Controlling Molecular and Microstructural Alignment in Anisotropic Polymer Systems

Dissertation by

Vinay Kumar Gupta

In Partial Fulfillment of the Requirements

for the Degree of

Doctor of Philosophy

California Institute of Technology

Division of Chemistry & Chemical Engineering

Pasadena, California

1996

(Defended June 1995)

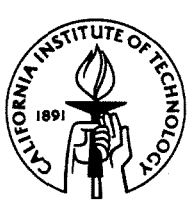

Dedicated to

my mother and father

for their love, constant support & encouragement

Acknowledgments

First of all I would like to thank my research advisor, Julia Kornfield, for all her help and guidance. She has been a constant source of boundless optimism, enthusiasm and inspiration. I would also like to acknowledge my thesis committee members—Dr. John F. Brady, Dr. George Gavalas and Dr. Zhen-Gang Wang—for their time and effort.

My aspirations have been greatly influenced by my parents. They have constantly expressed pleasure and pride in all my successes, and their love and blessings underlie all my achievements. Being the youngest in my family, I have been fortunate to receive the loving support of my older brothers and sisters. My brother, Surendra and sister-in-law, Sandhya have provided me time and again with valuable and much needed advice that has helped me throughout these years.

Apart from providing a stimulating environment for my doctorate, Caltech has given me an invaluable opportunity to interact with a set of tremendously talented individuals from every corner of the world. I am grateful for the assistance of Dr. Peter Bauerschmidt (Carl Zeiss), Prof. J. P. Revel (Biology, Caltech) and Tom Dunn (Electrical Shop, Caltech) during the development of the novel microscopy (PM-LSM). The Langmuir-Blodgett film work in this dissertation has been made possible by collaboration with Dr. Andreas Ferencz (MPI, Germany) and Prof. Gerhard Wegner (MPI, Germany). I also owe thanks to Dr. Steve Smith (Procter & Gamble) and Ramanan Krishanmoorti for their part in the investigation on block copolymers.

I have benefited greatly from a number of close friendships that I have formed dur-

ing my stay at Caltech. Among the members of the Kornfield research group I would like to thank Kannan, Chung, Barbara, Steve and Zhong-Ren for providing a very pleasant and intellectual working atmosphere. I appreciate the help and friendship of Kathy Lewis (research group secretary during most of my doctorate work), and thank Anne Hormann (the current research group secretary). I am especially grateful to Suresha Guptha, who has put up with my constant pestering and taught me a great deal. I have had the good fortune of working closely with Ramanan Krishnamoorti. He has had a great influence on both my personal thinking and my work, and I am forever indebted to him. I cherish my friendships with both Suresha and Ramanan.

It is difficult for me to list the numerous ways in which Susan has helped me. My years at Caltech have been thoroughly enjoyable, and my work successful due to her company and support. I look forward to sharing the rest of my life with her and having her love and support in the coming years of my life, and career.

Abstract

Molecular and microstructural orientation plays a key role in determining the useful mechanical, optical and electrical properties of a large class of polymeric materials. Realization of the technological promise of these materials requires rational control of the microstructure and understanding of the processing–structure–property relationships. Towards this end, we focus on the material properties and dynamical processes that affect molecular order of two complex polymeric systems **(a)** Ultra-thin Langmuir-Blodgett films of a hairy-rodlike polymer, and **(b)** Lamellar diblock copolymer melts of polystyrene and polyisoprene (PS-PI).

We accomplish our objective by improving and tying together existing analytic techniques into instruments extremely effective for measuring molecular orientation and order. For fundamental insights into the nature of alignment in ultra-thin ($\sim$ few nanometers thick) LB films, we integrate laser scanning microscopy (LSM) with polarization-modulation (PM) polarimetry. PM-LSM possesses high spatial resolution, sensitivity and speed, and allows us to image the anisotropy in films as thin as *two molecular layers*. To monitor the dynamics of flow alignment in diblock copolymers, *in situ* and in *real time*, we combine polarization-modulation polarimetry with rheometry. This rheo-optical technique enables us to monitor the evolution of microstructure by measuring the optical anisotropy, and correlate it with changes in macroscopic mechanical observables, such as stress and strain.

Using PM-LSM we have investigated the interplay of molecular weight, layer thickness and thermal annealing in controlling molecular order in rodlike polymer LB films. Upon investigating two different molecular weights of the polymer, we find lowering of molecular order in deposited films with increase in molecular weight. Furthermore, thermal annealing improves alignment only for films of shorter rodlike polymers ($\sim$ lower molecular weight). We believe that the underlying cause for these results is a difference in the structure of the deposited films for the longer polymer because of the relative changes in timescales for the macromolecular relaxation and the monolayer deformation during deposition. We also find that for both molecular

weights, the substrate exerts an anchoring effect on the first two layers adjacent to it and suppresses improvement in alignment on annealing. This inability to improve alignment has important consequences for applications such as molecular electronics where monolayers or bilayers having a high degree of orientation are required.

In-situ measurement of flow birefringence during oscillatory shear alignment, clarifies the evolution of the lamellar orientation distribution for a diblock copolymer melt. Shearing results in "parallel" or "perpendicular" alignment *i.e.* layers normal to either the velocity gradient or the vorticity axis, respectively (Figure 1.1). Both states of alignment occur via an initial "fast" process followed by a "slow" one. The fast process is dominated by the depletion of the projection of the orientation distribution along either the perpendicular direction or the "transverse" direction (layers normal to the flow). This resulting biaxial distribution is then transformed into a well-aligned uniaxial one during the slow process. Surprisingly, at particular frequencies, the projection along the perpendicular direction can disappear *faster* than the projection along the transverse direction. In both the fast and the slow processes the time evolution of birefringence follows a highly non-linear scaling with strain; the scaling being different for the fast and slow processes. A systematic study of the effects of strain on shear alignment in block copolymers led to the discovery that strain affects not only the dynamics of alignment, but also the direction. This phenomenon expands the range of parameters that can be used to flip the direction of alignment. In relation to previous studies that examined the regimes of alignment only in terms of temperature and frequency, this phenomenon necessitates consideration of a third dimension – strain.

Contents

List of Figures

List of Tables

Chapter 1

Introduction

1.1 Importance of Molecular Orientation

The escalating growth of polymer utilization in recent years has its roots in the coupling of the high-strength characteristics of polymers, with some unusual electronic and optical properties. Quite commonly, these remarkable properties are a direct result of the state of molecular orientation in the material and the ease with which it may be manipulated. Therefore, it is of significant interest to impart and sustain a desired molecular orientation, and to rationally control the microstructure in a material. For this purpose one needs meaningful processing–structure–property relations.

Establishment of such relations has been a conspicuous focus of industrial and academic research. Traditionally the objective has been to achieve improved mechanical strength in materials. For instance, in a vast number of commercially manufactured fibers and films, high-strength and high-modulus are achieved through parallel alignment of macromolecules. Many different ways can be employed to achieve this alignment, leading to a wide range of the mechanical characteristics among samples prepared by different technologies (*e.g.*, Table 1.1 Source: [1]). These differences can largely be accounted for by the specific supermolecular structure achieved in each case.

Importantly, the supermolecular structure also affects optical and electrical properties that, along with the mechanical stability of polymers, form the basis for a vast number of current and proposed technological applications. For example, many of

Table 1.1: Mechanical properties of oriented polyethylene (ultra high molecular weight and high density) samples produced in various ways.

Method	Tensile Strength (GPa)	Tensile Modulus (GPa)
Drawing of gel crystallized UHMWPE	6.0-7.0	150-200
Drawing of single crystal mats of UHMWPE	2.0-5.0	100-200
Extrusion of single crystal mats of UHMWPE with subsequent drawing	6.0	220
Surface growth technique for UHMWPE	3.0	20-100
Surface growth technique for UHMWPE with subsequent drawing	4.0-6.0 $10\% \leq 10.0$	120-130
Drawing of reactor UHMWPE powder	3.0-3.5	130
Solid state extrusion of HDPE	0.4-0.6	70
Multistage drawing of melt crystallized HDPE	1.5-2.0	100
Conventional commercial HDPE	0.15-0.4	5

the important optical properties of polymers—refractive index, reflection, scattering, absorption, clarity, gloss, haze, birefringence, and stress-optic coefficient—are necessary in evaluating the polymer's usefulness in an application. The stress-optic behavior finds use in compact disks; optical clarity is needed for eyeglasses, while both clarity and gloss are required for attractive packaging. The electronic properties of polymers are important in applications such as insulation of electric cables, encapsulants for electronic components, printed wiring board materials (PCBs). Inventive research has resulted in a large number of conducting polymers which open entirely new fields in photonics and molecular electronics. As molecular orientation generally underlies both the optical and electrical characteristics of a polymer, frequently the

combination of these physical properties enhances potential use. Familiar examples are liquid crystalline polymers in displays and data storage, nonlinear opto-electronics, and sensors.

Therefore, a rapid pace of material development has to be complemented with an equally rapid development in the ability to predict and control the properties of new (and existing) materials from basic scientific principles. Such an ability necessitates a fundamental insight into the relationship between the microstructure and the physical properties. For today's advanced and high-performance polymers, such an insight cannot be achieved from measurement of polymer properties, structure and morphology using a single technique. Development and implementation of multidimensional techniques is needed to do the job efficiently. One avenue which offers tremendous gains is a combination of existing analytic techniques to spawn an array of powerful multifunctional tools to probe structure in polymers.

1.2 Thesis Perspective

The aim of this dissertation is to aid in effective molecular design and processing strategies for polymeric materials that possess an inherent anisotropic structure. Application of these systems depend on the manipulation and control of microstructural alignment, and hence we focus on that aspect in two systems–(a) Langmuir-Blodgett films of rodlike polymers (Figure 1.1a) and (b) lamellar block copolymers (Figure 1.1b).

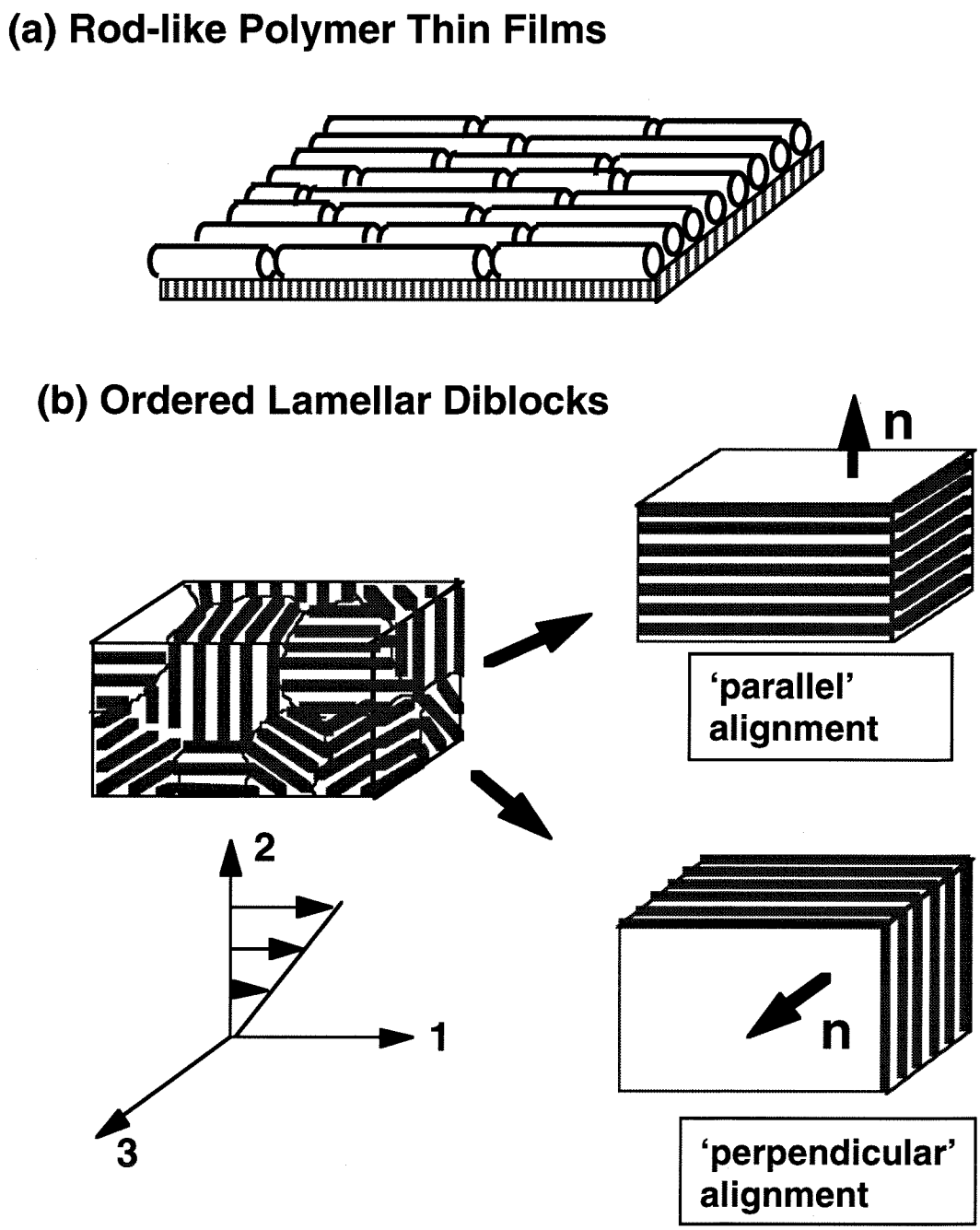

Figure 1.1: (a) Ultra-thin Langmuir-Blodgett films of rod-like polymer (b) Flow induced alignment of ordered lamellar diblocks.

1.2.1 Ultra-thin Langmuir Blodgett films

In the Langmuir-Blodgett technique, molecular monolayers are spread on a pure water subphase, and then transferred to solid substrates to obtain varying molecular architectures. The technological significance of such monomolecular films at boundaries between phases and multilayer structures transferred onto solid substrates has grown considerably as it has become possible to specify, design, fabricate and characterize ultra-thin films of thickness as small as a few Ångstroms [2, 3]. These films have numerous applications [4, 5] in molecular electronic devices, sensors, optical systems, lithography, and biotechnology. Further, these films provide model systems for fundamental study in physics, chemistry and biology. The basis of this tremendous potential is the high degree of molecular organization that persists in these films. Therefore, it is extremely pertinent to understand the properties and mechanisms responsible for the structural order in these films.

Experimental characterization of the degree and direction of alignment in films as thin as a few nanometers is required in order to understand how molecular design and processing strategies lead to the ultimate state of alignment. Various spectroscopic methods have been used to examine the structure, properties, and molecular arrangement of LB films [4–7]; however, detailed characterization of molecular order has been lacking because these spectroscopic techniques average over large areas of films. Spatial information with molecular resolution can in principle be obtained via transmission or scanning electron microscopy (TEM or SEM) [8–13], scanning tunneling microscopy (STM) [8, 14–16] or atomic force microscopy (AFM) [14, 17–21].

However, each of these methods is restricted to a limited number of systems. Typical LB film forming compounds cannot withstand the irradiation in TEM or SEM. Even for organic compounds that are hardy enough, low dose imaging is required. Films have to be prepared on special electron microscope grids, which significantly changes either the deposition procedures (film floatation or horizontal deposition) or the deposition dynamics (dipping grid-attached substrates). As most LB films are insulating, investigation with STM has to be performed on conductive substrates. Imaging with AFM requires that molecules of interest be rigidly mounted and immobilized with well-defined orientation to avoid damage by physical contact.

The complex microstructure in these organic films depends intricately on a combination of molecular structure, deposition dynamics, substrate properties and post-treatment. Consequently, meaningful structure-property relations have to be established under conditions closer to those in potential manufacturing processes. Techniques such as EM, STM, or AFM are unsuitable to characterize molecular alignment required to study these relationships. In contrast, optical measurement techniques are non-invasive and nondestructive, have fast response times and high sensitivity, and can be used to perform measurements under ambient conditions. However, established optical tools cannot perform quantitative imaging of order in ultrathin films.

Therefore, a major aim of this work is to address the need for rapid, sensitive imaging of molecular orientation. Chapter 2 describes how we accomplish this objective by developing a novel technique that integrates polarization modulation with laser scanning microscopy. Description of the materials, the results of our investiga-

tion of structure in rod-like polymer films, and discussion of the results are contained in Chapter 3.

1.2.2 Lamellar Block Copolymers

Block copolymers are macromolecules composed of sequences, or blocks, of chemically distinct repeat units. Generally, their equilibrium morphology exhibits local segregation into periodic nanostructures, called their ordered, microphase separated state. If ordering occurs in the absence of a symmetry-breaking field, the material is isotropically ordered. Using fields such as electric fields and flow fields, "single-crystal" like order can be induced on global length scales in these microphase separated block copolymers [22–34]. In particular, for lamellar diblock copolymers it has been shown that two states of macroscopic order can be achieved by large amplitude oscillatory shear. Shearing at different frequencies but at the same temperature and strain amplitudes [28, 29] can produce alignment either with layer normals along the shear gradient direction (parallel), or with layer normals along the vorticity direction (perpendicular) (Figure 1.1). Similar lamellar orientations can also be induced by shearing smectics and lamellar surfactant mesophases [35–37].

The underlying causes and mechanisms of alignment and the selection of one alignment over the other remain largely speculative in spite of more than two decades of theoretical and experimental work. Therefore, a fundamental understanding of the evolution of microstructure in diblocks during shear would be valuable in enabling new applications of diblocks, and clarifying common features of shear orientation

and viscoelastic behavior in the class of layered materials that spans smectic liquid crystals, surfactant membranes and layered polymer composites [35, 36, 38, 39].

Hypotheses regarding alignment mechanisms in lamellar diblocks have been based primarily on the changes in the microstructure observed after alignment using small angle neutron scattering (SANS) [28], transmission electron microscopy (TEM) and small angle x-ray scattering (SAXS) [34, 40]. Apart from the possibility of artifacts induced during the cooling, cutting and mounting processes for sample preparation, such characterization does not provide any information on the molecular and microstructural dynamic responses during flow alignment. This information is vital to discriminate among existing ideas and to formulate mechanisms to explain flow alignment. Thus, real time, *in situ* studies are essential to understanding the mechanism of flow alignment - a prerequisite for rational control of the macroscopic ordering in block copolymers and other mesostructured materials.

To address this need, we study alignment in a lamellar polystyrene-polyisoprene (PS-PI) block copolymer by implementing *in situ* rheo-optical measurements. In PS-PI, birefringence measurements can be directly related to the lamellar orientation distribution in the sample, which permits study of the coherent macroscopic order as it develops during oscillatory shear. Furthermore, birefringence measurements provide a much higher time resolution ($\sim$ 100ms) than can be achieved with SAXS or SANS ($\sim$ 10-100s) measurements. The instrumentation for these measurements has been previously developed and we describe it only briefly in the methods section in Chapter 2. The results on the evolution of alignment, and their interpretation are

presented in Chapter 4.

1.3 Multifunctional Characterization Techniques

This thesis also contributes to and benefits from a rapidly expanding technological base that is enabling more sensitive and more precise methods of characterization. Continuous improvement in digital electronics and computation systems makes it increasingly possible to design sophisticated, semi or fully automated instruments that explore a wide breadth of material properties and structure. Concomitantly, there have been a host of "hyphenated techniques" developed that combine accurate techniques of polymer analysis and meet the need of the current research environment for higher quality information in shortened analysis times for both polymer properties & morphology, and for process monitoring & control. The ability to use multifunctional characterization techniques to analyze the structural and quantitative features of polymers has become a popular concept, and a common interfacing of two or more instruments is becoming indispensable (Figure 1.2,Source: [41]).

This concept of multifunctionalism provides a powerful means to achieve the goal of understanding structure-property relations in polymers. In particular, in a number of anisotropic polymer systems, the macroscopic properties have contributions from molecular and microstructural responses that depend intricately on material properties and processing variables. It is therefore instructive to look at the microscopic origins of alignment, along with other macroscopic characterization, to understand the governing physical mechanisms. Benefiting from the ideas of multifunctionalism,

Separation Methods
- Chromatography
  - Gas (GC), Liquid (LC),
  - Thin Layer (TLC)
  - Gel Permeation (GPC),
  - Size Exclusion (SEC)
- Mass Spectrometry (MS)
- Pyrolysis
- Vapor Pressure Osmometry (VPO)

Thermal-Mechanical Methods
- Differential Scanning Calorimetry DSC
- Thermogravimetric Analysis TGA
- Dielectric Constant Measurement
- Torsional Braid Analysis TBA

Rheological Methods
- Cone/Plate Viscometry
- Co-Axial Cylinder Viscometry
- Parallel Plate Viscometry

Spectroscopic Methods
- Fourier Transform Infrared (FTIR)
- Internal Reflection (ATR)
- External Reflection (RA)
- Spectroscopy
  - Emission, Photoacoustic,
  - Rheo-Photoacoustic, Auger,
  - X-Ray Photoelectron (XPS),
  - Fluorescence, Dichroism,
  - Phosphorescence, UV-Vis
- Infrared Microscopy
- Ellipsometry
- Raman Scattering and Microscopy
- Electron Scanning Chemical Analysis
- Nuclear Magnetic Resonance (NMR)
- NMR Imaging
- Light Scattering
- X-Ray Scattering (SAXS, WAXS)
- X-Ray Diffraction, Electron Diffraction

Morphological Analysis
- Optical Microscopy
- Phase Contrast Microscopy
- Scanning Electron Microscopy (SEM)
- Scanning Tunneling Microscopy (STM)
- Atomic Force Microscopy (AFM)

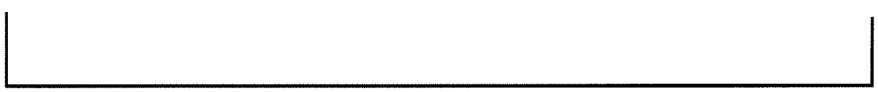

LC-SEC, SEC-FTIR, SEC with MS, 2D-NMR, multidimensional FTIR,
pulse pyrolysis FTIR, HPLC/UV, Thermal Gradient LC, MS-GPC, TG-DSC,
TG-DSC-MS, TG-DSC-FTIR, DSC-FTIR, DSC-SAXS and DSC-WAXS,
Rheo-Optics : Rheological Methods and Light Scattering
Rheological Methods and Dichroism/Birefringence
Rheological methods and X-Ray Scattering

Figure 1.2: Common techniques for material characterization, and some examples of the hyphenated multifunctional techniques used currently.

we develop and implement unique combinations of mechanical and optical methods to address key problems in the polymer physics arena.

Chapter 2

Characterization of Polymer Structure

2.1 Probing Structure with Polarized Light

Among the numerous advantages of optical techniques are fast response times, high sensitivity and micron-scale spatial resolution. Currently, a host of optical techniques are employed in the characterization and investigation of the distortion and orientation by measurement of a material's interaction with light. Among such optical methods is polarimetry [42] wherein changes in polarization of light, transmitted through the sample, are measured and analyzed to determine the structural anisotropy of the system.

The polarization of light is affected by the material's refractive index tensor $(n'_{ij} + in''_{ij})$ in two ways: anisotropic attenuation (dichroism, $\Delta n''$) and/or anisotropic retardation (birefringence, $\Delta n'$). In structurally anisotropic materials, the magnitude and orientation of these quantities can be related to the orientational correlation that exists in the material. High sensitivity in the measurement of the optical anisotropies can be achieved by introducing a carrier frequency at which the polarization state of the light beam is modulated [43, 44].

The modulation scheme we use (Figure 2.1) employs a photoelastic modulator (PEM) that has a sinusoidal time-varying phase retardation ($\delta_o \sin ft$). The particular polarization state generating (PSG) optics we use produces a linearly polarized beam of constant intensity and an orientation that sweeps back and forth through a wide angle at a frequency f. As the polarization direction sweeps back and forth, the beam probes the orientation dependence of the properties of the sample. If the material is linearly dichroic, then the attenuation of beam rises and falls as its orientation

sweeps back and forth. By analyzing the resulting modulation in intensity, we may determine the absorption anisotropy (ν) and its orientation angle (χ). In particular, if we demodulate the intensity into its steady part (I_{dc}, from the low pass filter, LPF) and its first and second harmonics (I_f and I_{2f}, from two lock-in amplifiers, LI1 and LI2) (Figure 2.1), the normalized harmonics can be used to determine ν and χ using the following relations [45]:

$$R_f \equiv I_f/I_{dc} = \frac{2J_1(\delta_o)\sin(2\chi)\sinh(\nu)}{\cosh(\nu) - J_o(\delta_o)\cos(2\chi)\sinh(\nu)} \tag{2.1}$$

$$R_{2f} \equiv I_{2f}/I_{dc} = \frac{-2J_2(\delta_o)\cos(2\chi)\sinh(\nu)}{\cosh(\nu) - J_o(\delta_o)\cos(2\chi)\sinh(\nu))}, \tag{2.2}$$

where J_o, J_1 and J_2 are calibration constants determined using samples of known optical anisotropy, and $\nu = \frac{2\pi\Delta n'' d}{\lambda}$ for an optical path length, d, and wavelength of light, λ.

For the case of a sample that is birefringent with little or no dichroism, only the phase of the transmitted beam is anisotropically affected by the sample. That is, as the orientation of the incoming polarization swings back and forth, the degree of ellipticity of polarization state of the emerging beam rises and falls. This modulation of the ellipticity of the polarization state may be translated into a measurable intensity variation using a circular polarizer as the polarization state analyzer (PSA in Figure 2.1). In this case,

$$R_f = \frac{2J_1(\delta_o)\cos(2\chi)\sin(\mu)}{1 + J_o(\delta_o)\sin(2\chi)\sin(\mu)} \tag{2.3}$$

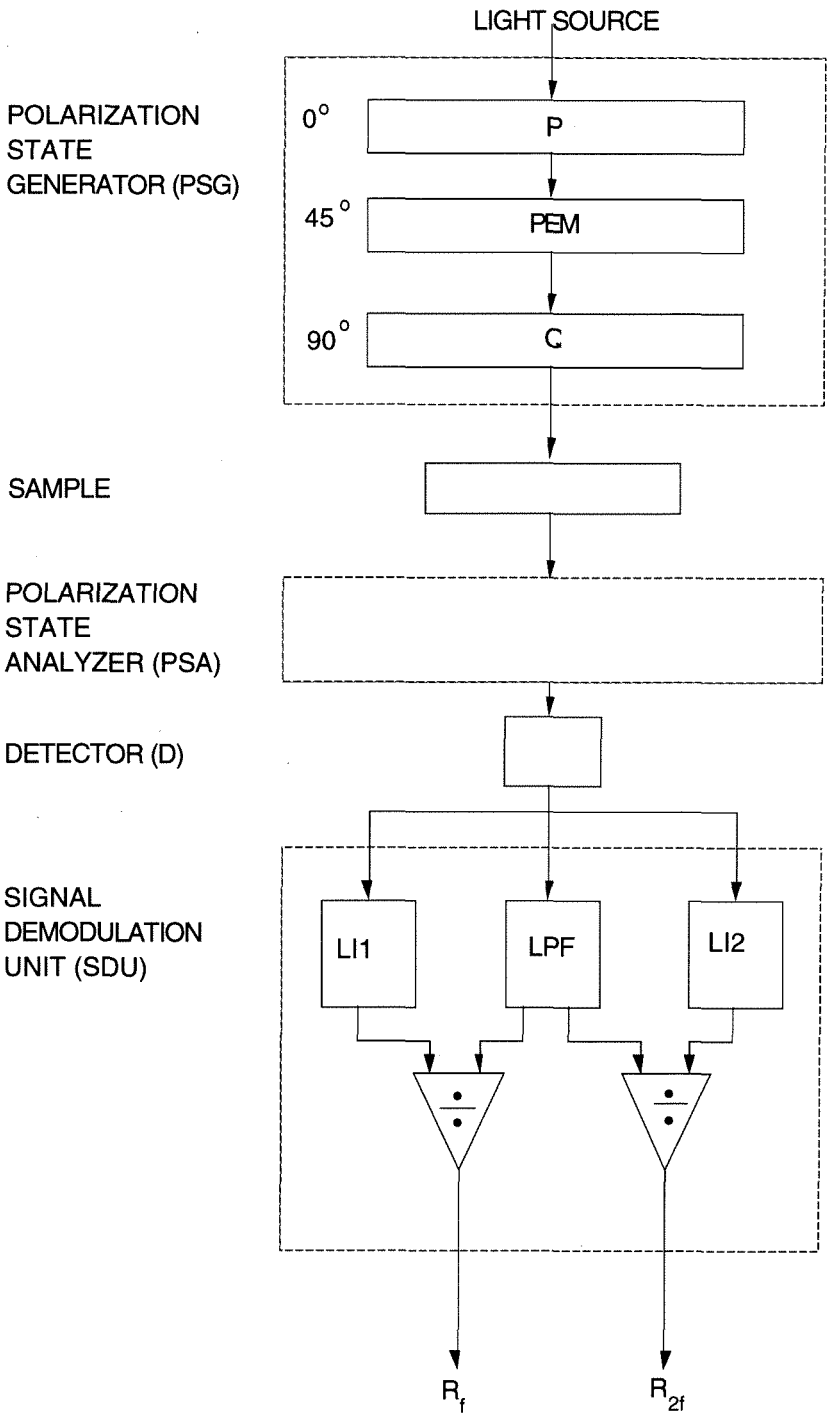

Figure 2.1: Schematic of the optical arrangement for simultaneous measurement of the magnitude and orientation of dichroism or birefringence exhibited by a material. P=Polarizer, PEM= Photoelastic Modulator, Q= Quarter Wave Plate, LI=Lock-In Amplifier, LPF=Low Pass Filter.

$$R_{2f} = \frac{2J_2(\delta_o)\sin(2\chi)\sin(\mu)}{1 + J_o(\delta_o)\sin(2\chi)\sin(\mu)}, \tag{2.4}$$

where μ is proportional to the magnitude of birefringence ($\mu = \frac{2\pi\Delta n' d}{\lambda}$), and χ its orientation [45].

As a result of polarization modulation, the need for rotating the polarizers or the sample is obviated. A rapid dynamic response is achieved. And locking to the carrier frequency f provides high sensitivity, making it possible to measure weak birefringence or dichroism. While this sensitivity makes polarization-modulation polarimetry ideally suited to the present study of molecular orientation and microstructure, it alone does not suffice and we need to enhance the capability of polarimetry to achieve our objective of understanding alignment in thin films, in which the spatial variation of alignment is important.

2.2 Imaging Orientation Fields

To adequately characterize the structure of ultra-thin films, we need to *image* anisotropy to determine the uniformity of the magnitude and direction of alignment in a thin film. Polarimetric techniques are typically used with a fixed beam which provides information that is spatially averaged over the spot of incidence of light [46, 47]. To achieve the required imaging capability, we integrate polarization-modulation polarimetry with scanning optical microscopy.

2.2.1 Optical Scanning Microscopy

A fundamental feature of optical microscopy is that the object to be imaged is illuminated as a whole by a condenser and imaged onto an intermediate image plane by the objective. This intermediate image plane is viewed with an eyepiece as in conventional microscopy or can be scanned with the electron beam of a camera tube in TV microscopy. The field of the image plane can be restricted to a smaller area and the intensity detected using photomultipliers or photodiodes. In contrast, in scanning microscopy [48] the object is not illuminated as a whole but is illuminated point by point, and the reflected or transmitted or scattered light is measured using photodetectors (Figure 2.2). These point measurements are transformed into brightness values that can be viewed on a conventional video monitor. This method possesses considerable advantages over conventional light microscopy as it allows electronic enhancement of the contrast and the brightness of the image. Coupled with elimination of stray light background due to interfering light, scanning microscopy results in a much superior image.

A number of additional features increase the performance of scanning microscopy. A laser light source provides highly collimated, monochromatic light that can be focussed on a small area with a high intensity. Due to the high speed of scanning, the residence time of the high intensity beam at each point is very small and no degradation of the sample occurs. Scanning is achieved either by rastering the beam or by mechanically moving the sample. Acousto-optical deflectors, or resonant or servo-controlled galvanometer systems for the former option can greatly enhance the

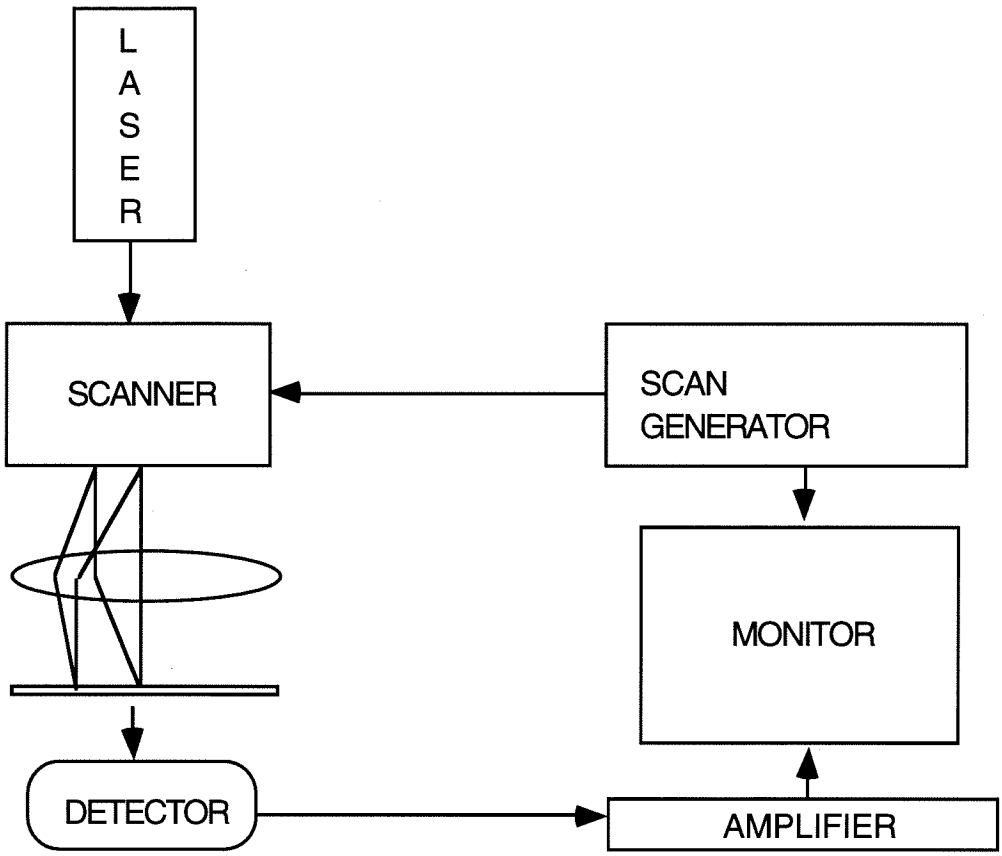

Figure 2.2: Basic schematic of an optical scanning microscope.

speed of scanning.

The features of scanning microscopy and polarimetry have been recently combined in differential polarization imaging, and differential polarization microscopes have been employed to probe the molecular organization in biological specimens [49, 50]. An optical train is set up in the microscope by incorporating polarizing optics, in particular, adding the PSG and the PSA sections in the optical path (Figure 2.3). Images are constructed from the magnitude of linear and circular dichroism that is measured. However, both of the previous prototypes require image acquisition at two different orientations in order to determine both the magnitude and orientation of

dichroism or birefringence. Furthermore, these prototypes of differential polarization imaging do not use a laser light source and the light source is fixed so the sample has to be moved in raster fashion with respect to to stationary spot of light, limiting the scanning speed.

2.2.2 Polarization-Modulation Laser Scanning Microscopy

The basic principle behind the previous differential-polarization microscopes can be extended to provide simultaneous determination of both the magnitude and the orientation angle of dichroism and birefringence. And vast improvements in sensitivity and speed can be achieved by using laser light and rastering the beam rather than the sample.

To achieve these improvements we have integrated a polarization-modulation optical arrangement in a Zeiss laser scanning microscope (LSM) [51, 52] (Figure 2.3). As the laser beam rasters across the sample, the two lock-in signals from each pixel are normalized by the steady component of the intensity. The two ratios R_f and R_{2f} are calculated at each pixel. We modified the electronics of the LSM to record these two signals. Using this information, we create an image of the orientation of the optical axis χ and degree of ordering, proportional to ν or μ, from eqs. (2.1-2.2) or (2.3-2.4), as appropriate for the sample.

In the Zeiss laser scanning microscope a polarized laser beam is focussed to a diffraction-limited spot, which is rastered across the image very rapidly using a servo-controlled, feedback galvanometer system. A dual laser option provides laser light at

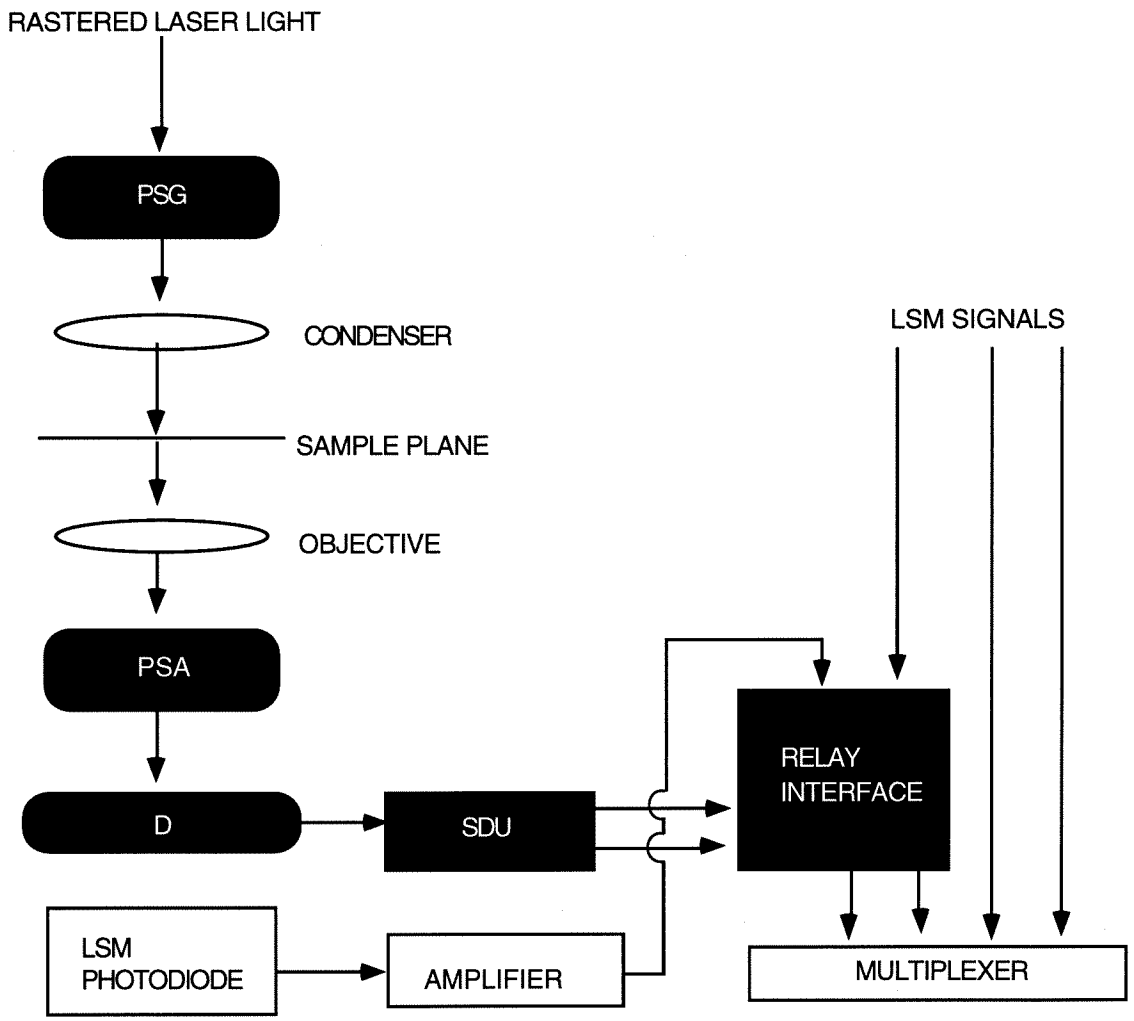

Figure 2.3: Basic schematic of the polarization-modulation laser scanning microscope that integrates polarimetry and scanning microscopy to allow quantitative imaging of the dichroism or birefringence field.

wavelengths of 514 nm and 488 nm for an Argon-ion laser and at 543 nm for a green Helium-Neon laser. Electronic zoom over a range of 1:8 combined with appropriate lenses permits a field of view ranging from $6000 \times 4000\mu m$ to $19 \times 14\mu m$. The Zeiss LSM also allows the simultaneous display of images constructed from two independently acquired signals. This feature is extremely valuable in our scheme of PM-LSM as we record the two ratios R_f and R_{2f} simultaneously.

Our modifications of the LSM have been designed to facilitate changing between operation in the conventional laser-scanning mode and the new polarization-modulation laser-scanning mode. The modifications can be can be divided into two major categories:

- **Optical Modifications** A special polarization modulating unit has been fabricated that contains all the three components of the polarization state generator of our optical train (PSG in Figures 2.1 and 2.3). The analyzer components which include a collecting lens and circular polarizer (for birefringence images), go beneath the sample stage in the microscope (Figure 2.3).

- **Electronic Modifications** to record the normalized lock-in amplifier signals R_f and R_{2f} that are needed to measure the magnitude and orientation of birefringence or dichroism. We have equipped the LSM with an external silicon photodiode that intercepts the laser beam (Figure 2.3). The signal from the detector is demodulated by the lock-in amplifiers (Figure 2.1). The lock-in outputs are normalized by the mean intensity (I_{dc}) provided by a low-pass filter (Figure 2.1) and then fed to the signal processing unit of the LSM via a relay switch.

Here we describe these optical and electronic modifications in more detail. The polarization modulating unit consists of a linear film polarizer, a Hinds International photoelastic modulator (PEM) oriented at 45° with respect to the polarizer and a quarter-wave retarder oriented at 90° with respect to the polarizer (Figure 2.1). A half-wave plate can be used above the PSG module to rotate the polarization direction

of the laser light and bring it parallel to the linear polarizer (P in Figure 2.1). The frequency of the modulator is $f = 63\text{kHz}$ and the amplitude (δ_o) of its sinusoidal retardation set such that $J_o(\delta_o) = 0$ so that equations 2.1-2.2 simplify to

$$R_f = 2J_1(\delta_o)\sin(2\chi)\tanh(\nu) \tag{2.5}$$

$$R_{2f} = -2J_2(\delta_o)\cos(2\chi)\tanh(\nu) \tag{2.6}$$

and equations 2.3-2.4 simplify to

$$R_f = 2J_1(\delta_o)\cos(2\chi)\sin(\mu) \tag{2.7}$$

$$R_{2f} = 2J_2(\delta_o)\sin(2\chi)\sin(\mu) \tag{2.8}$$

After passing through the appropriate analyzing optics as described earlier, the laser light is intercepted by the externally provided Si photodiode (Universal Detector, 6pinDP) where the light intensity is converted to an analog voltage signal. The steady part of this signal, I_{dc}, is extracted using a Stanford Research SR-640 low-pass filter (LPF in Figure 2.1). Synchronous demodulation is performed using two lock-ins: a Stanford Research SRS-850 Digital Lock-in Amplifier (LI1 in Figure 2.1) and an Ithaco 3962A Lock-in Amplifier (LI2 in Figure 2.1). The scanning rate is limited by the requirement that the dwell time per pixel be sufficiently large for the lock-ins to isolate the two harmonics. This can be achieved by keeping the dwell time per pixel about five times the time constant of the low pass filter circuit in the lock-in. Here we

are limited by the minimum time constant of 100 μs for the Ithaco 3962A; the SR 850 has a 10 μs minimum time constant. The first and second harmonics obtained from the two lock-ins are normalized by I_{dc} using two ratiometer circuits and transmitted to the microscope signal processor via the relay interface and protection circuit. The relay switch toggles between the two regular internal LSM signals and the two external signals (Figure 2.3). Using the Zeiss LSM's unique capability to record the two signals simultaneously, the dual grey-scale image is saved in the LSM's internal format. Image analysis is subsequently performed on a Sun workstation (Sparc2).

Calibration is performed using a linear polarizer and the images for J_1 and J_2 are recorded. Given these values of J_1 and J_2, the grey level values for each pixel in the image of a sample are converted into the magnitude (ν or μ) and orientation (χ) values for that pixel. Using these, the whole image is reconstructed, pixel by pixel, for both the magnitude and orientation [53].

2.3 Monitoring Flow-Alignment

Fundamental insight into the dynamics during shear-alignment of lamellar diblock copolymers requires one to discover the correlations, and ultimately the causal relationships between macroscopic properties and the underlying micro-scale responses during shear. This in turn necessitates observation of changes in the copolymer microstructure together with characterization of the macroscopic mechanical consequences. We accomplish this objective by combining polarization-modulation polarimetry and rheometry.

2.3.1 Polymer Rheology

Rheology is concerned with understanding the behavior of these materials under flow, and describing how their stress-strain behavior is modified by flow, which typically imposes a combination of shear, extension, and bulk deformation [54].

Rheological characterization of a material involves measurement of the response to imposed flow-fields. This response is typically a combination of a viscous and an elastic response.

- In viscous flow, a material continues to deform as long as the stress is applied; the energy put in to maintain the flow is dissipated as heat. Such a response is characterized with the viscosity which is the ratio of stress to rate of strain (*i.e.* $\eta = \frac{\sigma}{\dot{\gamma}}$). When the material flows with a viscosity independent of the stress level, it is termed as a Newtonian. Commonly, polymer melts approach this behavior at low stress levels.

- In contrast, a material exhibits elastic response when it deforms instantaneously under stress and the deformation is spontaneously reversed when the stress is removed. In this case the material possesses a characteristic modulus which is the ratio of stress to the recoverable strain (*i.e.* $G = \frac{\sigma}{\gamma}$). For a completely reversible deformation that is also proportional to the applied stress, the material is termed a Hookean solid.

The character of the viscoelastic response can be described using a dimensionless group termed the *Deborah number (De).* It is defined as the ratio of a characteristic timescale (λ) of the fluid to a characteristic time of the flow system (t_{flow}). In the

limit of small Deborah number ($De \rightarrow 0$), thermal motion keeps the molecules in equilibrium configurations, and the material is Newtonian. On the other hand, for large Deborah number ($De \gg 1$), the microstructure of the fluid is distorted by flow (*i.e.* it cannot relax during t_{flow}).

An effective method to characterize the viscoelastic response of polymeric liquids is oscillatory shear wherein the material is subjected to a sinusoidal shear history. At small deformations, the stress response, $\sigma(t)$, for an entirely elastic material is also sinusoidal and in phase with the applied strain, $\gamma(t)$, with an amplitude that is described by the modulus (G) of the material. For an entirely viscous material, the stress response is exactly $\pi/2$ out-of-phase with the strain. For fluids of intermediate viscoelastic character, the phase shift for the stress response is also intermediate between 0 and $\pi/2$. Mathematically, this is represented as

$$\gamma(t) = \gamma_o \sin \omega t \tag{2.9}$$

$$\sigma(t) = \sigma_o \sin(\omega t + \delta) \tag{2.10}$$

$$= \gamma_o [G'(\omega) \sin \omega t + G''(\omega) \cos \omega t] \tag{2.11}$$

where the stress has been resolved into an elastic or in-phase component characterized by the storage modulus, G', and a viscous or out-of-phase component characterized by the loss modulus, G''. At low frequencies (low De), it is common for a polymer to exhibit viscous flow, while at high frequencies (large De), the polymer melt behaves as a solid or is elastic-like.

Complete characterization of the viscoelastic behavior of the polymer sample in-

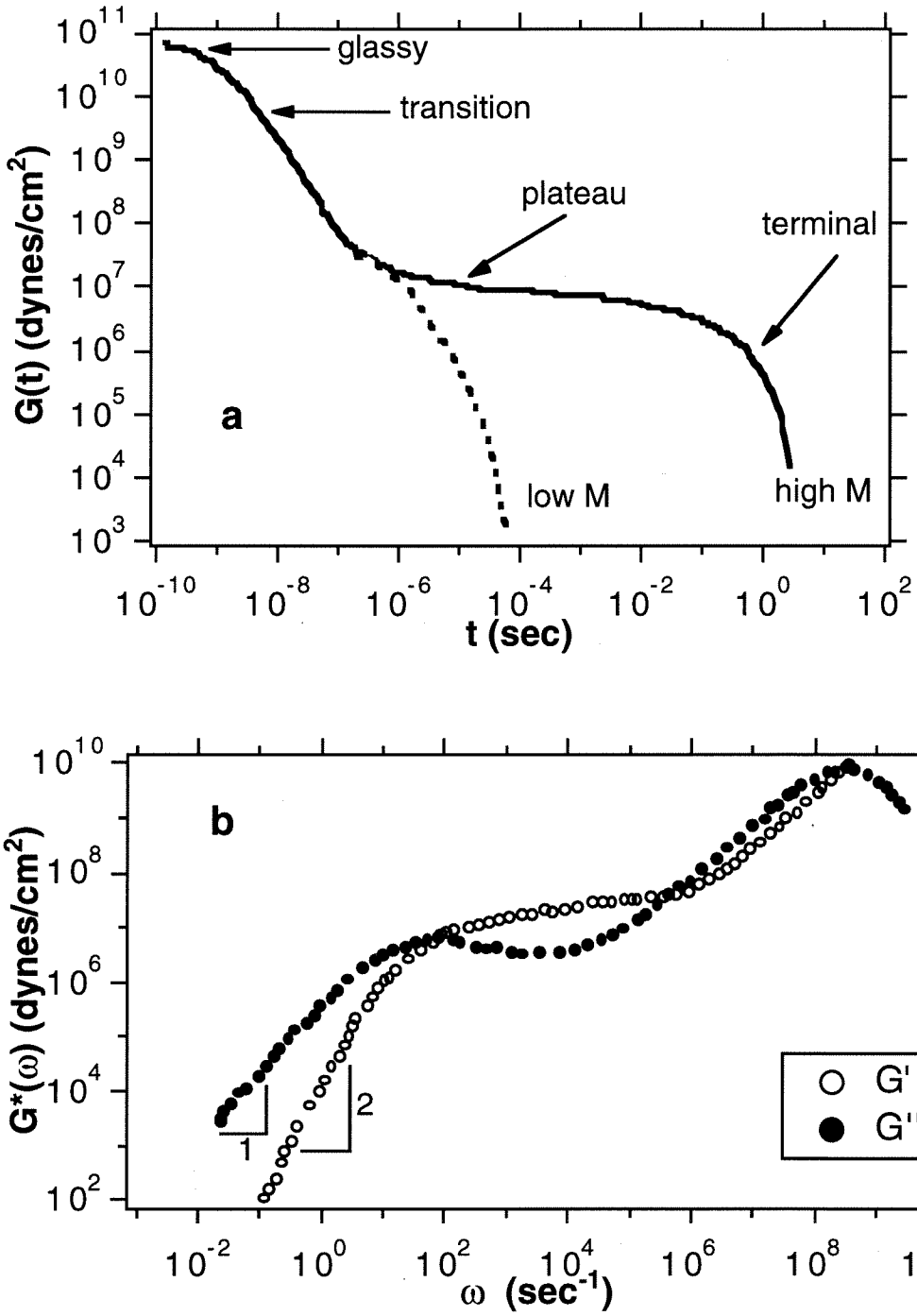

Figure 2.4: Shear stress relaxation for a typical polymer melt plotted as (a) dynamic modulus G(t) as a function of time (b) dynamic moduli $G^*(\omega)$ against frequency.

volves measurements of the stress-relaxation modulus (or the dynamic moduli spanning many orders of magnitude in modulus and frequency (or time-scale) (Figure 2.4). Experimentally this is difficult to achieve at a single temperature (T) as most instruments possess limited dynamic range of testing. Therefore, for most homogeneous polymer liquids, composites of data measured at different temperatures are assembled together using the time-temperature superposition principle. A change in the temperature of measurement shifts the viscoelastic functions along the modulus and time (or frequency) scales without change in the spectrum shape. Raising temperature shifts relaxation to lower times (higher frequencies) and *vice versa.*

$$G(t,T) = G(t/a_T, T_o)/b_T \tag{2.12}$$

$$G'(t,T) = G'(\omega a_T, T_o)/b_T \tag{2.13}$$

$$G''(t,T) = G''(\omega a_T, T_o)/b_T \tag{2.14}$$

Here, T_o is some convenient reference temperature and a_T and b_T are empirically determined shift factors. Typically, the shift in modulus values is very small (*i.e.* b_T is near unity), and the predominant effect of changing temperature is a shift along frequency scale.

Thus, the mechanical response as observed by the dynamic moduli (Figure 2.4) is a macroscopic reflection of the dynamic processes occurring at the molecular level. However, fundamental understanding of the flow behavior requires characterization of the processes occurring on the microscopic scale as well, and here, optical methods are especially suitable.

2.3.2 Rheo-Optical Measurements

Generally, flow induced distortion and orientation of the material constituents affect the interaction with light, and thus measurement of this interaction gives valuable information of the molecular and mesoscopic dynamics. Rheo-optics designates the use of optical techniques such as birefringence, dichroism, and light scattering as complements to standard rheological methods outlined in the previous section [44]. In our description of rheo-optic techniques, we are going to focus only on integration of polarimetric techniques with rheology.

Flow birefringence has been the traditional methodology to measure stress fields in polymeric liquids. Such measurement has been possible for many homopolymer melts and solutions under simple shear since this optical anisotropy has a simple, linear relationship with the components of the stress tensor (stress-optical rule). Orientation at the molecular scale, *i.e.* of the polarizable chemical bonds causes a polymeric material to exhibit birefringence, and the magnitude of this "intrinsic" birefringence depends on the degree of orientation and the characteristics of the bonds (bond polarizability). Polymeric materials also exhibit a second type of birefringence that results from "form" anisotropy or the refractive index contrast that exists due to different phases within the liquid. In this case, characterization of the flow birefringence simultaneous with stress gives information on the orientational and the mechanical response of these phases due to the applied flow.

Based upon these ideas, a rheo-optical apparatus uniquely suited for simultaneous, quantitative measurements of dynamic stress and birefringence over a wide range of

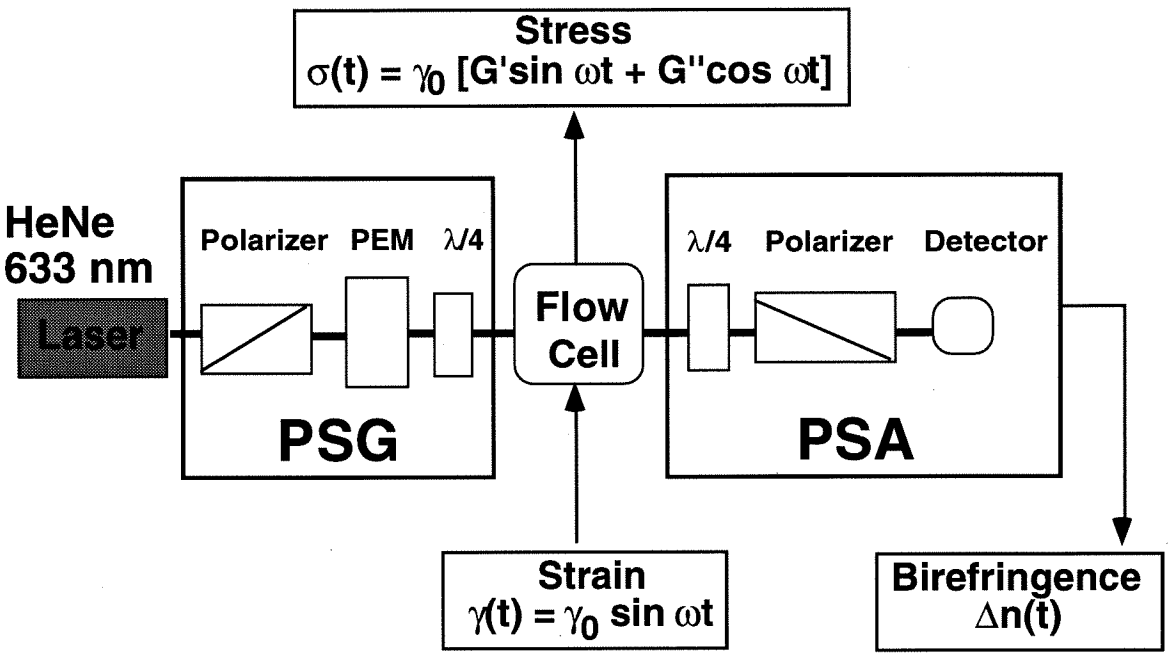

Figure 2.5: Basic schematic of rheo-optic apparatus that integrates polarimetry and rheometry.

frequency (0.01 to 100 rad/s) and temperature (-100 to 400°C) has been constructed by Kannan *et al.* (Figure 2.5). The construction of this apparatus, the instrumentation and data acquisition are described in detail elsewhere [55, 56]. We use this apparatus for monitoring flow alignment in block copolymer melts.

Chapter 3

Controlling Alignment in Ultra-Thin LB Films

3.1 Langmuir-Blodgett Films: Background

Ultrathin films, from less than a nanometer to about a micron thick, are extremely significant in catalysis, colloidal science, biomedical science, materials science and other fields involving study of surfaces and interfaces. Most technological and scientific uses of such thin films require control of the uniformity and molecular organization within the film. While fabrication of organized layers can be achieved by a number of methods, the Langmuir-Blodgett (LB) technique is especially suited to build films of molecular dimensions with a fine control of the film architecture. Using the LB technique, monomolecular and multilayers with a precise order and composition can be built-up, and unusual properties imparted to the films. Consequently, LB films possess numerous potential applications as nonlinear optical systems, molecular templates for protein crystallization, insulating or patterning layers in microelectronic devices, and selective layers in biosensors.

In the LB technique, a solution of molecules is spread on the water surface in a shallow container called the Langmuir Trough (Figure 3.1). The solvent, which is insoluble in water, evaporates and the solute molecules behave as a two-dimensional gas on the water surface. Surface compression via a movable barrier reduces the area per molecule, forcing molecules to move towards a solid crystal phase. During the compression, molecules pass from a two-dimensional gaseous state to a two-dimensional liquid like state, and then, on to a range of liquid-crystal-like states. Further increase in the surface pressure (π) results in a solid crystal phase and eventual film collapse. The surface pressure is the difference between the surface tension of pure water and

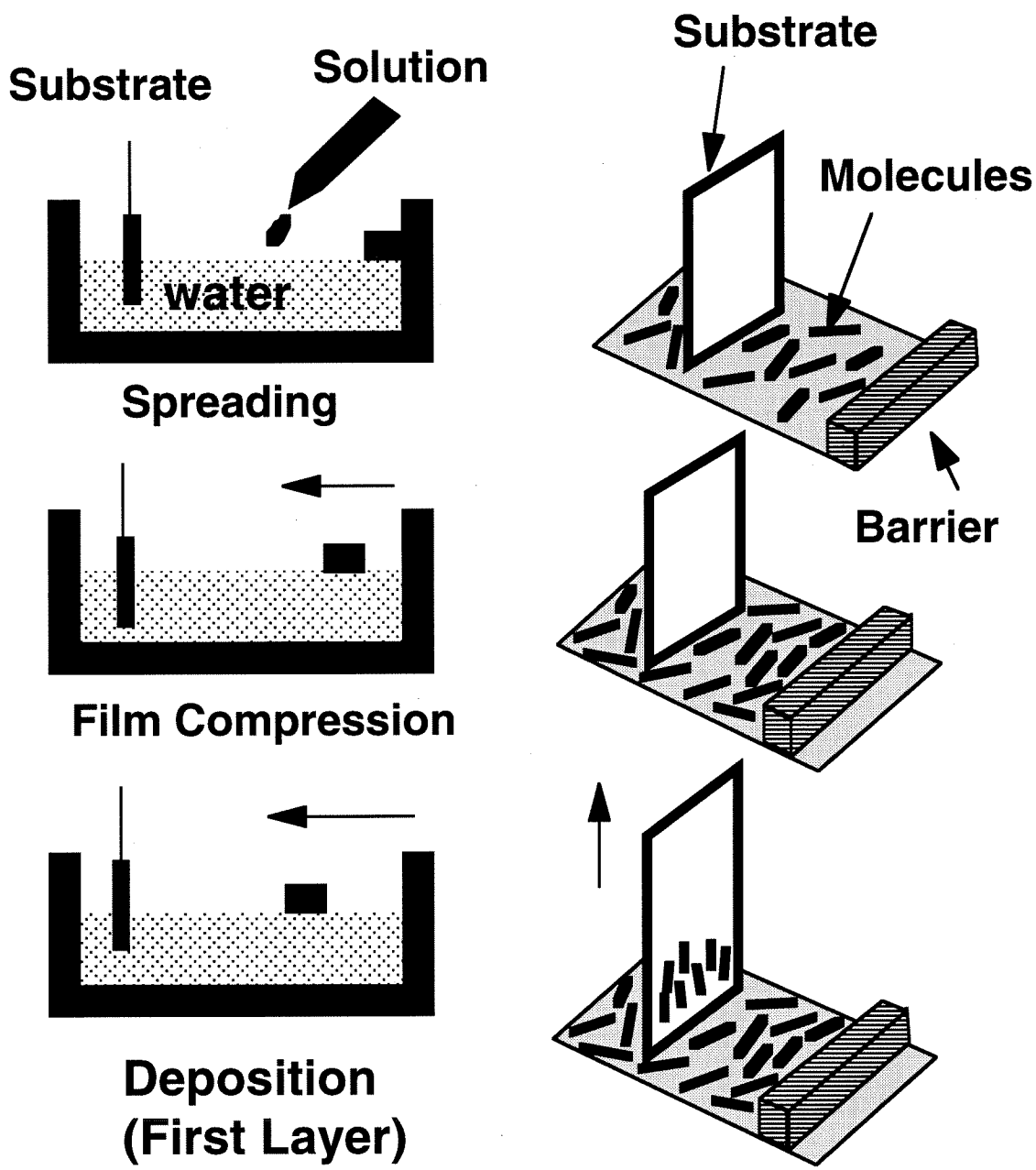

Figure 3.1: Schematic of the Langmuir-Blodgett technique.

the water carrying a surface film.

$$\pi = \pi_{water} - \pi_{film} \tag{3.1}$$

Measurement of the surface pressure *vs.* area isotherm reveals information about the thermodynamics of a monolayer. The nature of phase transitions can be deduced from thermodynamic models. Domain formation under conditions where two phases co-exist can be studied qualitatively using fluorescence microscopy [57]. However, due to the extreme difficulty in obtaining quantitative information on the surface by classical x-ray structure analysis and electron microscopy, the physics of phase transitions in monolayers on the surface of water remains an active area of investigation.

Quite frequently, reduction of the surface area during film compression is accompanied by an orienting effect on the molecules deposited on the water surface and two-dimensional crystalline domains with grain boundaries are formed [58, 59]. Grain boundaries result from the mismatch in the orientation of molecules on the surface. Upon transfer of the films onto the solid substrates, films retain these grain boundaries, which degrade their mechanical, optical and electrical properties. With the emergence of polymeric films, it has been possible to achieve superior mono- and multi-layers with higher stability, fewer defects and greater technical applicability.

We focus on polymeric LB films and are interested in understanding and quantifying the processing-structure-property relations that control the state of alignment and order within the films. Towards this end, we experiment on Langmuir-Blodgett films of rigid-rodlike polymers, where the rod-axis lies parallel to the plane of the

surface. These films possess a high degree of anisotropic order, which finds important applications in microelectronic devices. Furthermore, films that exhibit liquid crystalline character in two-dimensions represent ideal systems for fundamental study in the area of condensed matter physics.

In our research we take advantage of the anisotropic refractive index exhibited by the films of rod-like molecules due to their lateral orientation and their shape anisotropy. The direct relationship between the refractive index tensor $\hat{n}_{ij}$, and the orientational order parameter tensor makes it possible to use an experimental image of the spatial variations of $\hat{n}_{ij}(\mathbf{r})$ to determine the field of molecular orientation in the film. We perform this imaging using our newly developed technique of polarization-modulation laser-scanning microscopy.

3.2 A "Hairy-Rod" Polymer (PcPS)

The model polymeric system we choose, for study of molecular orientation and order in ultrathin LB films, is a "hairy-rod" polymer [tetra(methoxy)-tetra(octyloxy)-phthalocyaninatopolysiloxane, PcPS]. (Figure 3.2) [60–64]. The monomer consists of a silicon-substituted phthalocyanine ring with four pairs of side groups attached in a random cyclic order. Each pair consists of a methoxy and an octyloxy group, resulting in four isomers. Upon polymerization, straight siloxane bonds link the silicon in the middle of the ring. Consequently, the backbone and the rings form a rigid, incompressible core surrounded by a deformable outer core of the aliphatic groups.

The asymmetric substitution of alkyloxy aliphatic groups prevents crystallization

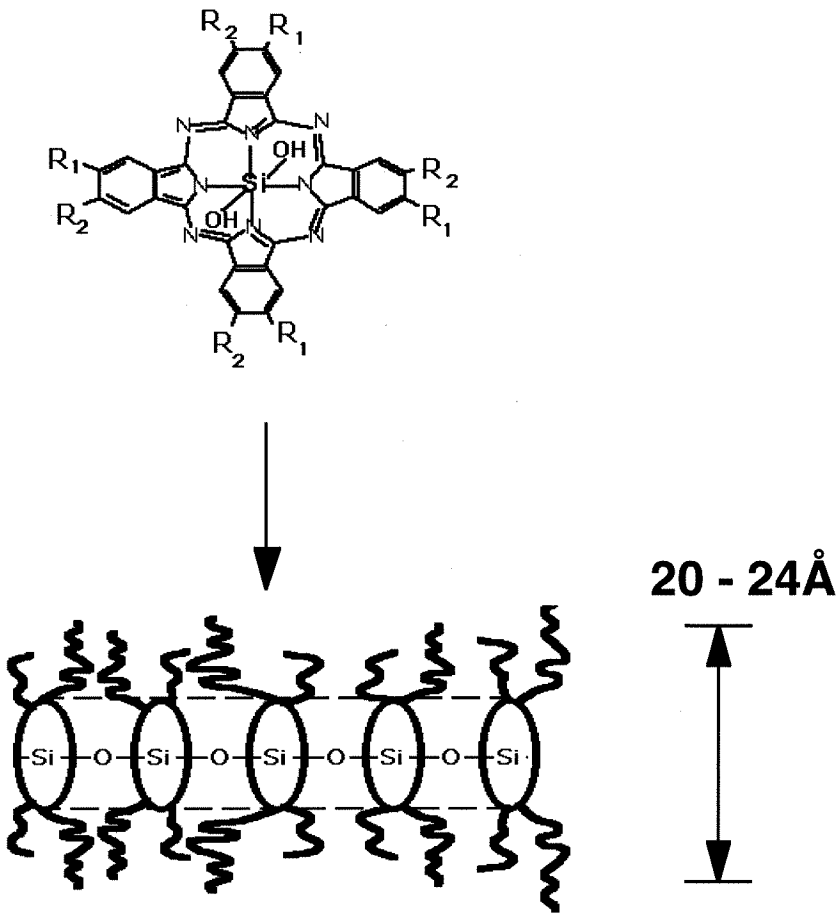

Figure 3.2: Chemical structure of asymmetrically substituted phthalocyaninatopolysiloxane (PcPS) [$R_1 = OCH_3$ and $R_2 = OC_8H_{17}$]. X-Ray diffraction measurements yield inter-layer separation of $\sim 20\mathring{A}$ in transferred films (transfer conditions: $\pi = 25$mN/m, $v = 50\mu$m/s, transfer ratio$\simeq 0.95$), and electron diffraction yields in-plane inter-backbone separation $\sim 25\mathring{A}$ (Source: [64]). The distance per repeat unit along the chain is found to be $\sim 3.4\mathring{A}$ (Source: [60]).

on the air-water interface. Film compression of the monolayer spread on the air-water interface, results in a "dense" phase for $\pi \simeq 15 - 40$mN/m [60, 64]. It is believed that the molecular organization in this phase resembles a nematic liquid-crystal (see Figure 3.3). Further compression from this "nematic-like" state produces film collapse, which unlike most other materials (*e.g.*, simple fatty acids) is progressive and not catastrophic [64]. Crockett *et al.* [64] observe that during this collapse, the

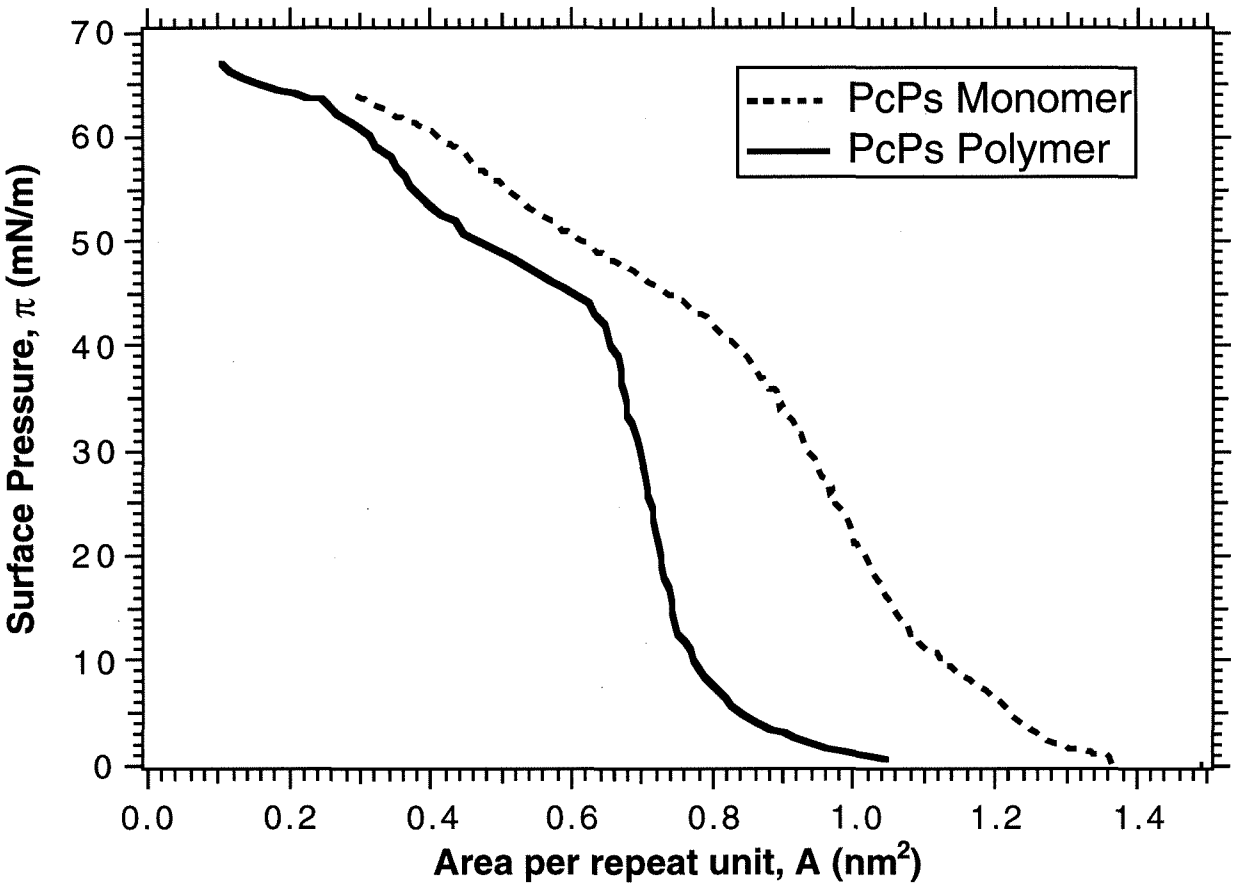

Figure 3.3: Pressure-area isotherm for a PcPS langmuir film (Source: [60]). The approximate degree of polymerization for the polymer is ~ 15.

surface pressure increases linearly with area reduction and speculate that this occurs due to "localized collapse-and-restructuring events."

Wegner and co-workers [60–63] have found that films of asymmetrically substituted PcPS deposited in the "nematic-like" phase exhibit a highly oriented organization of the rodlike molecules. From flow visualization studies of the surface monolayer [65] it is believed that the convergent flow produced in the fluid monolayer during the course of film transfer leads to chain orientation along the dipping axis. This highly organized supramolecular assembly of PcPS has promising applications in optics and

electronics. It has recently been demonstrated that PcPS LB films as thin as a few molecular layers impart a high degree of alignment in an adjacent low-molar liquid crystalline material [66]. Such control of surface alignment is essential in liquid crystalline display technology. Currently this is achieved by rubbing a polymer coated surface, which suffers from problems of dust-contamination, static charge generation and stress-damage to underlying, sensitive transistor circuits. Therefore, use of LB films to attain liquid crystal alignment is an attractive and technologically superior alternative.

However, the present knowledge about the structure-property relations governing the state of alignment in these LB films is poor. As mentioned earlier, studies of molecular order in films as thin as a few nanometers have been severely hampered by lack of adequate experimental characterization techniques. Development of polarization-modulation laser scanning microscopy (PMLSM) provides a powerful means to study the processes and properties controlling alignment in PcPS LB films, non-invasively and on commonly used substrates. Furthermore, the phthalocyanine-based rodlike polymers are ideal candidates because the phthalocyanine molecule is a dye that is optically anisotropic. PcPS absorbs strongly under visible light and exhibits a maximum absorption anisotropy at wavelengths around 550 nm. Polymeric arrangement of the phthalocyanine rings, co-facially with siloxane linkages, results in a high anisotropy with a principal axis along the rod. Thus, using PMLSM, we can image the in-plane molecular orientation and order.

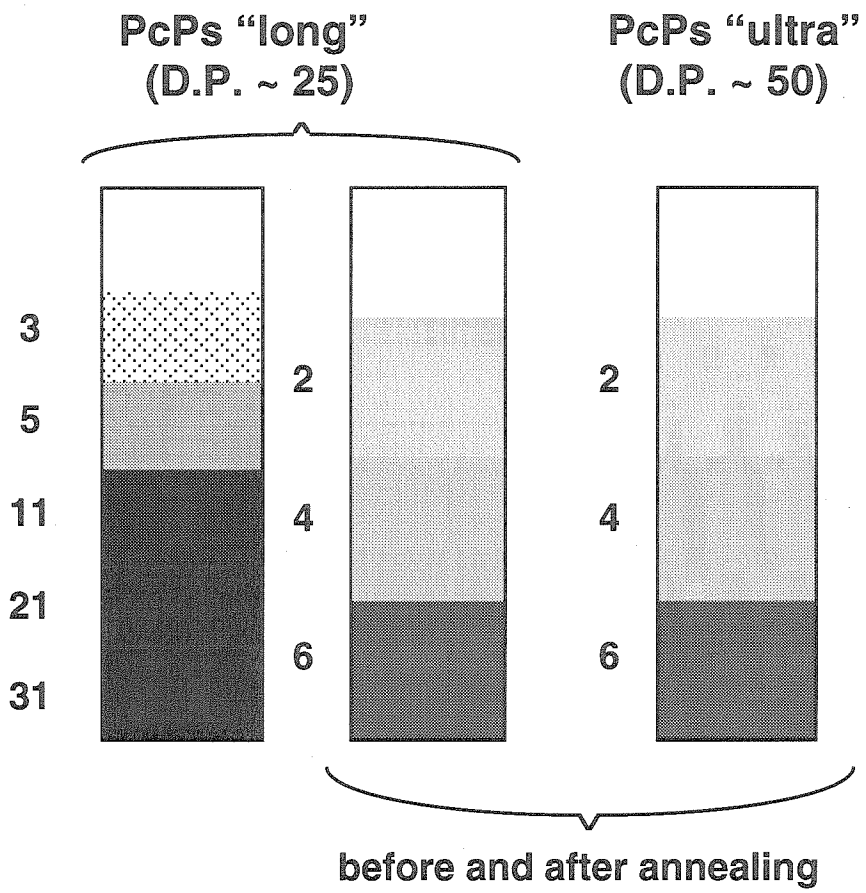

Figure 3.4: Sample LB films to study interplay of molecular weight, layer thickness and thermal annealing in affecting the degree of molecular order.

3.3 Results and Discussion

PcPS molecules were spread on a Lauda film balance[1] at 6° C, and the monolayer was compressed to a deposition surface pressure of 25 mN/m. Deposition of films with varying number of layers onto microscope glass slides was accomplished by dipping the slide to different lengths at a speed of 10 mm/min (Figure 3.4). Each dipping cycle included a 20min upper stop relaxation (drying) time with nitrogen flowing. To study

[1]Synthesis of PcPS and the LB deposition was done by Dr. Andreas Ferencz during his doctoral studies with Professor G. Wegner at the Max-Planck-Institut für Polymerforschung

the interplay of molecular weight, layer thickness and thermal annealing in affecting the state of alignment, thin films were prepared for two molecular weights: PcPS-25 with approximately 25 repeat units ($\sim$ 10 nm long) and PcPS-50 with approximately 50 repeat units ($\sim$ 20 nm long).[2] For characterization of the enhancement of molecular alignment on thermal annealing and its relation to molecular weight and layer stacking, we compared unannealed samples with samples annealed at 120°C for 1 hour for both sets of polymers and films with a 2, 4, and 6 series of molecular layers (Figure 3.4).

Dichroism images were recorded at the boundaries between the bands. All the images discussed in this section were acquired in 480 $\times$ 256 pixel frames, and recorded at a rate of 64 seconds per frame. In comparison to the earlier prototype differential polarization microscopes, the present method provides at least two orders of magnitude greater speed (the previous microscopes required over an hour to obtain a map of both absorption anisotropy and its orientation).

3.3.1 Order and Orientation in PcPS LB Films

The dichroism field observed at the boundary between a region covered with 31 molecular layers ($\sim$ 682 $\AA$) and a region covered with 21 layers ($\sim$ 462 $\AA$) of PcPS is shown in Figure 3.5(a). The absorption anisotropy (ν) has been color coded for enhanced viewing contrast from red to blue (as ν increases) as shown in the accompanying color scale. The dichroism fields at the 21/11 layer boundary, 11/5 boundary and

[2]These values for molecular weight are estimated from high-resolution electron micrographs.

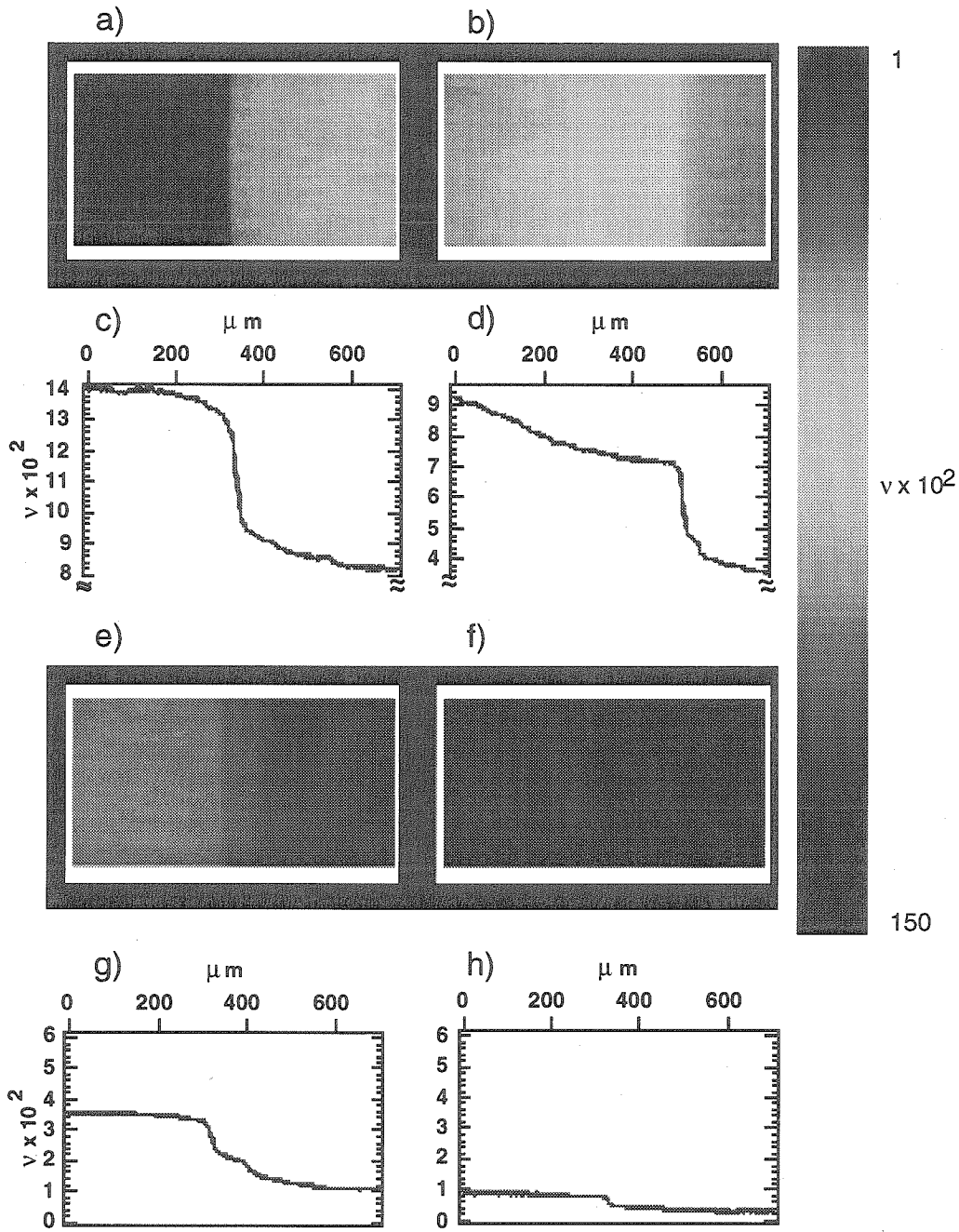

Figure 3.5: Linear dichroism field at the boundaries between two regions covered with different number of molecular layers (refer to Figure 3.4). The absorption anisotropy has been color coded from dark red to dark blue as the magnitude increases (see color scale). Also shown are graphs for the vertical line averages in each image of the magnitude of dichroism as a function of distance along the image. (a) and (c) represent the boundary between 31 and 21 layers, (b) and (d) represent the boundary at 21-11 layer interface, (e) and (g) represent the boundary at 11-5 layer interface, (f) and (h) represent the boundary between 5 and 3 layers.

5/3 boundary are shown in Figure 3.5(b), (e) and (f) respectively. The absorption anisotropy shows a monotonic decrease from 31 molecular layers to 3 layers in proportion to the number of layers. The relative decrease in ν across a boundary is much larger when the decrease in the thickness across the boundary is greater. This is seen clearly by the higher color contrast that corresponds to a step of 10 layers (~ 220 $\mathring{A}$) in the the dichroism images in Figure 3.5(a) and (b), compared to a lower contrast for a step of 6 layers (Figure 3.5(e)) and one that is nearly negligible for a step of two molecular layers (Figure 3.5(f)). The decrease in ν in going from 31 layers to 3 layers and the steep drop at each boundary is seen easily in the graphs of the vertical line averages for each image, shown in Figures 3.5(c), (d), (g) and (h) for the dichroism images Figures 3.5(a), (b), (e), and (f), respectively.

Multiple layers are built up on the foundation of a monolayer on the glass substrate by withdrawing and dipping the slide up and down through the Langmuir monolayer, with each cycle depositing two layers (see Figure 3.4). Ideally, the boundary between the two regions would be sharp, if the dipping process were carried out to precisely the same depth. However, we see that while the boundary is fairly sharp at the 31 layer-21 layer interface, there is a stair-step transition between the two regions in Figure 3.5(b) (21-11) and (e) (11-5), as also evident in the corresponding graphs of the line average (Figures 3.5(c) and (g)). This stair-stepping is more pronounced in the 11-5 layer boundary than in the 21-11 layer boundary, and from the relative heights of the two steps in Figure 3.5(g) we can surmise that the larger step corresponds to a decrease of 4 layers in thickness and that the next step to a decrease of 2 layers. Thus, the narrow

orange band, about 120 micron wide, in Figure 3.5(e) corresponds to a region with 7 molecular layers. Similarly, the narrow yellow band in Figure 3.5(b) appears to be a region of 13 molecular layers about 60 micron wide. The fact that the microscope can image the boundary between a region with 5 molecular layers and 3 molecular layers, and detect these bands shows that it can resolve differences in anisotropic absorption that correspond to the contribution of just two molecular layers[3] and image the non-uniform build up of the LB film. These images represent the first spatially resolved measurements of optical anisotropy in such thin Langmuir-Blodgett films.

Measurement of the angle of orientation of linear dichroism at each pixel allows us to construct a similar image displaying to the orientational distribution in the sample. The orientation image for the boundary between 31 and 21 molecular layers is shown in Figure 3.6. The background color represents the absorption anisotropy (color scale as is shown in Figure 3.5). In the foreground the orientation of the dichroism, and hence the mean direction of the polymer backbone, is shown by apolar vectors. The mean orientation angle lies along the transfer direction, and the whole field exhibits strong and uniform ordering. The orientation images corresponding to the boundaries between 21-11, 11-5 and 5-3 layers are very similar. In comparison to earlier macroscopic measurements of the average orientation in LB films [63] of PcPS using grazing-incidence reflection infrared (GIR-IR) spectra and polarized UV-VIS spectra, our measurements reveal that the molecular orientation is spatially uniform along the transfer direction, even on a microscopic scale. This is consistent with recent results

[3]With the present sensitivity of the instrument we were not able to resolve a monolayer

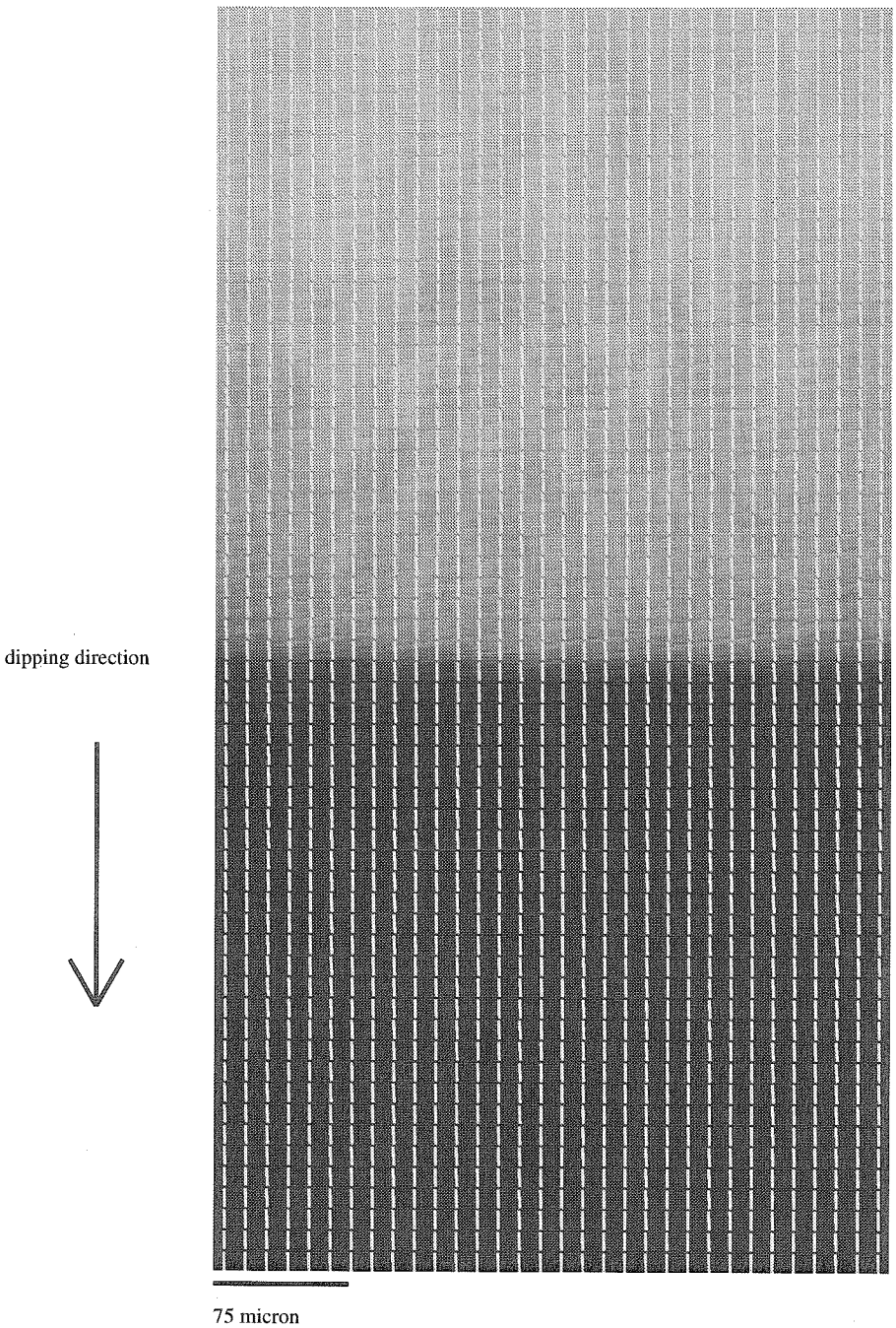

Figure 3.6: The image shows the boundary between a region that is uniformly covered with 31 molecular layers of the polymer (upper half) and a region uniformly covered with 21 layers (lower half). The background shows the absorption anisotropy in a color code from dark red to dark blue as the magnitude increases. The color scale used here is shown in Figure 3.5. The foreground shows the orientation angle of the dichroism, which coincides with the mean direction of alignment of the backbone of the hairy-rod polymer. The orientation image is shown on a much coarser resolution to facilitate viewing. Each apolar vector represents the average orientation in a 8×8 pixel square, and each pixel is $1.5\mu m \times 1.5\mu m$.

by high resolution transmission electron microscopy (TEM) of LB films of PcPS and polyphthalocyaninato-germanoxane (PcPG) [12, 13], that reveal an invariant mean orientation of the polymer backbone along the transfer direction on length scales of over 500 nm.

3.3.2 Interplay of MW, Layer Thickness and Annealing

The structure of polymeric LB films has important implications on their application, and this structure depends critically on a number of factors that include molecular properties, dynamical processes during deposition and interaction with the substrate. In particular, for rod-like polymers, few experiments exist that probe this dependence. Having successfully demonstrated that PM-LSM can be used to probe alignment within few molecular layer thick films, we focus our attention on elucidating these dependencies.

The series of films having 2, 4 and 6 deposited layers of PcPS-25 also show extremely homogeneous orientational order, as indicated by the uniformity of ν (Figure 3.7a through f). This homogeneous order improves in general upon thermal annealing, evident in the increase in the anisotropic absorption between Figure 3.7a through c and Figure 3.7d through f. However, this increase in ν for the molecular layers is modified by the interaction with the underlying surface. This effect is manifested as an almost imperceptible increase in ν for the region covered with two molecular layers (Figure 3.7a). In contrast, the degree of molecular reorientation is larger in successive layers of the LB film (Figure 3.7b and Figure 3.7c). This change

can be seen easily from the line averages in Figure 3.7g, where the step jump in going from bare glass to a region of two layers remains almost unchanged after annealing, and is in distinct contrast to the step heights in Figure 3.7h. Intimate interaction between the substrate surface and adjacent layers strongly affects the refinement of order, and the strength of this interaction decays with layer thickness (Figure 3.8a). Past as few as four layers, the multilayer assembly achieves bulk orientational order that become insensitive to the presence of the substrate[4].

The longer PcPS-50 also exhibits increasing ν with increase in number of layers from two to six. However, in comparison to the shorter PcPS-25, the anisotropy of absorption for each film thickness is significantly lower in PcPS-50 films. Figures 3.9a, 3.9d and 3.9g show that the region covered with two molecular layers shows almost no increase in ν upon annealing and that only a slight increase becomes apparent in layers that are built up on a foundation of a few multilayers of PcPS (Figures 3.9b, e and h, and Figures 3.9c, f and i). Because longer rodlike molecules generally have a higher degree of local order, this decrease in alignment with increasing molecular weight suggests a reduction in the mesoscale order in transferred films from PcPS-25 to PcPS-50. The order in the transferred film of PcPS-50 is not only lower than that of PcPS-25, but also is less amenable to refinement with annealing (Figure 3.8b).

To explain these results we need to understand the origin of mesoscale order in LB

[4]Authors of a previous study of PcPS have speculated upon the importance of surface interaction on film morphology [64]. Transmission electron microscopy (TEM) studies of films deposited directly on carbon covered grids as well as films (22 layer thick) transferred from glass onto the TEM grids showed that layers in the former case were less well defined and more disordered than those transferred from glass substrates. Crockett *et al.* speculated that poor interaction between the surface layer and the carbon covered substrate led to unstable films during successive dipping and thus, to more disorder.

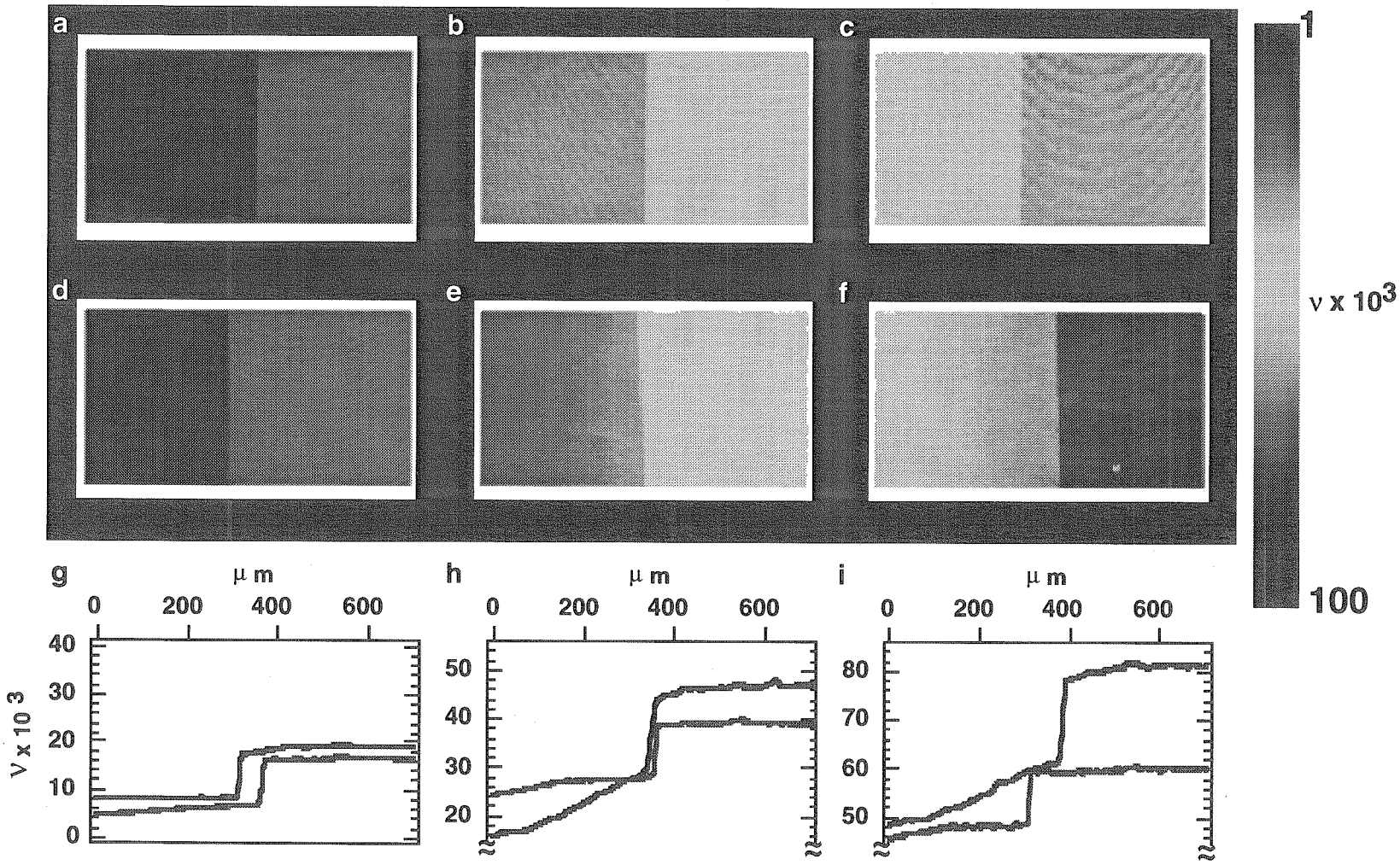

Figure 3.7: Linear dichroism field at the boundaries between two regions covered with different numbers of molecular layers of PcPS-25. The anisotropy in absorption (ν) has been color coded from dark red to dark blue as the magnitude increases (see color scale). (a-c) Images of the unannealed sample. (d-f) Images after annealing. (g-i) Vertical line averages of ν as a function of distance along the image (red, unannealed sample; blue, annealed). In a, d, and g, the boundary is between bare glass and two layers. In b, e, and h, the boundary is at two to four layer edge. In c, f and i, the boundary is at the four to six layer edge.

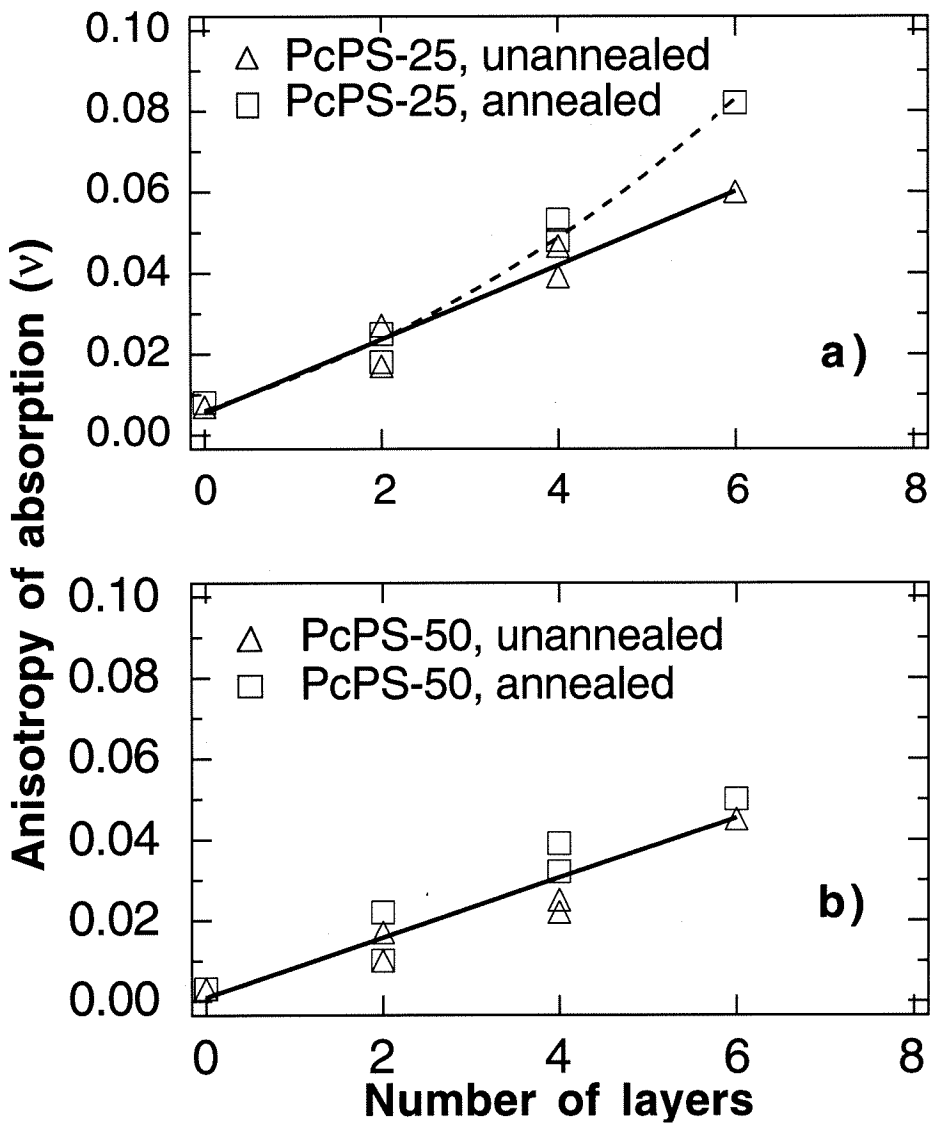

Figure 3.8: Anisotropy of absorption (ν) for different layer thickness in as-deposited and annealed LB films of (a): PcPS-25 and (b): PcPS-50. The solid and dashed curves are drawn to guide the eye.

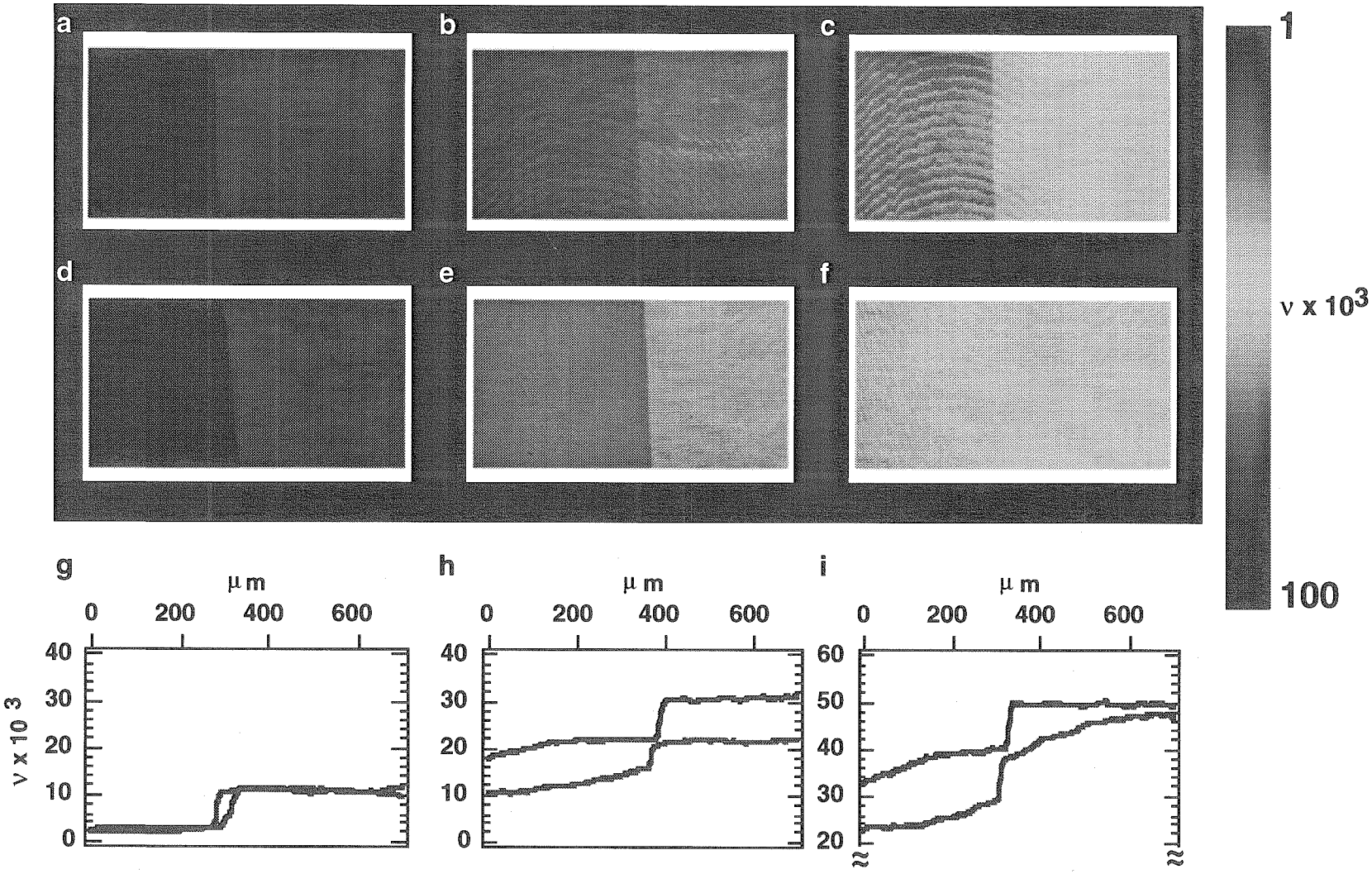

Figure 3.9: Linear dichroism field at the boundaries between two regions covered with different numbers of molecular layers for the PcPS-50. The anisotropy in absorption has been color coded with the same scale as in Fig.3.7. (a-c) Images of the unannealed sample. (d-f) Images after annealing. (g-i) Vertical line averages of ν as a function of distance along the image (red, unannealed sample; blue, annealed). In a, d, and g, the boundary is between bare glass and two layers. In b, e, and h, the boundary is at two to four layer edge. In c, f and i, the boundary is at the four to six layer edge.

films and the factors controlling it. Towards this end, details of the transfer process and the nature of surface flow are critical. When a monolayer is compressed in the Langmuir trough using sliding barriers, the flow of surface layer depends intricately on the exact experimental conditions, the properties of the molecules and the structure in the film at a given surface pressure. Experimentally it is observed that rheological properties such as the viscosity can have important consequences on the nature of flow of the surface layer during compression and deposition processes [67–71]. The trough design is another important factor governing the uniformity of distortion of the surface layer [72, 73]. The dipping speed during deposition, substrate orientation and its dimensions relative to the trough area play a critical role in affecting the nature of surface flow [65, 74–76]. Quite naturally, the response of the surface layer to flow distortion is a strong function of the chemical and physical properties of the molecules, their intermolecular interaction and their packing arrangement.

In the compressed PcPS film, it is believed that the rodlike molecules are packed in assemblies or domains each of which possesses uniform orientation. However, these domains are expected to be misaligned with respect to each other. During the deposition process, deformation of the fluid layer produces a convergent flow of these assemblies near the substrate. It is speculated that the deformation forces during flow tend to elongate and break up domains in the spread monolayer and reorient the molecules so that there is macroscopically uniform orientation, which gets transferred to the deposited film [65, 68, 74]. We believe that when the molecular weight of PcPS is varied, the behavior of the rodlike molecules will differ with deformation of the

surface layer. Consequently, changes in the morphology of PcPS films should occur as the nature of surface flow varies.

For higher molecular weights (other things being equal), *i.e.* with increase in the length of the rodlike molecule, we expect the surface deformation to be less fluid within the time-scale of flow during deposition[5]. Such a solid-like interaction could hinder molecular reorientation from the distortional forces, and result in transfer of intact parts of the domains to the substrate. Consequently, the deposited films would exhibit a higher mesoscale disorder (*c.f.* lower ν in PcPS-50 films). Thermal treatment may reduce misalignment within domains in the deposited film and improve the mesoscale order. However, if these domains have a wide distribution of orientation, no macroscopic improvement in alignment would be achieved by annealing (*c.f.* no improvement in ν upon annealing in PcPS-50 films).

It is clear from the foregoing discussion that more experiments are needed for understanding the origin and control of alignment in PcPS LB films. In this context, our work of developing polarization-modulation laser-scanning microscopy is important for both the meaningful measurement of monolayer properties, and in the understanding of orientation effects in ultrathin films. Results from our work on PcPS suggest directions for future work that are valuable towards elucidating the relationship between surface flow and film morphology. In particular, considerable intrigue

[5]Simple theoretical modeling of the flow of surface layer as ideal fluid and the substrate as a finite-line sink has been performed previously [65, 75]. Minari *et al.* have used such modeling to estimate the in-plane anisotropy in LB films (mixed systems of merocyanine and fatty acid) by taking into account the viscoelastic nature of a condensed monolayer using Bingham plasticity. Their results suggest that orientation of the aggregates of chromophores depend on $V_d/(Da)$ where V_d is the deposition velocity, a is the width of substrate and D is the rotatory diffusion coefficient that is a function of surface viscosity and length of the aggregate.

remains about the nature of changes in alignment within a film that result upon altering surface flow by using different deposition speeds (*i.e.* changing flow time-scales), choosing materials with different physical properties and studying these with respect to a range of substrates. Resolution of these questions hinges critically upon visualization of the molecular organization on the air-water interface and its reorganization during compression and deposition. PMLSM's imaging capability together with its vastly improved speed represents a significant step towards this direction. We believe that future work focusing on these issues of structure-property relations will be vital towards optimization of Langmuir-Blodgett film fabrication and improvement of the film quality.

Chapter 4

Development of Coherent Macroscopic Order in Lamellar Diblocks

4.1 Flow Alignment in Diblocks: Introduction

Coherent macroscopic order in intrinsically anisotropic materials is an essential requirement for diverse electronic, optical, separation and biomedical applications. Consequently, it is highly desirable to manipulate structure in a wide range of new materials to induce molecular and mesostructural alignment. One means to affect such structural rearrangements in complex biological and synthetic materials is by using flow fields. However, achieving this in a rational and optimal manner necessitates understanding the nature of the strong coupling between applied deformation and the local microstructure. In this chapter, we focus on flow induced alignment in microphase separated diblock copolymers, in particular lamellar polymers. Our goal is to acquire a fundamental insight into the complex dynamics resulting from a distribution of lamellar orientations, and we propose to achieve this objective by monitoring flow alignment, in *real time* and *in-situ.* We expect that such an insight would serve to clarify certain features of shear orientation and viscoelastic behavior that are common to the broad class of layered systems spanning smectic liquid crystals, surfactant membranes, and layered polymer composites [35–39].

In most block copolymers above an order-disorder transition temperature (T_{ODT}) the material exists in a disordered, homogeneous state. Moving through T_{ODT} in the absence of an applied field leads to local segregation into periodic microstructures (ordered, microphase separated state) that are randomly oriented. Symmetry breaking fields such as electric fields and flow fields can induce "single-crystal" like order on global length scales in these microphase separated block copolymers

[22, 28, 30–33, 39, 77].

When a shear field is applied to diblock copolymers that exhibit a lamellar morphology, three states of global alignment can be envisaged (Figure 4.1). Only two, with layer normals along the shear gradient direction (parallel) and with layer normals along the vorticity direction (perpendicular), are stable and can be induced using large amplitude oscillatory shear flows [28]. Intriguingly, these two distinct microstructural arrangements can be achieved by a mere change in shear frequency at the same temperature and strain amplitude [28, 78]. In spite of more than two decades of theoretical and experimental work, the underlying causes and mechanisms of alignment and the selection of one alignment over the other remain elusive [22, 28, 30–34, 39, 77–79].

Much of the previous experimental work has focused on two classes of systems: (a) polystyrene-polydiene block copolymers (where the diene may be either butadiene or isoprene) with the components having vastly different glass transition temperatures and the experimental temperatures not much greater than the glass transition temperature of the styrene-rich phase [22, 24, 26, 34, 39, 40, 79, 80]; and (b) well-entangled, polyolefin diblocks, such as PE-PEE, PE-PEP and PEE-PEP (PE=polyethylene, PEE=poly(ethylethylene), PEP=poly(ethylene-alt-propylene) wherein the components have similar glass transition temperatures and flow alignment is performed at temperatures much greater than either component glass transition temperature [28, 29, 78, 81, 82].

The early shear experiments on lamellar styrene-diene block copolymers induced alignment in the parallel direction [24, 26], but more recent experiments on polyolefin

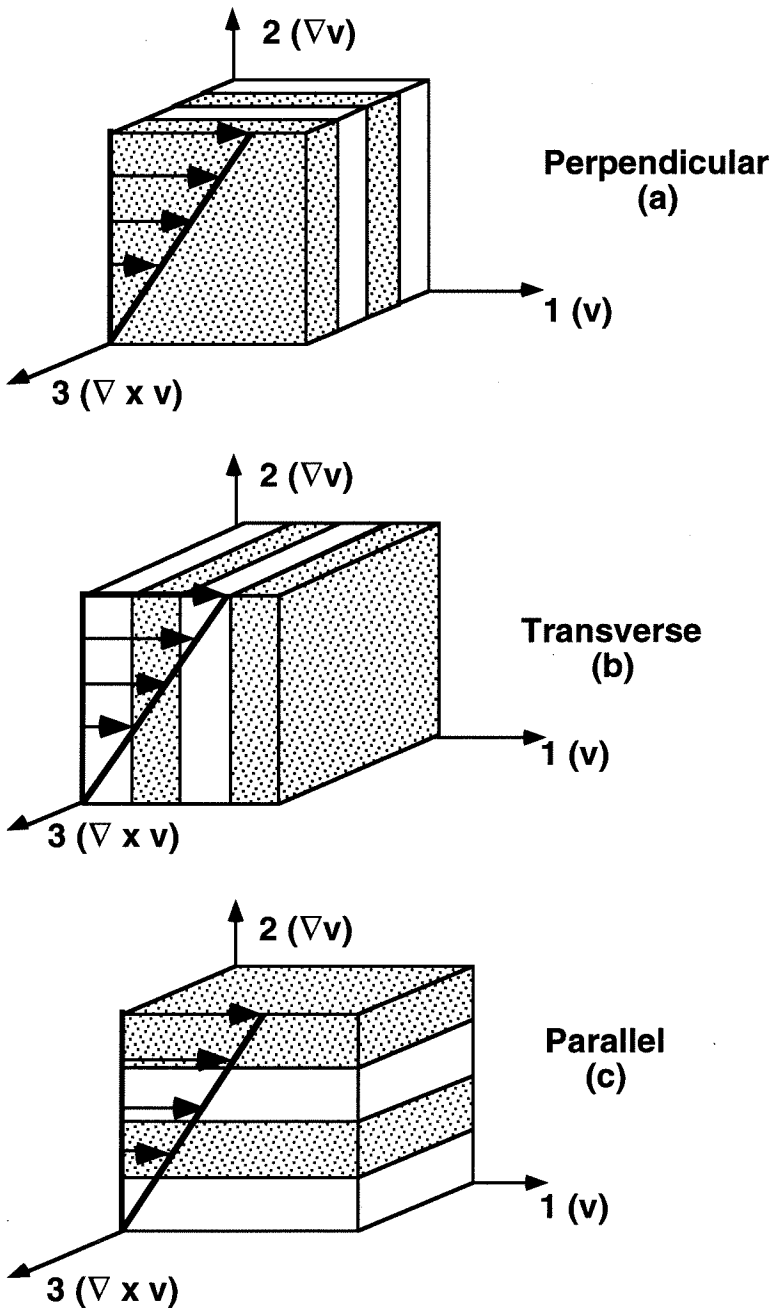

Figure 4.1: Schematic of lamellar orientations for diblock copolymers.

diblocks showed that perpendicular alignment could also be produced [28]. Koppi and coworkers [28] found that for lamellar polyolefin diblocks, large amplitude reciprocating deformations at shear frequencies in the dynamic regime dominated by the layered microstructure and at temperatures near the order-disorder transition resulted in perpendicular alignment, while parallel alignment was produced at lower reduced shear frequencies over a broader range of temperatures. More recently, Winey and coworkers [34, 39, 40] working with a PS-PI lamellar diblock (12.5k-9.5k, $T_{ODT} = 152°C$), achieved perpendicular alignment near the order-disorder transition (*e.g.* $\omega = 10$ rad/s, $T = 144°$ C, $\gamma_o = 100\%$), and parallel alignment at lower temperatures (*e.g.* $\omega = 0.1 - 100$ rad/s, $T = 98°$ C, $\gamma_o = 2 - 5\%$). This differed from the polyolefin case wherein parallel alignment was restricted to lower reduced frequencies than those inducing perpendicular alignment.[1]

In early studies [24, 26], where only parallel alignment was found, it was proposed that flow alignment could proceed by mechanisms that include grain rotation, selective melting of grains and defect migration. To explain the occurrence of parallel as well as perpendicular alignment, Koppi and coworkers [28] speculated that perpendicular alignment was achieved because "the interfacial material is deformed by the vorticity component of the velocity gradient in all but the perpendicular orientation." In contrast, they argued that parallel alignment occurred by "breaking and reforming the lamellae individually through the movement of dislocations (or disclinations)."

As mentioned in the introduction (Chapter 1), these ideas about alignment mech-

[1]Parallel alignment in PS-PI has recently been reported [80] at frequencies lying below and above those at which perpendicular alignment is induced.

anisms were based primarily on the microstructure observed after alignment using small angle neutron scattering (SANS) [28], transmission electron microscopy (TEM) and small angle x-ray scattering (SAXS) [34, 40]. Apart from the possibility of artifacts induced during the cooling, cutting and mounting processes for sample preparation, such characterization does not provide any information on the molecular and microstructural dynamic responses during flow alignment. This information is vital to formulate mechanisms of flow alignment and to discriminate among existing ideas. Thus, real time, *in-situ* studies are essential to understanding the mechanism of flow alignment - a prerequisite for rational control of the macroscopic ordering in block copolymers and other mesostructured materials.

Studies with a focus on *in-situ* measurements during shearing of block copolymers recently appeared in the literature [78, 83–85]. However, the SANS and SAXS studies [83, 85] by Balsara *et al.* and Okamoto *et al.* reported scattering profiles averaged over periods of several minutes ($\sim$ 8-20 minutes), thus tracking changes in the microstructure on that time-scale. Both investigations examined only a few conditions of alignment. In contrast, *in-situ* stress-optical methods used by Kannan *et al.* to examine alignment processes in a PEP-PEE diblock copolymer, provided a much higher time resolution ($\sim$ 0.1s) [78]. However, in PEP-PEE, flow birefringence is sensitive to chain orientation, since the intrinsic contribution dominates; at high frequencies, where conformation distortion occurs, this precludes determination of the lamellar orientation distribution during development of perpendicular alignment.

To study the grain orientation during alignment, we investigate a lamellar PS-

PI block copolymer using *in-situ* rheo-optical measurements. In PS-PI, apart from probing distinctly different regimes of alignment than the polyolefin, we can explore the role of material properties (PS-PI *vs* PEP-PEE) and viscoelastic contrast (PS *vs* PI). In the styrene-isoprene diblock, the birefringence measurements can be directly related to the grain orientation distribution, since form contribution dominates. Thus, we can study the coherent macroscopic order as it develops during oscillatory shear. The higher time-resolution of rheo-optical measurements proves extremely valuable as significant changes in microstructure occur initially within times of less than a minute. Using transient birefringence measurements, we perform a systematic study of the effects of shear frequency, strain amplitude and temperature on the rate, the route and the final direction of alignment.

4.2 Material, Apparatus and Methods

A nearly symmetric polystyrene-polyisoprene diblock copolymer with $M_w \simeq 20$ kg/mol, and $\frac{M_w}{M_n} \leq 1.06$ was prepared by anionic synthesis using standard techniques. Clean material was obtained by filtering a solution of the polymer in toluene through a 0.2μm teflon filter, followed by precipitation in methanol and vacuum drying. The order-disorder transition temperature (T_{ODT}) was determined rheologically (Figure 4.2). Using a temperature sweep at a rate of 1°C/min and in steps of 1°C, the dynamic moduli at different temperatures were measured with oscillatory shear at 10 rad/s and 2% strain. At $T_{ODT} \simeq 164$°C,[2] both moduli (G', G'') exhibited a steep de-

[2]For yet unknown reasons, we observed T_{ODT} of 171 °C and 164 °C for two different batches for the same polymer sample. All the experiments reported in this dissertation were performed with

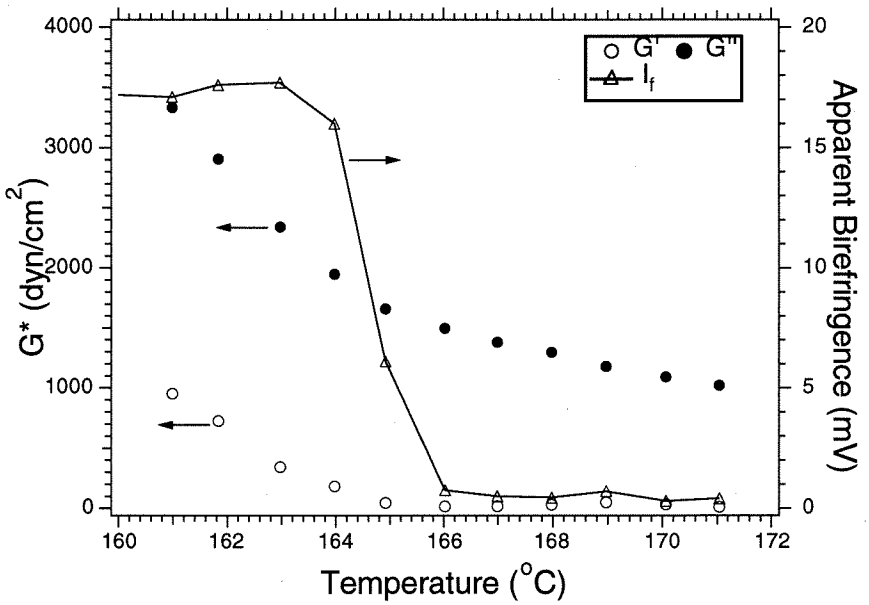

Figure 4.2: Determination of the order-disorder transition temperature (T_{ODT}).

crease, which was more pronounced for G'. Similar determination revealed a typical hysteresis behavior upon cooling with the transition temperature a few degrees lower than that during heating. The order-disorder transition temperature is also manifested in optical measurements as a steep decrease in the "apparent birefringence."[3]

The mechanical and optical properties of this block copolymer were characterized using the rheo-optical apparatus described in section 2.3.2. All experiments were performed under an inert nitrogen atmosphere using the 'shear-sandwich' geometry, with light propagation along the velocity gradient direction (axis 2). This allowed us to measure the projection of the anisotropic refractive index tensor in the plane formed by the flow direction (axis 1) and the vorticity axis (axis 3). The present rheo-optic instrument measures the sign of birefringence along with its magnitude.

---

the latter.

[3]In the microphase separated state for block copolymers a small apparent birefringence results from depolarization of the polarized light upon transmission through a collection of randomly oriented lamellar grains.

Experiments were performed with the sample loaded in a tool with a gap of 0.26 mm and rectangular plates (15.92 mm $\times$ 12.65 mm). The optical path length was twice the gap width, *i.e.* 0.52 mm. We primarily used a red helium-neon laser at a wavelength of 633 nm.

For a highly birefringent sample (with little or no dichroism), the measurable optical property was $\sin\mu$, where the retardation $\mu = \frac{2\pi d}{\lambda}\Delta n_{ij}$, with d the optical path length, λ the wavelength of the incident light, and Δn_{ij} the birefringence in the i,j-plane (1,3-plane in our work). Because the principal value of μ was obtained by inverting the sine function, errors are large in the vicinity of $\mu = (2m+1)\pi/2$. However, the uncertainty in the precise value of μ in the time intervals where μ is near $(2m+1)\pi/2$ does not alter the conclusions of this work.

We used two types of oscillatory shear protocols: (1) frequency sweeps at strain amplitudes small enough to characterize the linear viscoelastic response of the sample before and after alignment, and (2) prolonged, large amplitude ($10\% \leq \gamma_o \leq 110\%$) oscillatory shear at a fixed frequency and temperature to induce macroscopic alignment of the microstructure. To establish a reproducible initial condition before each alignment experiment, the sample was heated well into the disordered phase (180°C) and allowed to equilibrate at that temperature for 15-20 minutes. The sample was then cooled to the desired temperature in the ordered state and equilibrated for 15 minutes. This procedure resulted in a reproducible initial state, confirmed by frequency sweep measurements before each alignment process.[4] Once the sample was

[4]Surface ordering effects have been observed in the literature [83]. We are unable to comment on these from our birefringence measurements. Based on the random morphology studied by Winey *et al.* [40], we interpret the initial state as unaligned.

loaded in the shearing tool, uninterrupted measurements over several weeks were carried out by simply cooling and reheating the same sample to minimize relative errors (*e.g.*, variations in sample thickness in successive experiments, optical-train calibration, etc.). Clean terminal behavior in the disordered state after completion of the whole suite of experiments, and GPC traces of the sample showed no evidence of any thermal or oxidative degradation, or cross-linking. Furthermore, we saw neither a broadening nor a shifting of the T_{ODT} over the course of weeks of experimentation.

4.2.1 Stress and Birefringence

In shear flow, by symmetry, the shear stress (σ_{12} in the coordinate system described above) is an odd function of the strain. For oscillatory shear $\gamma(t) = \gamma_o \sin \omega t$, if γ_o is small, the leading term in an expansion of $\sigma_{12}(t)$ in the harmonics of ω dominates. Thus, σ_{12} is expected to be sinusoidal with the same frequency (ω) as the applied strain. When this is the case and when the stress is linear in the strain, we can define storage and loss moduli $G'(\omega)$ and $G''(\omega)$: $\sigma_{12} = \gamma_o[G' \sin \omega t + G'' \cos \omega t]$.

Frequency sweeps to characterize the linear viscoelastic behavior of the block copolymer were performed with small enough strain amplitudes to avoid macroscopic alignment and non-linearity in the stress response. However, this was particularly difficult to achieve at elevated temperatures where larger strains were required to obtain a measurable force response.

In contrast, during "flow-alignment" we used strain amplitudes large enough to produce alignment of the lamellae, but small enough that the stress was dominated

by the fundamental Fourier component and could be described using an effective dynamic modulus G^*_{eff} that changed with time during prolonged shearing. The higher harmonics $(3\omega, 5\omega)$ in the stress response were also recorded.[5]

For PS-PI diblocks in the strongly segregated regime, the form contribution to the birefringence $(\Delta\mathbf{n}_f)$ resulting from the block copolymer microstructure is estimated to be at least three times the intrinsic or "molecular" contribution $(\Delta\mathbf{n}_i)$ [86, 87]. Therefore, in our experiments we expect the form birefringence to dominate: consequently the observed birefringence provides a measure of the lamellar orientation distribution. A beam propagating along the velocity gradient probes the projection of $\Delta\mathbf{n}$ on the 1,3-plane, $\Delta\mathbf{n}_{13}$. Due to flow symmetry, the principal axes of $\Delta\mathbf{n}_{13}$ coincide with axes 1 and 3, so its anisotropy is completely described by the magnitude of the birefringence $\Delta n_{13} = n_{11} - n_{33}$. If a particular orientation of the projection of the lamellar normal in the 1,3-plane were enhanced by oscillatory shear, it would be directed along one of the axes (1 or 3) and would be manifested in Δn_{13}. Thus, the evolution of the steady offset in $\Delta n^{(d)}_{13}$ is sensitive to the development of alignment. In the parallel orientation, the lamellar normal $(\hat{\mathbf{u}})$ points in the velocity gradient direction (axis 2) and is along the beam propagation direction. This results in a zero birefringence in the 1,3 plane for a perfectly aligned parallel state.[6] In contrast,

[5]The ratio of the 3ω component to the 1ω component in the stress response showed a maximum value that ranged from approximately 10% to 5%. It then fell rapidly and during most of the shear alignment process, was within 1%. The 5ω component was an order of magnitude smaller throughout the alignment.

[6]A near zero birefringence can be ambiguous, since it can correspond to any state that has a symmetric distribution about the velocity gradient direction [*e.g.*, parallel alignment, an isotropic distribution of the lamellar grains (either overall or in the 1,3-plane) or a collection of onion-like structures (observed in lamellar lyotropics [88])]. Therefore, we interpret $\Delta n^{(d)}_{13}$ in the context of the overall alignment trajectory, and in combination with the changes in the mechanical properties (G', G'') of the sample. We also draw on previous structural studies using TEM/SAXS for a very

in perpendicular alignment the layer normal ($\hat{\mathbf{u}}$) points along the vorticity direction (axis 3); for PS-PI, this corresponds to positive Δn_{13}, since the form contribution has a higher index along the layers. Similarly, a large, negative 1,3-birefringence corresponds to the "transverse" orientation, with layer normal ($\hat{\mathbf{u}}$) along the flow direction (axis 1).

4.3 Results

4.3.1 Dynamic Moduli of Disordered and Unaligned Ordered Phases

Time-temperature superposition at a reference temperature of 120°C was used to construct dynamic moduli, G' and G'' master curves that span nearly seven decades in reduced frequency (Figure 4.3a and 4.3b). The data measured at different temperatures using small amplitude oscillatory shear[7] were shifted only along the frequency scale to construct the master curves (a_T reported in Table 4.1). The dynamic moduli at temperatures near and above the ODT are also shown in the same figure.[8]

similar polymer system [34], which clearly establish existence of aligned lamellar morphology after large-amplitude oscillatory shear and correlate the aligned state with changes in G' and G''.

[7]Testing at $T \leq 110$°C (*i.e.* $5.5 \leq a_T\omega$ [rad/s] $\leq 66 \times 10^3$) was performed with $\gamma_o \leq 0.003$. For $T \leq 130$°C (*i.e.* $1 \leq a_T\omega$ [rad/s] ≤ 24), strains with $\gamma_o \leq 0.02$ were used. Higher temperatures required larger strains; by $T \simeq 160$°C, strains as large as 12% were used at the lowest ω. At $T \geq 164$°C the materials is disordered and linear behavior is observed for all strain amplitudes used.

[8]It was not possible to superimpose the results of the frequency sweep [100-10 rad/s ($\gamma_o = 0.03$) and 10-1 rad/s ($\gamma_o = 0.12$)] at 160°C (Figure 4.3a). This could be due to the increasing strength of composition fluctuations as T_{ODT} is approached [82, 89, 90]. The discontinuity in G' at the overlap frequency of 10 rad/s is due to the non-linear effect of strain amplitude.

T(°C)	a_T $T_o = 120$°C	T(°C)	a_T $T_o = 120$°C
90	660	160	0.0114
100	45.5	164	0.0068
110	5.5	166	0.006
130	0.24	168	0.005
140	0.077	170	0.0045
150	0.034		

Table 4.1: Frequency shift factors for PS-PI in the ordered but macroscopically unaligned state

In the ordered phase, both G' and G'' roughly follow a power law scaling with frequency [39, 82, 91, 92], which can be approximated as $\omega^{0.5-0.7}$. The disordered state dynamic moduli show typical homopolymer-like terminal behavior with $G' \propto \omega^2$ and $G'' \propto \omega^1$ (Figure 4.3a and 4.3b).

We define two critical frequencies below which the relaxation dynamics are hypothesized to be dominated by relaxation modes of the microdomain structure [82]. The critical frequency based on the loss modulus (ω_c'') is taken to be the frequency below which the ordered and disordered loss moduli fall on different curves: $\omega_c'' \approx 0.5$ rad/s at $T = 120$°C. For the storage modulus, we estimate the value of ω_c' by extrapolating the disordered state data ($\omega_c' \approx 3 - 7$ rad/s at $T = 120$°C, Figure 4.3a). The uncertainty results from the rather long extrapolation of the disordered state data required to estimate ω_c'.

In the following sections, we describe the results of our systematic investigation of the effects of frequency and strain amplitude. We describe first extensive alignment

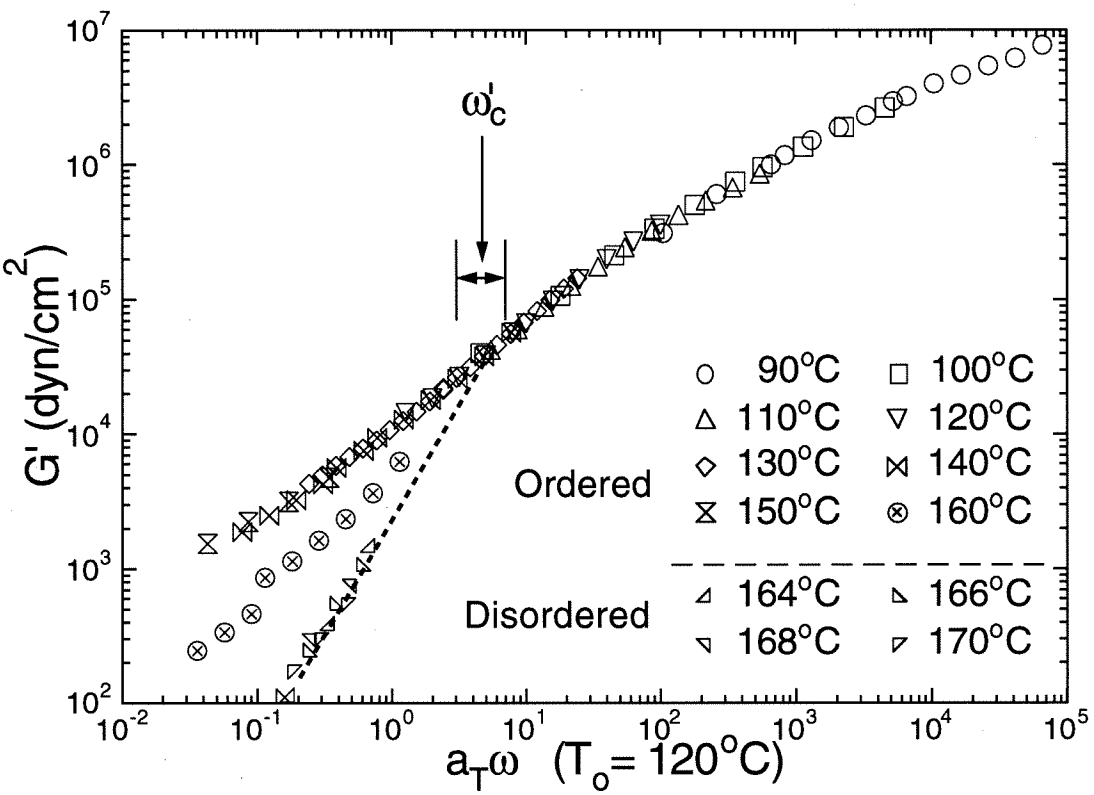

Figure 4.3a: Storage, G', modulus on a shifted frequency scale ($T_o = 120°\text{C}$, a_T given in Table 4.1) for ordered ($T < 164°\text{C}$) but macroscopically unaligned state, and the disordered ($T > 164°\text{C}$) melt. The lateral bar indicates the approximate value of the critical frequency ω'_c (see text).

results from experiments carried out at a single temperature of $120°C$. This choice of temperature permitted us to explore shear alignment to both parallel *and* perpendicular alignment with various shear frequencies and a wide range of strain amplitudes. Thereafter, we permit the temperature to vary as well, and present results from shear alignment at temperatures other than $120°C$.

4.3.2 Effect of Frequency (ω) on Evolution of Alignment

In this section flow alignment experiments at a single temperature of 120°C are described. The final state of alignment was characterized by the birefringence (Δn_{13})

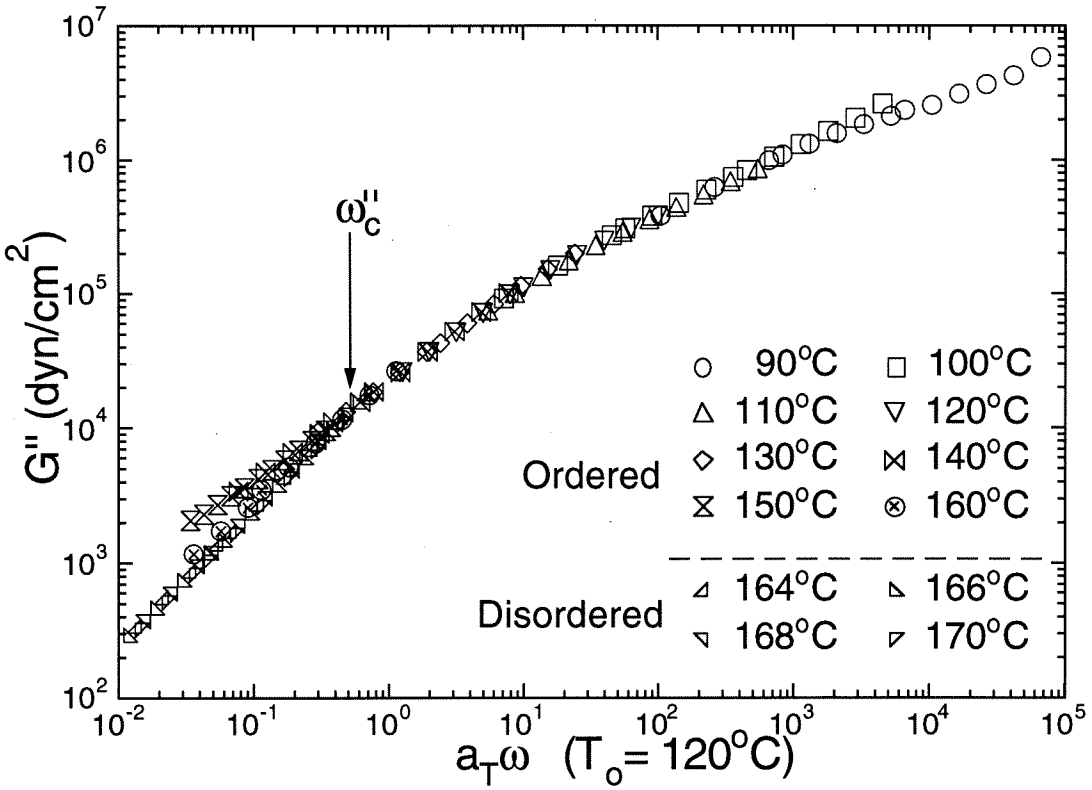

Figure 4.3b: Loss, G'', modulus on a shifted frequency scale ($T_o = 120°C$, a_T given in Table 4.1) for ordered ($T < 164°C$) but macroscopically unaligned state, and the disordered ($T > 164°C$) melt.

and the small strain moduli. In agreement with earlier work [34, 39, 40, 79] we found two distinct regions of parallel and perpendicular alignment. At high shear frequencies relative to the critical frequency ω_c' (*i.e.* $\omega \geq 10$ rad/s at 120°C) parallel alignment was achieved, and at lower frequencies perpendicular alignment was induced (*i.e.* $\omega \leq 1$ rad/s at 120°C).

4.3.2A: Perpendicular Alignment

Shearing at $\omega = 1$ rad/s, $\gamma_o = 1$ produced a rapid rise in $\Delta n_{13}^{(d)}$ followed by a slow saturation to $\sim 8 \times 10^{-4}$ (Figure 4.4a). Further confirmation of the final

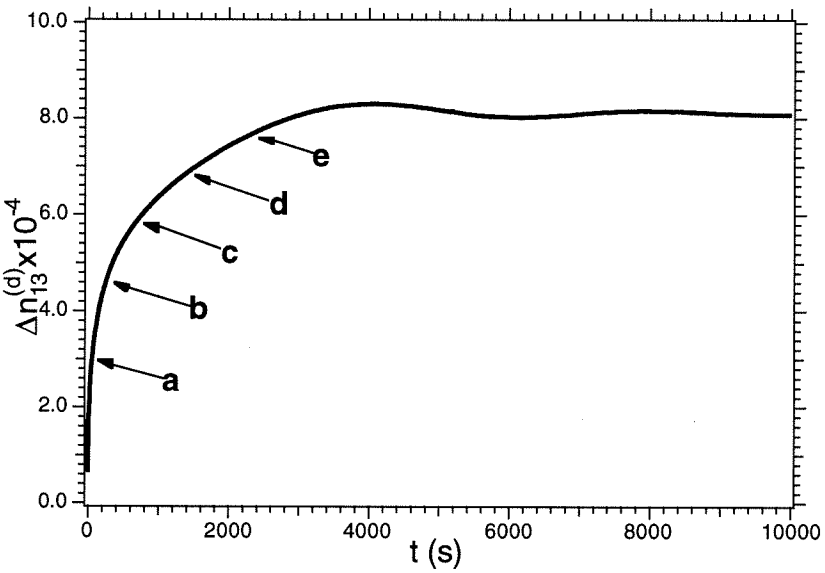

Figure 4.4a: The evolution of the steady offset in 1,3-birefringence during large amplitude shear alignment at $T_o = 120°C$ and $\omega = 1$ rad/s ($\gamma_o = 1.0$) to a perpendicular aligned state. The letters mark approximate locations where in a separate set of experiments, shear alignment was stopped to perform small strain measurements of the dynamic moduli (see Figure 4.5).

magnitude of the birefringence was obtained from the color observed on viewing the sample through crossed polarizers under white light and using the Michél Levy color scheme [93]. While it is difficult to evaluate the order parameter from the birefringence, there are indications that it is quite high. Recent calculations [86, 87] for lamellar styrene-diene block copolymers in the strong segregation limit suggest a value of $\Delta n \approx 16 \times 10^{-4}$ for a perfectly aligned sample. However, the condition examined here is in the weak segregation limit, resulting in smaller (form and intrinsic) birefringence than a strongly segregated PS-PI. It may be noted that in a large suite of experiments described later, the final birefringence of the perpendicular state obtained using different strain amplitudes and reduced frequencies, never exceeded $\Delta n_{13,max} \simeq 10 \times 10^{-4}$.

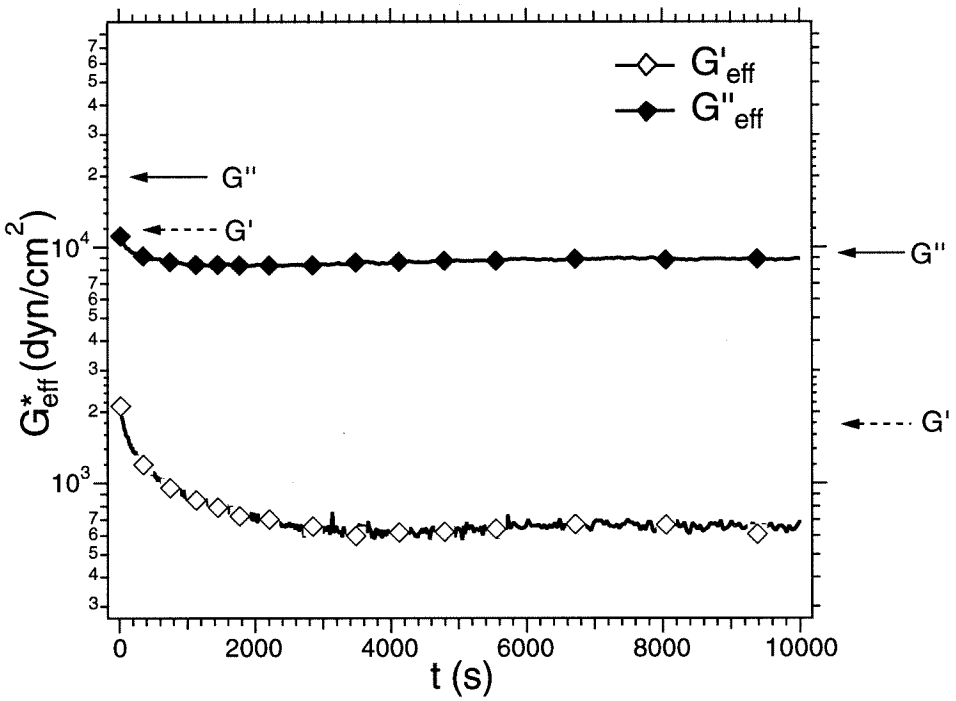

Figure 4.4b: Evolution of effective storage and loss moduli during the large amplitude shear alignment experiments described in Figure 4.4a. Sparsely spaced markers have been used to distinguish the curves. The arrows at left and right indicate the small strain dynamic moduli at ω =1 rad/s, before and after shearing respectively.

The effective dynamic moduli during shear alignment showed an initial rapid fall, followed by a gradual decrease and flattening out (Figure 4.4b). Small strain frequency sweeps before and after shear alignment show a much stronger frequency dependence for both G' and G''in the aligned state (Figure 4.4c). At low frequencies, the dynamic moduli in the aligned material are significantly lower than those in the unaligned material.

To examine the relationship between microstructure and macroscopic mechanical properties, in a separate experiment large amplitude shearing was interrupted to measure the dynamic moduli (linear viscoelastic response) at different points during the course of alignment. During the stoppage of large amplitude shearing the

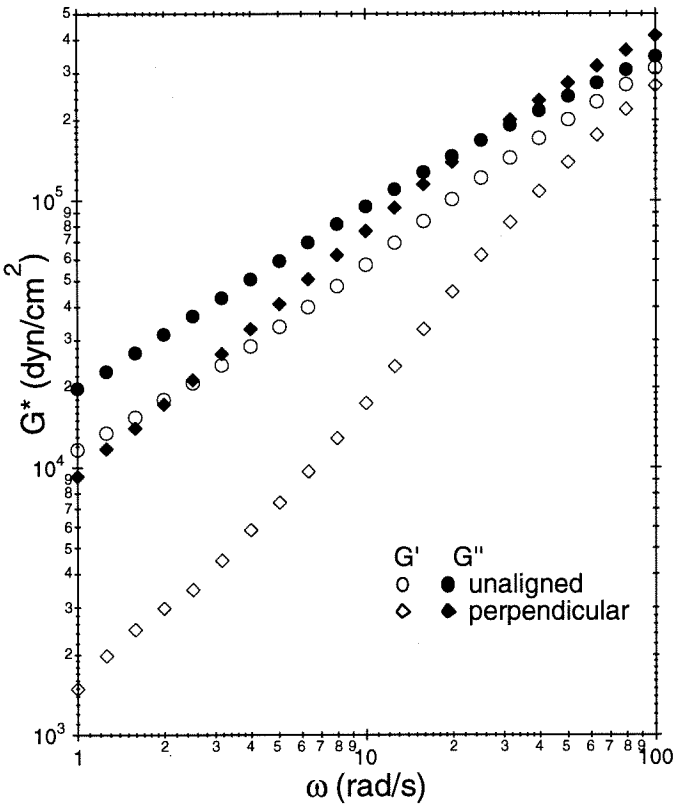

Figure 4.4c: Dynamic moduli at $T_o = 120°C$ obtained using small strain oscillatory shear measurement before and after large amplitude shear as in Figure 4.4a.

birefringence relaxed slightly (< 5%) while each small strain frequency sweep was performed. However, once large amplitude shearing was resumed, the birefringence rapidly reached the value just before the interruption of large amplitude shearing. It then followed a trajectory similar to that observed when shearing was continuous. The magnitude of the recovery in $\Delta n_{13}^{(d)}$ during the pause for small-strain experiments decreased with shearing time, being the largest when shearing was stopped at the end of the fast process (point 'a' on Figure 4.4a).

For perpendicular alignment, G' shows a monotonic decrease as alignment progresses (Figure 4.5a). To facilitate comparison, G' and G'' are shown normalized

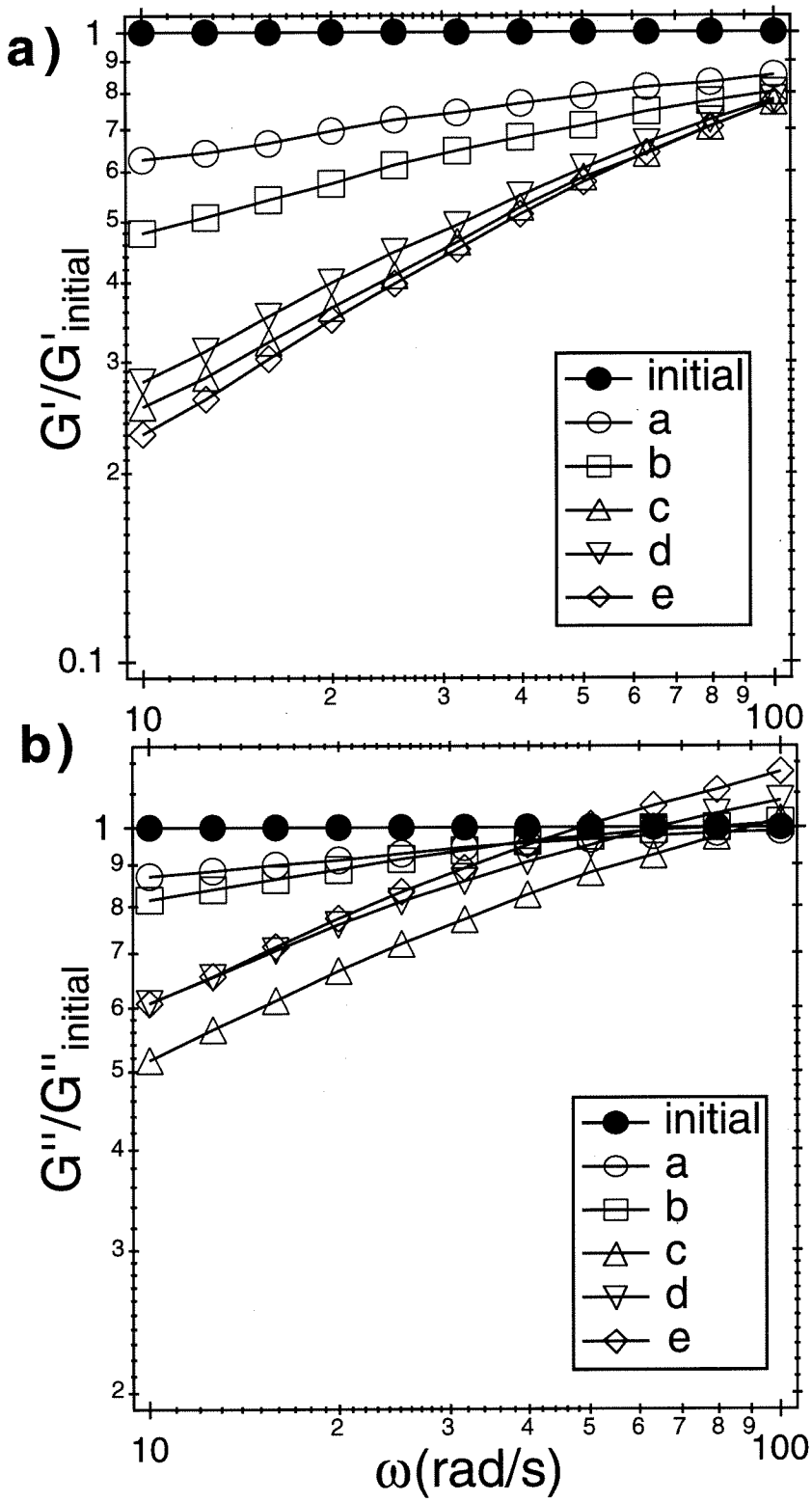

Figure 4.5: Small strain measurements of (a) storage and (b) loss moduli at various intermediate points during shear alignment at 1 rad/s. At each frequency, G' and G'' are normalized by the respective modulus before shear alignment.

by the corresponding values before shear alignment. Almost all of the change in the frequency dependence of G' occurs as $\Delta n_{13}^{(d)}$ increases to $\sim 6 \times 10^{-4}$ (point 'c' in Figure 4.4a). The loss modulus shows a different, non-monotonic behavior (Figure 4.5b): it decreases only slightly from the initial unaligned state as $\Delta n_{13}^{(d)}$ increases to $\sim 4.5 \times 10^{-4}$ (point 'b' in Figure 4.4a). However, with further increase of the retardation to $\Delta n_{13}^{(d)} \simeq 6 \times 10^{-4}$ (point 'c'), there is a large drop in G'' to nearly 50% of the initial value at low frequencies. Beyond this as the birefringence increases, G'' increases by about 10-15% equally at all frequencies.

4.3.2B: Parallel Alignment

Shearing at 100 rad/s ($\gamma_o = 0.5$) and at 10 rad/s ($\gamma_o = 0.8$) produces parallel alignment of the lamellae. Surprisingly, while the final states in both the shear alignment experiments exhibit $\Delta n_{13}^{(d)} \simeq 0$, the evolution of birefringence during alignment is dramatically different (Figure 4.6a). At $\omega = 100$ rad/s, $\Delta n_{13}^{(d)}$ rapidly becomes large and negative, in stark contrast to the steep positive rise in $\Delta n_{13}^{(d)}$ for $\omega = 10$ rad/s. A positive $\Delta n_{13}^{(d)}$ implies enhanced lamellar orientations biased towards perpendicular alignment relative to those biased along the transverse direction. Conversely, a negative $\Delta n_{13}^{(d)}$ implies a diminished ratio of the projection of perpendicular orientation to transverse orientation—quite contrary to expectations.

For both sets of flow conditions, the maximum absolute value of birefringence is $\Delta n_{13}^{(d)} \mid \approx \frac{1}{3}\Delta n_{13,max}$ ($\sim 3 \times 10^{-4}$), and is reached within ~ 100 seconds. Both these initial fast processes are followed by a much slower ($t \sim 3000 - 4000s$) decrease of birefringence to a near zero value. This peak value of $\Delta n_{13}^{(d)} \sim 3 \times 10^{-4}$, for the

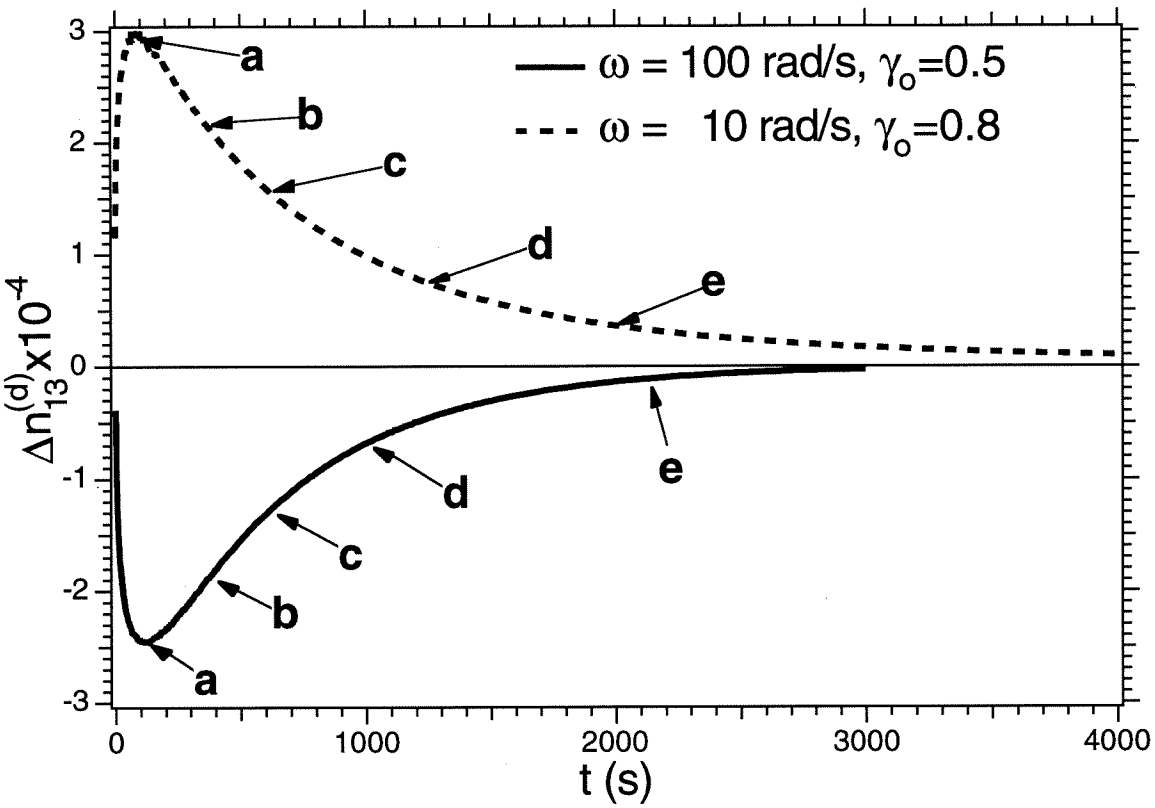

Figure 4.6a: Evolution of the steady offset in 1,3-birefringence during large amplitude shear alignment at at $T_o = 120°C$, $\omega = 10$ rad/s ($\gamma_o = 0.8$) and 100 rad/s ($\gamma_o = 0.5$) to a parallel aligned state. The letters mark approximate locations where in a separate set of experiments, shear alignment was stopped to perform small strain measurements of the dynamic moduli (see Figures 4.7 and 4.8).

case of red HeNe radiation ($\lambda = 633nm$) and the geometry employed ($d = 0.52mm$) corresponds to a retardation $\mu \approx \pi/2$. Since we measure $\sin\mu$, an increase in μ beyond $\pi/2$ to a value of π is indistinguishable from a decrease of μ from $\pi/2$ to 0. Therefore, shearing experiments were repeated using green HeNe radiation ($\lambda = 543nm$) to verify the magnitude of the birefringence. These experiments confirm that the birefringence indeed reaches a maximum magnitude of $\approx 3 \times 10^{-4}$ and then decreases to nearly zero.

The effective dynamic moduli during shear show a large initial drop followed by

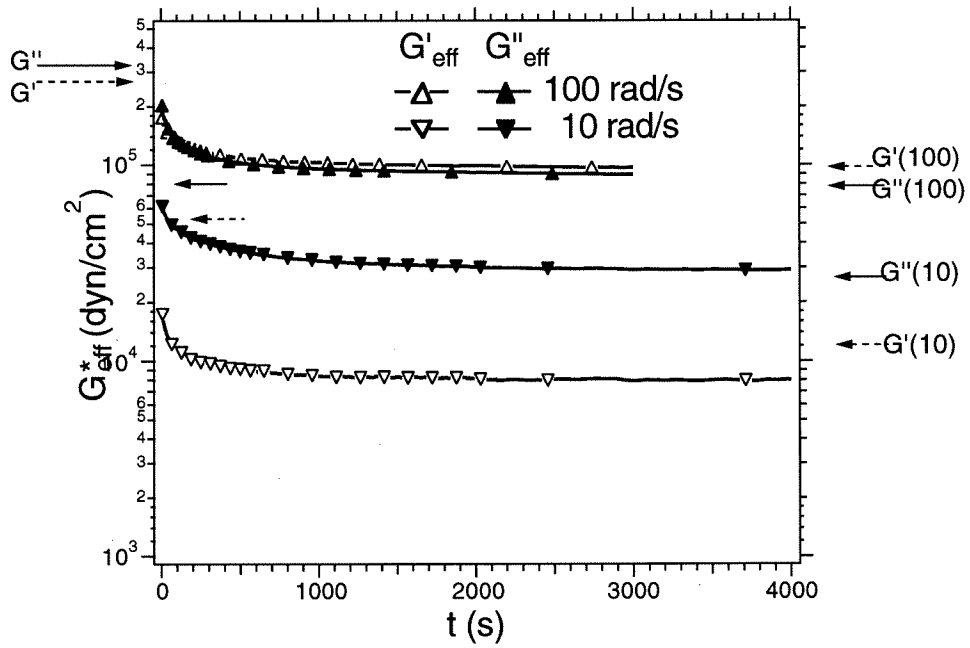

Figure 4.6b: Evolution of effective storage and loss moduli during the large amplitude shear alignment experiments described in Figure 4.6a. Sparsely spaced markers have been used to distinguish the curves. The arrows at left and right indicate the small strain dynamic moduli at 10 or 100 rad/s, as indicated, before and after shearing respectively.

a gradual flattening out (Figure 4.6b). This drop is slightly larger than that during perpendicular alignment at 1 rad/s. The small strain dynamic moduli for the two aligned samples are also nearly identical to each other and dramatically lower than those of the unaligned ordered sample (Figure 4.6c) as well as the perpendicular aligned sample (c.f. Figure 4.4c). A similar decrease in dynamic moduli has been reported for parallel alignment in PS-PI [34, 39, 40]. These dynamic moduli measurements together with the small value of 1,3-birefringence at the end of shearing, allow us to infer that the final alignment is along the parallel direction.

As before, to study the link between the microstructure and the macroscopic mechanical behavior, we performed a separate set of experiments in which we interrupted

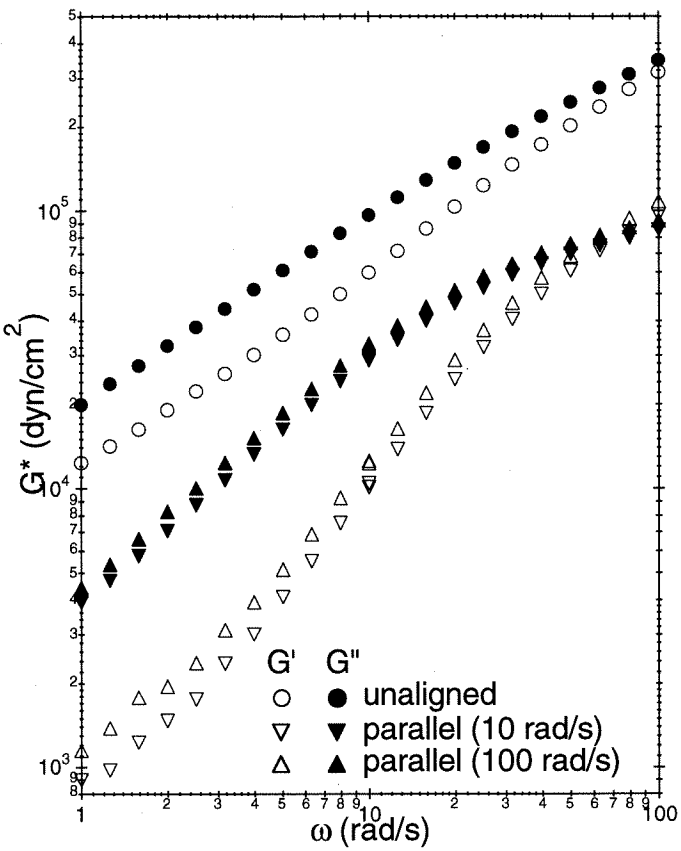

Figure 4.6c: Dynamic moduli at $T_o = 120°C$ obtained using small strain oscillatory shear measurement before and after large amplitude shear as in Figure 4.6a.

the alignment process at several stages and measured the dynamic moduli using small strains (Figures 4.7 and 4.8). As was the case for perpendicular alignment, there is a monotonic drop in G' and G'' associated with the changes that occur during the first few hundred seconds of large amplitude shearing at either 100 rad/s or 10 rad/s (up to point 'c' in Figure 4.6a). The dynamic moduli hardly change from point 'c' to point 'd', then drop again on proceeding to point 'e'. Given the very different orientation distributions indicated by the birefringence at these points for the 10 and 100 rad/s cases, the dynamic moduli at corresponding points in the processes are surprisingly similar.

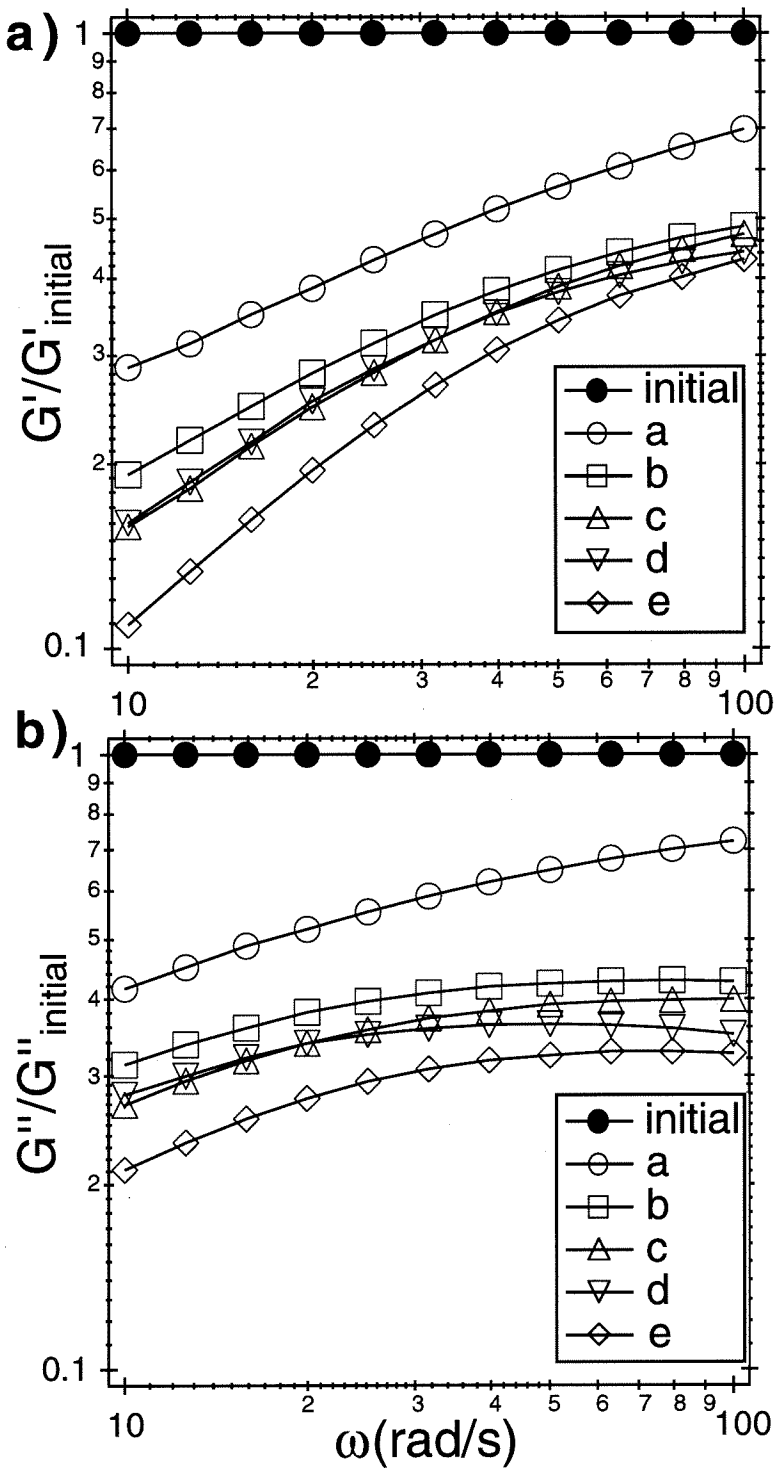

Figure 4.7: Small strain measurements of (a) storage and (b) loss moduli at various intermediate points during shear alignment at 10 rad/s. At each frequency, G' and G'' are normalized by the respective modulus before shear alignment.

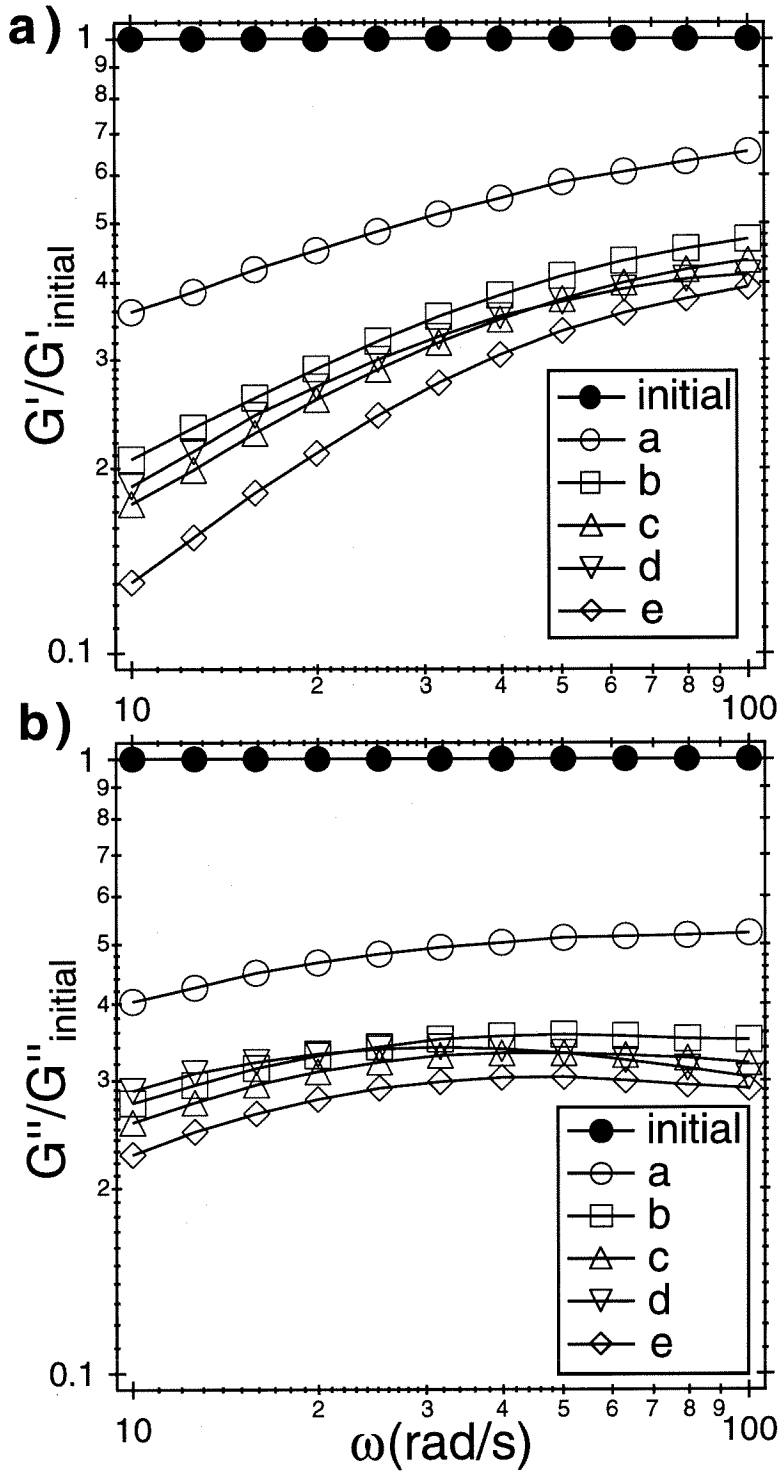

Figure 4.8: Small strain measurements of (a) storage and (b) loss moduli at various intermediate points during shear alignment at 100 rad/s. At each frequency, G' and G'' are normalized by the respective modulus before shear alignment.

4.3.2C: Frequency and Trajectory of Alignment

The flow alignment experiments carried out at 100, 10 and 1 rad/s clearly suggest that distinct processes dominate at each of the three frequencies leading to different trajectories of the birefringence and different final aligned states. In this section we focus on two issues: effect of ω on the development of similar final aligned states through dramatically different evolution pathways, *i.e.* 10 rad/s $\leq \omega \leq$ 100 rad/s; and the effect of ω on the orientation direction induced by shearing, *i.e.* 1 rad/s $\leq \omega \leq$ 10 rad/s.

- *Effect of Frequency on the Development of Parallel Alignment*

  As the shear frequency is decreased from 100 rad/s to 10 rad/s, the evolution of the birefringence shows a monotonic progression from having a negative extremum to a positive maximum (Figure 4.9). A strain amplitude[9] of $\gamma_o = 0.5$ was used for frequencies ranging from 60 to 20 rad/s. For some of the cases examined (*e.g.* ω =30 rad/s, $\gamma_o = 0.5$), the displacement of the birefringence remains near zero throughout the process. Yet in every case, the effective moduli G'_{eff} and G''_{eff} during the alignment process showed the characteristic large drop initially and a final flattening out. Large amplitude shearing was continued until both G^*_{eff} and $\Delta n_{13}^{(d)}$ had reached constant values. For all ω from 10 to 100 rad/s, the ultimate value of $\Delta n_{13}^{(d)}$ was approximately zero and the dynamic

[9]At higher frequencies the commanded strain γ_{com} was different than the applied strain γ_a, which varied over the course of prolonged shear. In the figures and text the strain amplitude indicated is the commanded strain. During shear alignment at 100 rad/s, $\gamma_{com} = 0.5$, and the initial strain amplitude was 0.38 and the final 0.44. Corresponding values for other shear frequencies are: 60 rad/s ($\gamma_{com} = 0.5, \gamma_a \simeq 0.44 - 0.46$), 30 rad/s ($\gamma_{com} = 0.5, \gamma_a \simeq 0.48$), and 20 rad/s ($\gamma_{com} = 0.5, \gamma_a \simeq 0.47 - 0.485$). Below 20 rad/s, the agreement between the commanded and the applied strain is within 1%.

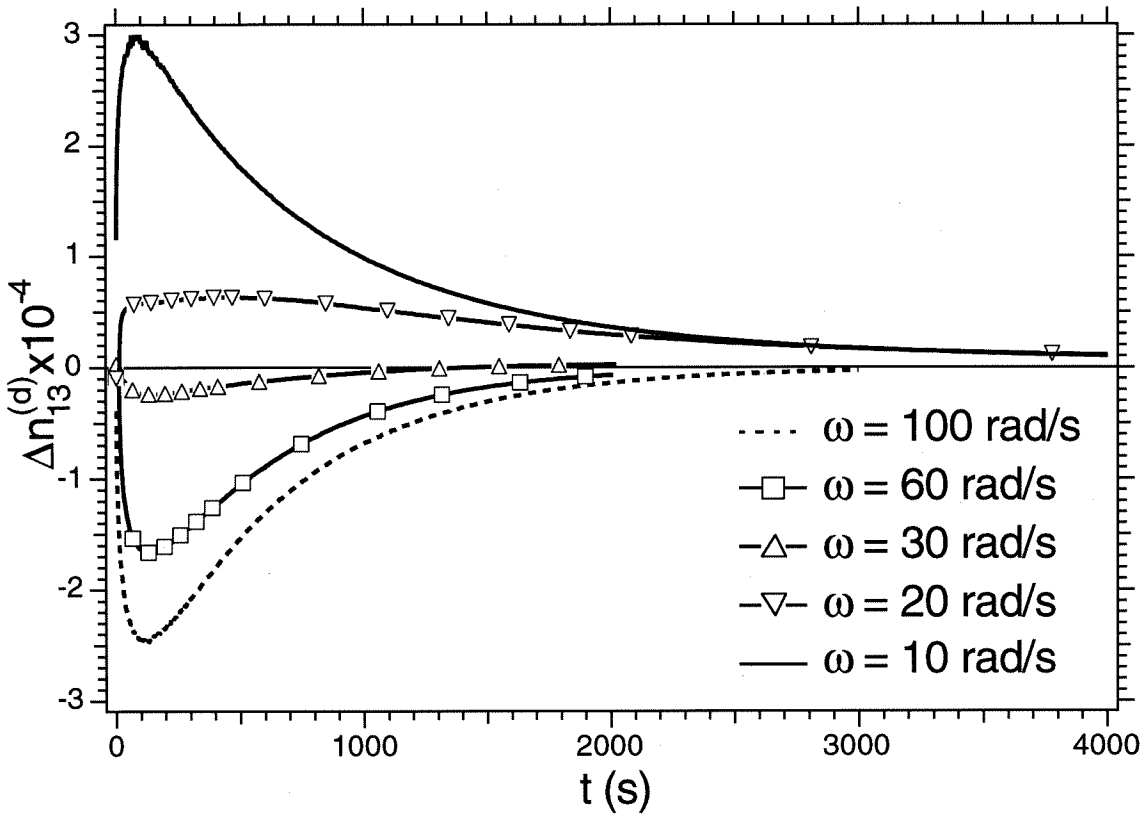

Figure 4.9: Evolution of the steady offset in 1,3-birefringence during large amplitude shear alignment at $T_o = 120°C$ for frequencies 100-10 rad/s to a parallel aligned state. Strain amplitude $\gamma_o = 0.8$ was used at 10 rad/s, and $\gamma_o = 0.5$ for 100-20 rad/s.

moduli after shearing were the same and roughly an order of magnitude lower than that in the initial unaligned condition. Both $\Delta n_{13}^{(d)} \approx 0$ and low $G^*(\omega)$ of the final state suggest that parallel alignment was induced in all cases.

- *Effect of Frequency on the Direction of Alignment*

  To examine alignment behavior at a frequency lying between the parallel (i.e., $\omega \geq 10$ rad/s) and perpendicular (i.e., $\omega \leq 1$ rad/s) regimes, we performed shear alignment at 4 rad/s. Oscillatory shear at $\gamma_o = 0.4$ resulted in build-up of a large positive birefringence (Figure 4.10a), typical of perpendicular alignment (Figure 4.4a). During flow, G^*_{eff} showed a modest initial decrease

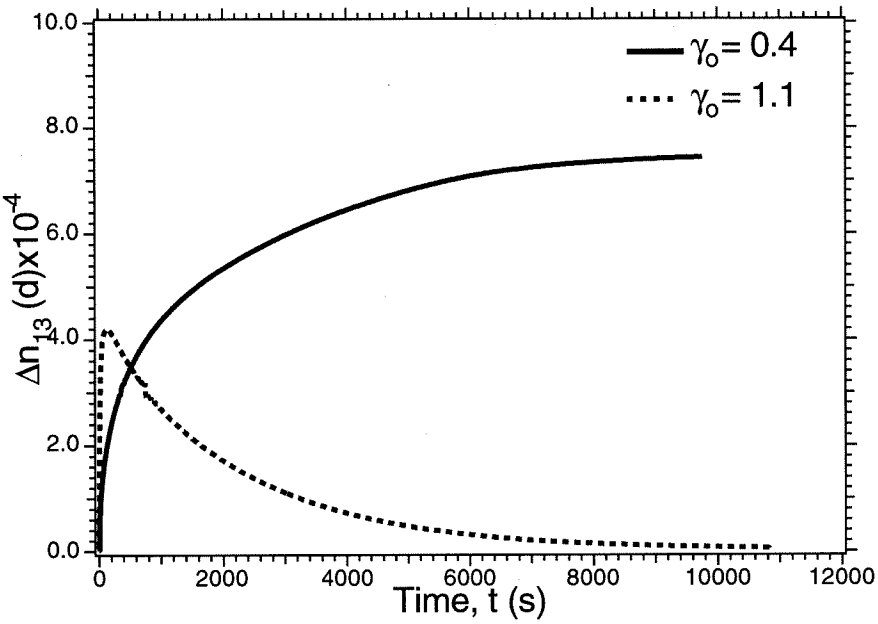

Figure 4.10a: The evolution of the steady offset in 1,3-birefringence during large amplitude shear alignment at $T_o = 120°C$ and $\omega = 4$ rad/s using two different strain amplitudes: $\gamma_o = 0.4$ leading to a perpendicular aligned state, and $\gamma_o = 1.1$ leading to a parallel aligned state.

and then became relatively constant (Figure 4.10b, *c.f.* Figure 4.4b). The dynamic moduli of the final aligned state (Figure 4.10c), were identical to those of a perpendicular aligned sample (Figure 4.4c).

In contrast, shearing at the same frequency and temperature, but using $\gamma_o = 1.1$ induced parallel alignment as indicated by a near zero final $\Delta n_{13}^{(d)}$ (Figure 4.10a) and small strain moduli after alignment (Figure 4.10c) consistent with those of parallel aligned material (Figures 4.6c). The time trace of $\Delta n_{13}^{(d)}$ was similar to the behavior at 10 rad/s, but reaching a significantly higher maximum value of $\Delta n_{13}^{(d)} \approx 4.2 \times 10^{-4}$ before decaying to zero. The effective dynamic moduli recorded during flow alignment showed significant differences from that observed at $\gamma_o = 0.4$ (Figure 4.10b): the decreases of both G'_{eff} and G''_{eff} were larger

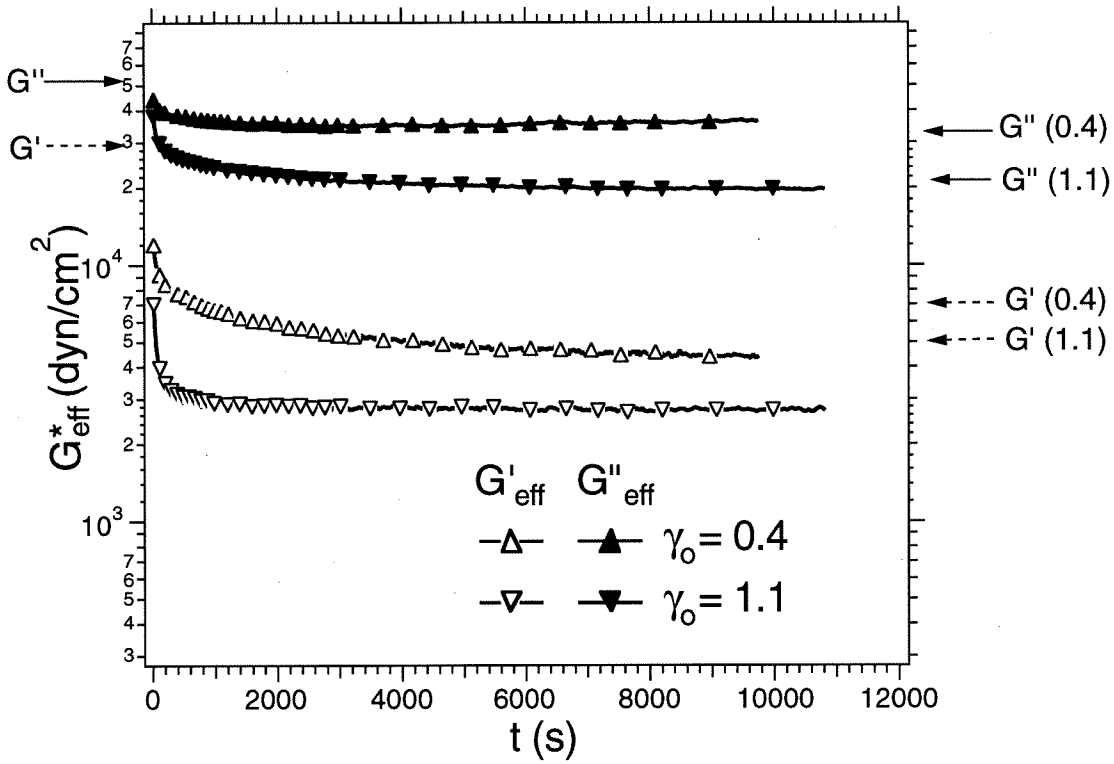

Figure 4.10b: Evolution of effective storage and loss moduli during the large amplitude shear alignment experiments described in Figure 4.10a. Sparsely spaced markers have been used to distinguish the curves. The arrows at left and right indicate the small strain dynamic moduli at ω =4 rad/s, before and after shearing respectively.

than the modest decreases observed during alignment at $\gamma_o = 0.4$. Instead the behavior was similar to that observed during parallel alignment at 10 rad/s (Figure 4.6b).

4.3.3 Effect of Strain Amplitude (γ_o) on Evolution of Alignment

Results presented in the previous section indicate a complex interplay of temperature, shearing frequency and strain amplitude in controlling the changes in the orientation distribution during shearing. In this section we focus on the effects of strain amplitude

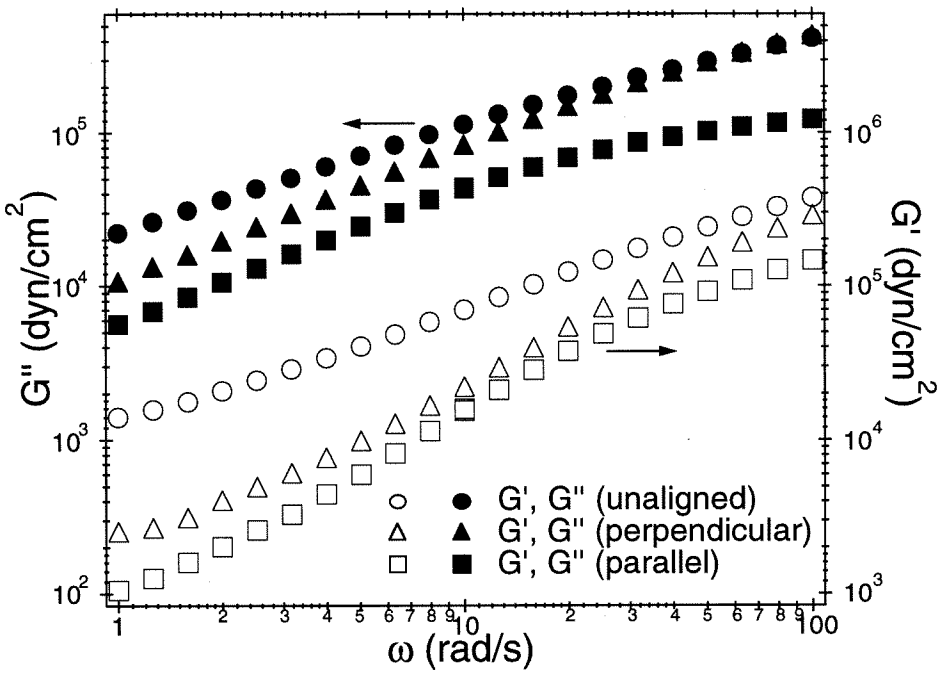

Figure 4.10c: Dynamic moduli at $T_o = 120°C$ obtained using small strain oscillatory shear measurement before and after large amplitude shear as in Figure 4.10a.

upon flow alignment. We discuss results obtained during shearing at different strain amplitudes at 120°C for both perpendicular and parallel alignment.

4.3.3A: Perpendicular Alignment

To investigate the effect of strain on the perpendicular alignment process, shearing experiments were performed at $\omega = 1$ rad/s and $T = 120°C$ with strain amplitudes from 0.3 to 1 (Figure 4.11a). Based on the transient birefringence observed at $\gamma_o = 0.3$, lower strain amplitudes were not attempted, since the alignment process became prohibitively slow.

The transient birefringence during shear possessed similar shape at the different strain amplitudes, indicating similar trajectories for the evolution of the orientation distribution. However, the time-scale of the alignment process was significantly re-

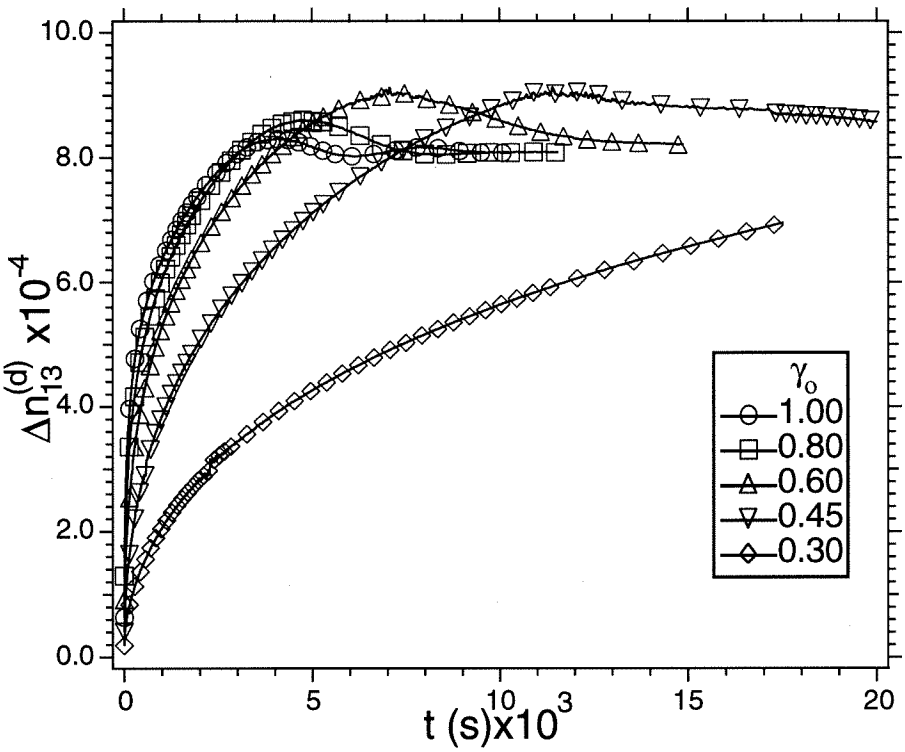

Figure 4.11a: Transient 1,3-birefringence observed during shearing at $T = 120°C$, $\omega = 1$ rad/s and different strain amplitudes. Sparsely spaced markers have been used.

duced with increasing strain amplitude. Shearing at $\gamma_o \geq 0.45$ ultimately resulted in a high value of $\Delta n_{13}^{(d)}$ ($\simeq 8.2 \times 10^{-4}$) indicating a high degree of perpendicular alignment. In contrast, shearing at $\gamma_o = 0.3$ yields intermediate alignment with the birefringence reaching only $\sim 7 \times 10^{-4}$ within 17000s.

By inspection of the shape of $\Delta n_{13}^{(d)}(t)$, it is clear that it is not possible to superpose the complete transient birefringence at different strain amplitudes by simple rescaling of time as $t/\tau(\gamma_o)$. Due to the absence of any predictions for the form of $\tau(\gamma_o)$, we attempted to collapse the curves using $\tau(\gamma_o) \sim \gamma_o^n$, restricting n to integers. This allows us to qualitatively describe the nonlinear effect of γ_o, and to contrast its effect on fast *vs* slow processes. With this scaling, the transient birefringence up

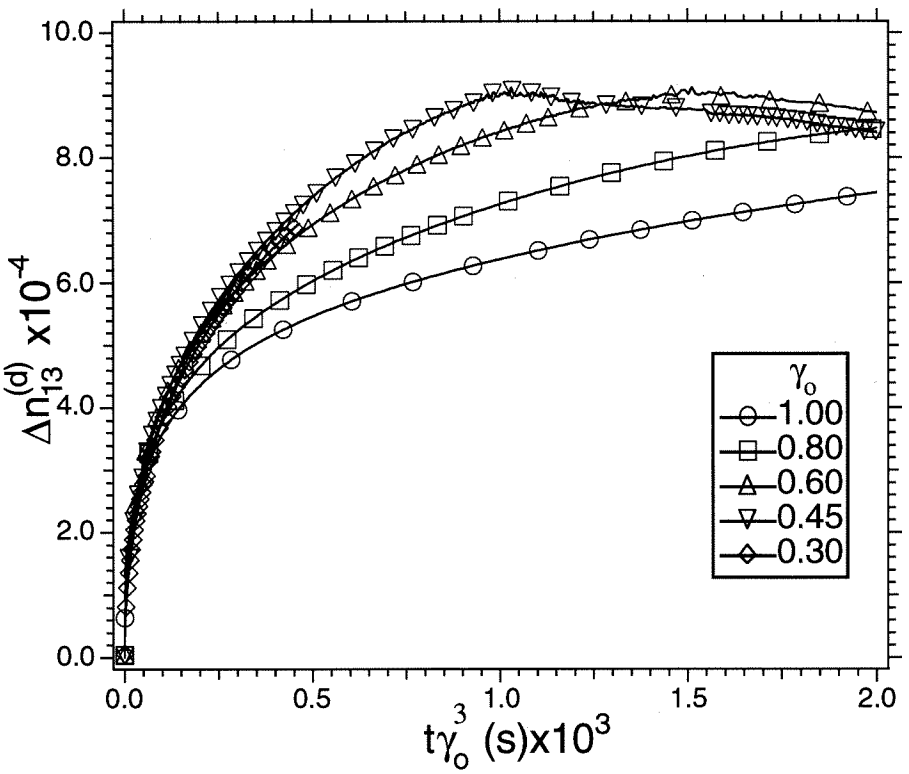

Figure 4.11b: Evolution of $\Delta n_{13}^{(d)}(t)$ plotted against scaled time. Shearing is at 1 rad/s and $T = 120°C$ with strain amplitude varied from 0.3 to 1. Sparsely spaced markers have been used.

to $\approx 3 \times 10^{-4}$ is superposed when plotted against $\gamma_o^3 t$ (Figure 4.11b). This scaling indicates a stronger effect of γ_o than can be attributed to either cumulative strain ($\gamma_o t$) or work ($\gamma_o^2 t$) during shearing at a fixed frequency ω. The latter part of the transient birefringence is not superposed by this scaling: the effect of strain during this period of the evolution of alignment being somewhat weaker than during the initial rise. In turn, this may signal a change in the mechanism of alignment from the "fast" process to the "slow" one.

At all strain amplitudes the effective dynamic modulus (G^*_{eff}) during shear alignment showed an initial rapid fall, and subsequent gradual decrease (Figure 4.11c). We examine the relation between the orientation distribution and the modulus, by plot-

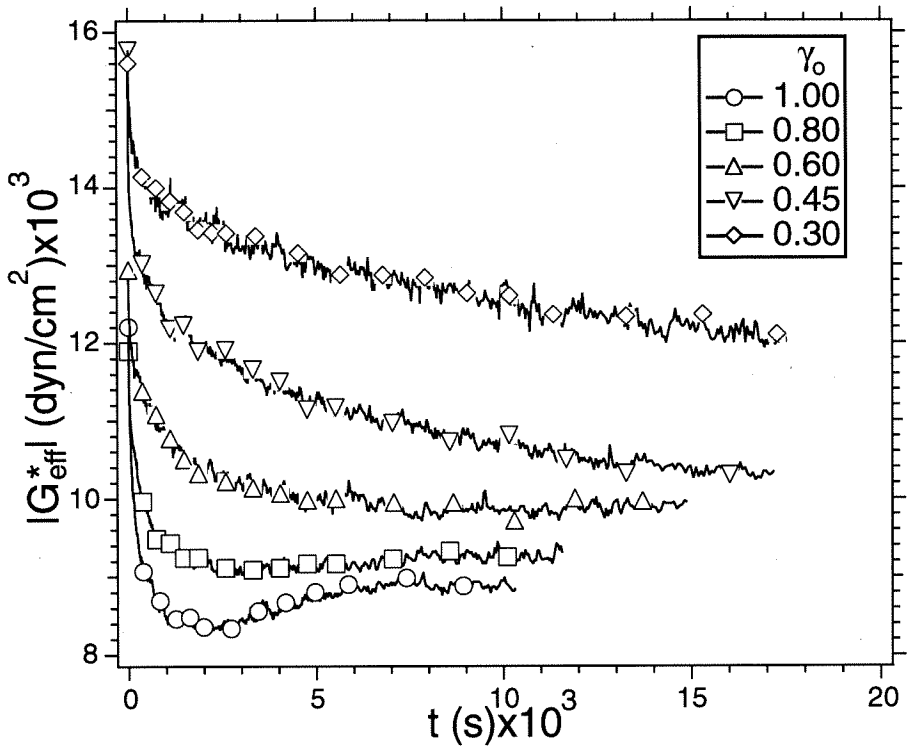

Figure 4.11c: Magnitude of the effective modulus $\mid G^*_{eff} \mid$ plotted against time for shearing at 1 rad/s and $T = 120°C$ with strain amplitude varied from 0.3 to 1. Sparsely spaced markers have been used.

ting $\Delta n^{(d)}_{13}(t)$ against $\mid G^*_{eff}(t) \mid$ at different strain amplitudes (Figure 4.11d). The evolution of $\mid G^*_{eff}(t) \mid$ as a function of microstructure (to the extent it is indicated by $\Delta n^{(d)}_{13}(t)$) changes with strain. A large strain softening effect is observed as $\mid G^*_{eff}(t) \mid$ shifts strongly towards lower modulus with increasing γ_o.

4.3.3B: Parallel Alignment

We have previously shown that prolonged shearing at $\omega = 10$ to 100 rad/s at 120°C led to parallel alignment, though via different trajectories (Section 4.3.2B). During alignment at 10 rad/s, the initial process was dominated by a rapid depletion of the projection of the orientation distribution along the transverse direction ($\hat{\mathbf{u}} \parallel axis\ 1$) relative to the perpendicular direction ($\hat{\mathbf{u}} \parallel axis\ 3$), manifested as a rapid increase in

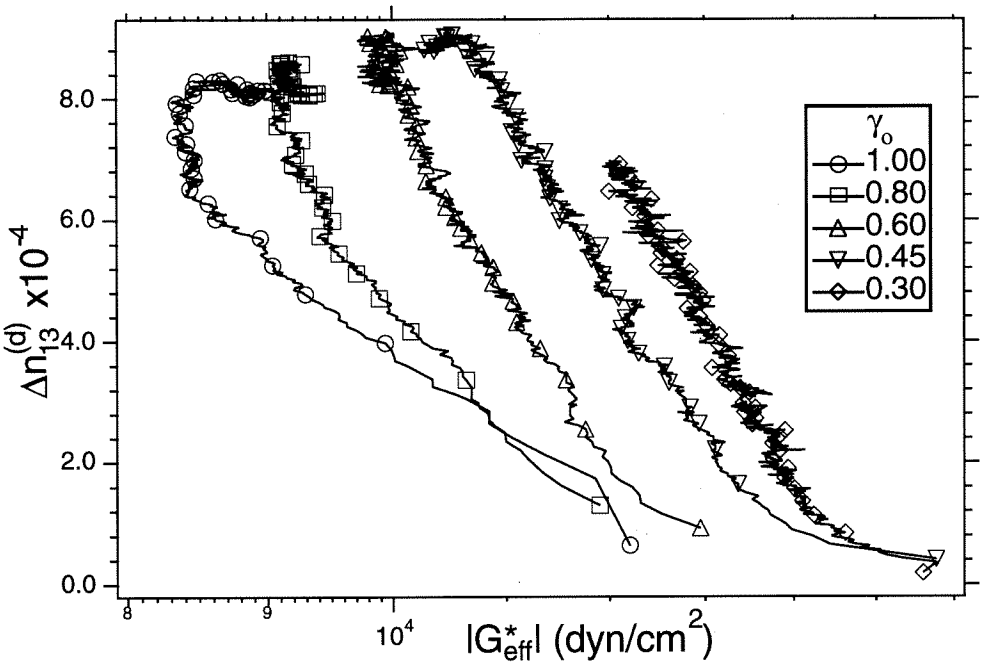

Figure 4.11d: Transient birefringence plotted against the effective modulus ($\mid G^*_{eff}(t) \mid$) measured during alignment. Sparsely spaced markers have been used.

$\Delta n_{13}^{(d)}(t)$. Conversely at 100 rad/s, during the initial fast process, the projection of the orientation distribution along the perpendicular direction decreased faster than that along the transverse direction, indicated by the sharp decrease of birefringence towards a large negative value. At intermediate frequencies, both projections decreased at comparable rates, with the birefringence remaining small throughout the alignment process.

To understand the role of strain during parallel alignment, we performed experiments over a range of strain amplitudes at three frequencies: 10, 30 and 100 rad/s at 120°C.

ω =10 rad/s at 120°C: Shearing with strain amplitudes from $\gamma_o = 0.5$ to $\gamma_o = 1.0$ resulted in qualitatively similar transient birefringence during shear (Figure 4.12a)

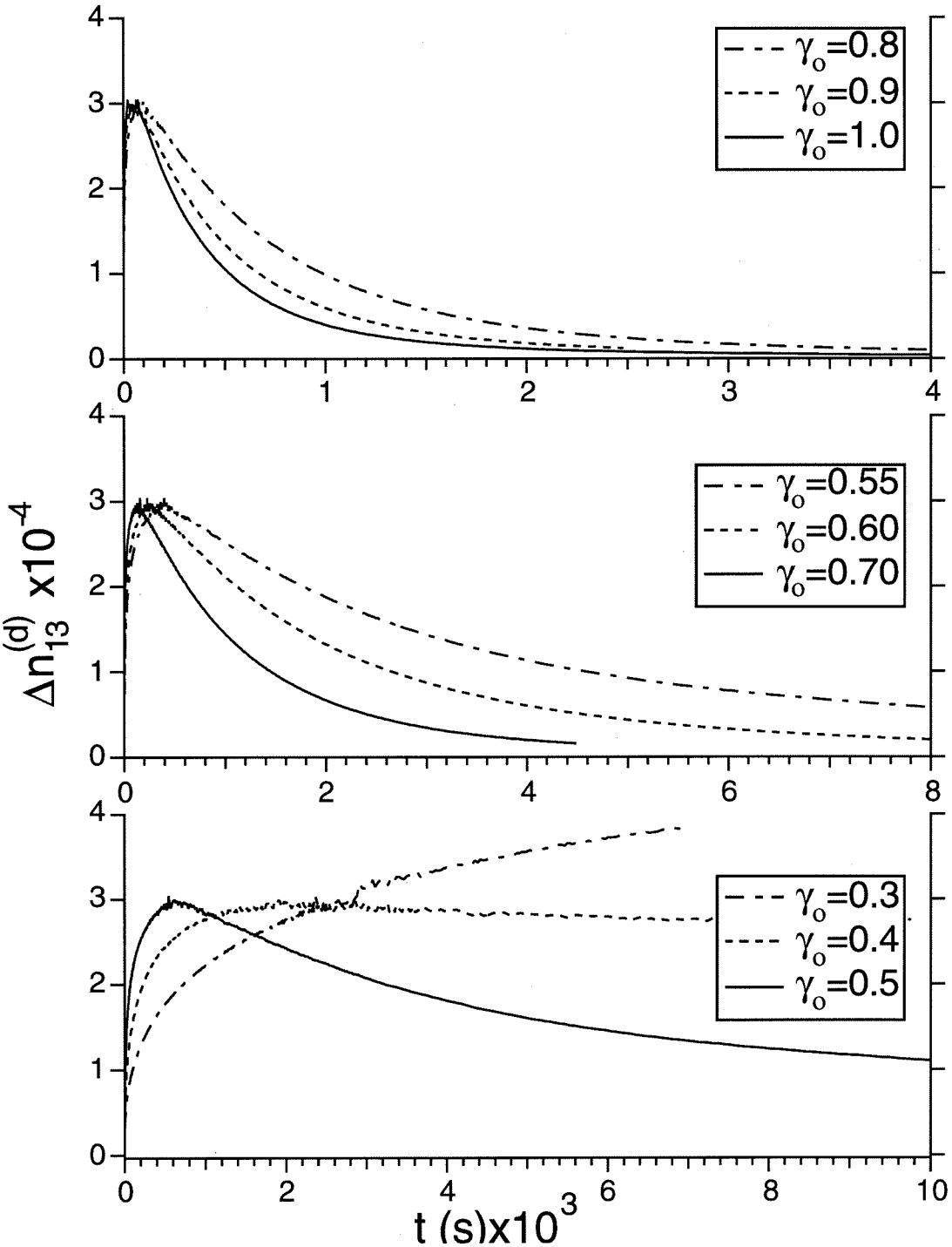

Figure 4.12a: Transient 1,3-birefringence observed during shearing at $T = 120°C$, $\omega = 10$ rad/s and different strain amplitudes.

and final aligned states with almost identical small-strain dynamic moduli. During the initial fast process, $\Delta n_{13}^{(d)}(t)$ increased rapidly to a value $\sim 3 \times 10^{-4}$ for each strain ≥ 0.5. Refinement of alignment during the slow process was accompanied by a gradual decrease in the birefringence to a near zero value.

Shearing at strain amplitudes below 0.5, produced qualitatively different results (Figure 4.12a). The transient birefringence during the fast process at $\gamma_o = 0.4$ increased to $\sim 3 \times 10^{-4}$, like at higher strain amplitudes; however, no slow refinement of the alignment was evident and $\Delta n_{13}^{(d)}(t)$ remained at this approximate value for over 9000s. Thus, unlike other strain amplitudes, for $\gamma_o = 0.4$, the final state was not highly aligned.[10] The birefringence during shearing at $\gamma_o = 0.3$, was even more unexpected. Here, $\Delta n_{13}^{(d)}(t)$ increased throughout the duration of shearing and exceeded $\sim \frac{1}{3}\Delta n_{max}$ ($\sim 3 \times 10^{-4}$) (Figure 4.12a). This effect of strain amplitude was qualitatively similar to our earlier observations during shearing at 4 rad/s and $T = 120°C$, where a relatively low strain amplitude ($\gamma_o \simeq 0.4$) produced perpendicular alignment, while at the same frequency a higher strain amplitude ($\gamma_o \simeq 1.1$) induced parallel alignment (Figure 4.10a). The small strain moduli after shearing at $\omega = 10$ rad/s and $\gamma_o = 0.3$ and 0.4 were between those of the initial unaligned state and those observed after alignment at higher strain amplitudes.

Successive shearing at $\gamma_0 = 0.8$ was performed after cessation of prolonged ($\sim$ 7000s) shearing at $\gamma_o = 0.3$ (Figure 4.12b). This resulted in a sharp decrease

[10]Quantitative characterization of the degree of alignment is an important issue. It has been reported that strain amplitudes as low as 0.05 yield parallel alignment [34]. However, our transient birefringence results from shearing at 120°C with strain amplitudes of 0.3 ($\omega = 10$ rad/s) and 0.2 ($\omega = 100$ rad/s) show that while the lamellar distribution has an enhanced projection along the parallel direction, the degree of alignment is *not* high (Figures 4.12a and 4.14a).

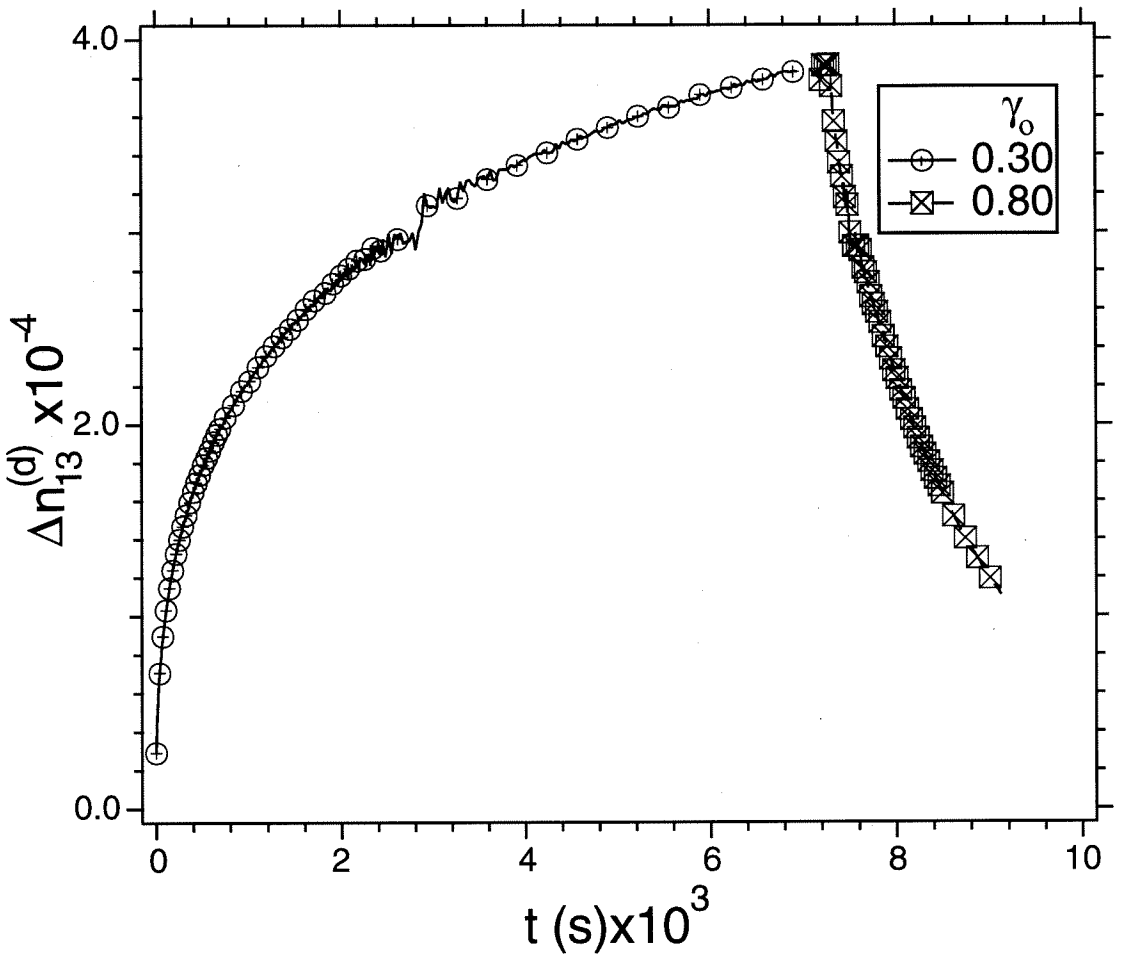

Figure 4.12b: Evolution trajectory for $\Delta n_{13}^{(d)}(t)$ during shearing (T = 120°C, ω = 10 rad/s), first with a strain amplitude of 0.3 followed by a strain amplitude of 0.8. Sparsely spaced markers have been used.

of $\Delta n_{13}^{(d)}(t)$ towards zero, in a manner reminiscent of the "flipping" of perpendicular alignment to parallel observed by Kornfield *et al.* [79]. The small-strain dynamic moduli measured at the end of this shearing process were identical to those obtained for a well-aligned parallel state. The time scale for approaching parallel alignment was similar to that observed when shearing at $\gamma_o = 0.8$ starting from an unaligned initial state.

The rate of both the fast and slow processes increased with increase in strain

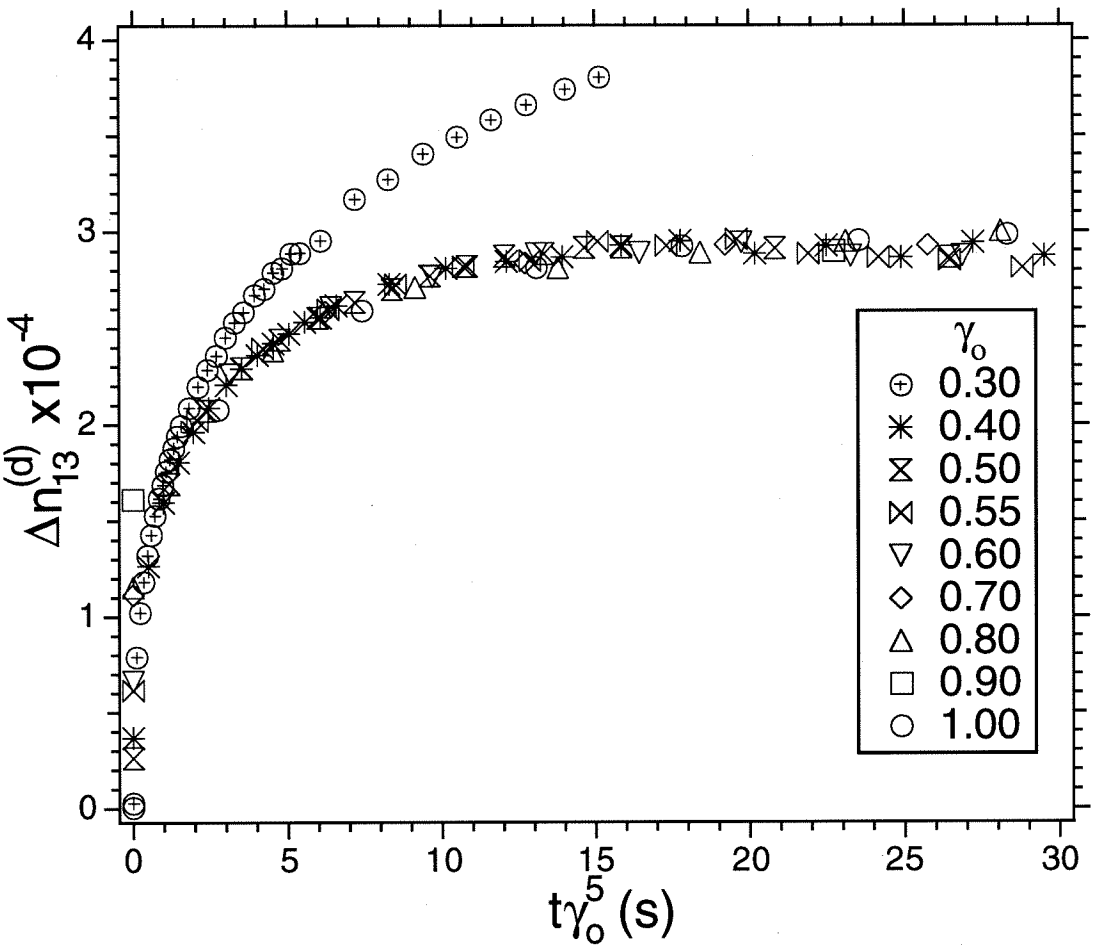

Figure 4.12c: Evolution of $\Delta n_{13}^{(d)}(t)$ during the initial fast process plotted against scaled time. Sparsely spaced markers have been used.

(Figure 4.12a). Once again, simple rescaling of time did not yield a single master curve for all the different strain amplitude experiments. However, the initial rise in $\Delta n_{13}^{(d)}(t)$ could be nearly superposed for $\gamma_o \geq 0.4$ using a scaled time $\gamma_o^5 t$ (Figure 4.12c). In contrast to the cubic scaling (*i.e.* $\gamma_o^3 t$) obtained in the perpendicular alignment case, here the effects of strain amplitude were even more highly non-linear. Again, such a strongly non-linear effect of strain amplitude cannot be attributed simply to either cumulative strain ($\gamma_o t$) or work ($\gamma_o^2 t$) done during shearing. The failure to superpose the transient birefringence observed upon shearing at $\gamma_o = 0.3$, suggested that the

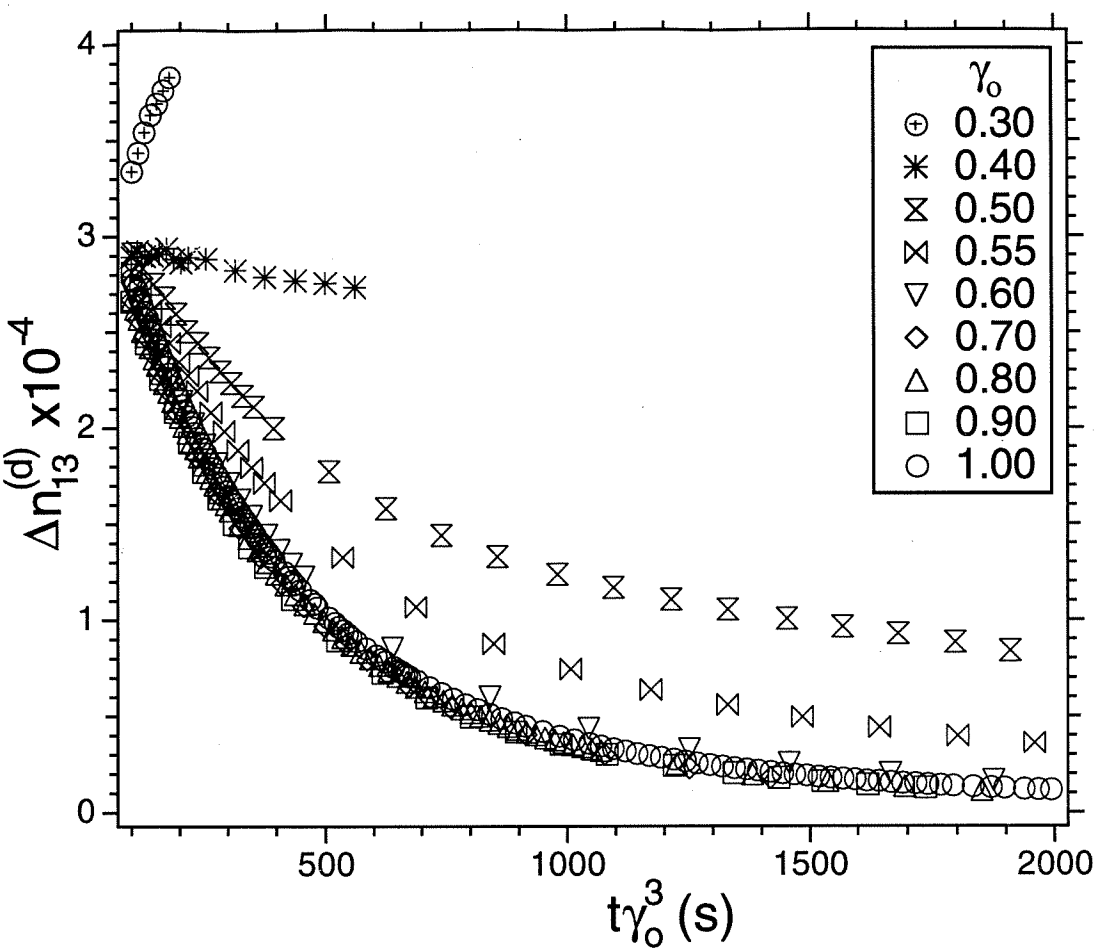

Figure 4.12d: Evolution of $\Delta n_{13}^{(d)}(t)$ during the slow process plotted against scaled time. Sparsely spaced markers have been used.

nature of alignment mechanism changed as γ_o decreased.

The slow refinement of alignment could be partially superposed by rescaling time, using $\gamma_o^3 t$ for $\gamma_o > 0.55$ (Figure 4.12d). Below this strain amplitude there were systematic deviations from this scaling, indicating stronger-than-cubic dependence on γ_o for $\gamma_o \leq 0.55$. Thus, while strain amplitude affects both the fast and slow processes strongly, the effects of strain on the rate of each process are distinct, and suggest distinct underlying processes.

In contrast to results at $\omega = 1$ rad/s, the transient birefringence during shearing at

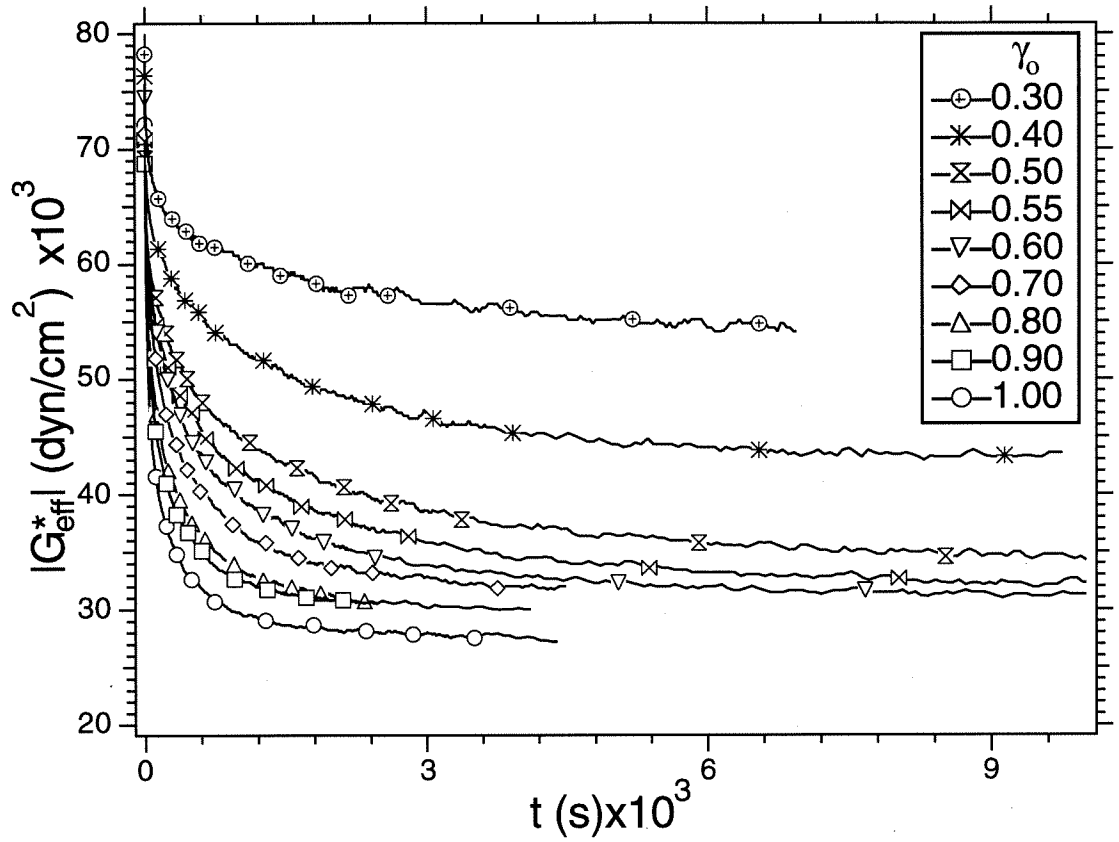

Figure 4.12e: Magnitude of the effective modulus $\mid G^*_{eff} \mid$ plotted against time for shearing at 10 rad/s and $T = 120°C$ with strain amplitude varied from 0.3 to 1. Sparsely spaced markers have been used.

10 rad/s exhibited a strong connection with the effective dynamic modulus ($\mid G^*_{eff} \mid$) (Figure 4.12e and 4.12f). Across large differences in strain amplitudes for each shearing condition, intermediate states having nearly similar orientation distribution (to the extent this is indicated by uniformly equal $\Delta n^{(d)}_{13}(t)$ values) have similar modulus (Figure 4.12f). This correlation suggests that the effective modulus at $\omega = 10$ rad/s, $T = 120°C$ and $\gamma_o = 0.4$ to 1.0, is largely determined by the orientation distribution of the lamellae. This may be a consequence of the smaller strain softening effect observed at 10 rad/s compared to 1 rad/s.

ω =30 rad/s at 120°C: For the strain amplitudes probed *i.e.* from 0.5 to 0.7, a small

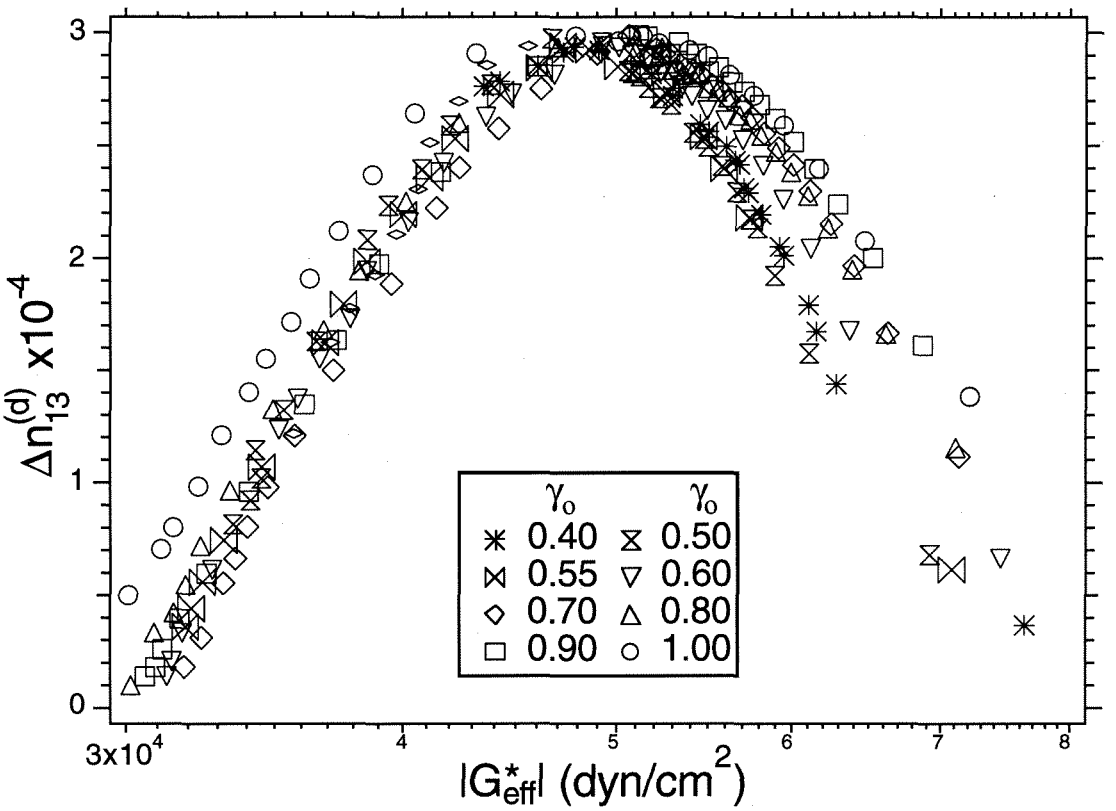

Figure 4.12f: Transient birefringence plotted against the effective modulus ($\mid G^*_{eff}(t) \mid$) measured during alignment at different strain amplitudes. Sparsely spaced markers have been used.

value of $\Delta n_{13}^{(d)}(t)$ was observed throughout the alignment process (Figure 4.13). The small-strain dynamic moduli measured after shearing were identical to those obtained after shear at 10 rad/s. Therefore, the final state was inferred to be aligned in the parallel orientation. The small value of birefringence throughout the process could be interpreted in terms of a continual decrease of the projections of the orientation distribution along the perpendicular and the transverse directions at comparable rates, and continual increase of the projection along the parallel direction ($S_{11}, S_{33} \rightarrow\sim 0$ and $S_{22} \rightarrow\sim 1$). Furthermore in this case, the transient birefringence at different strain amplitudes was quite distinct, and rescaling time could not superpose any part

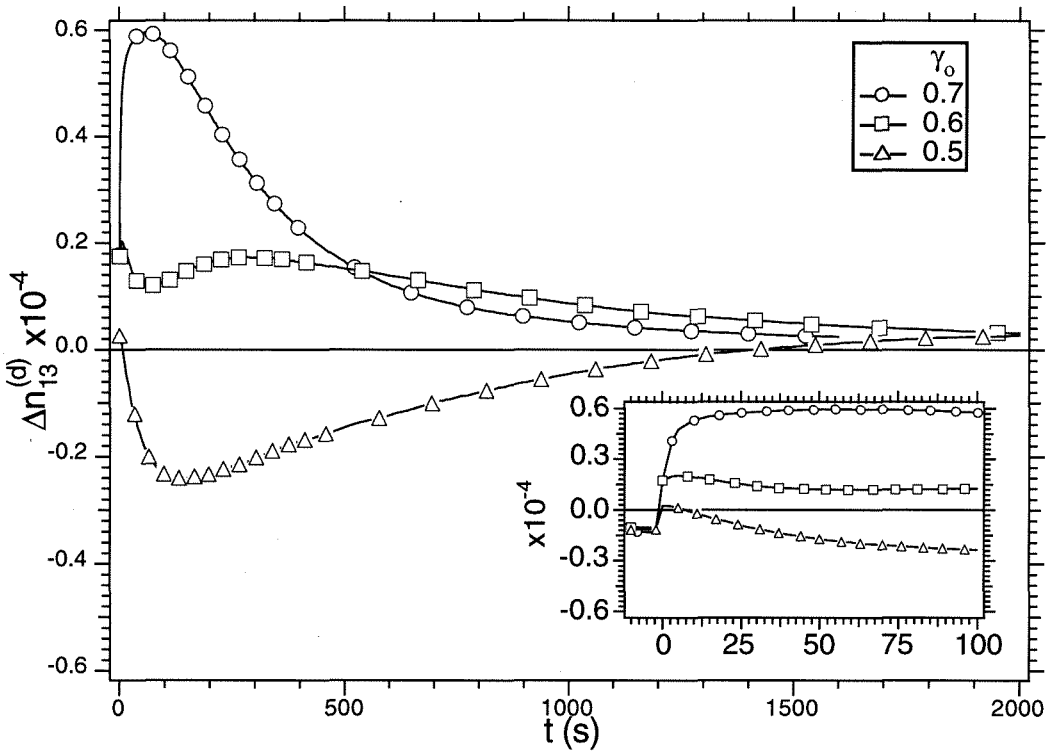

Figure 4.13: Transient 1,3-birefringence observed during shearing at $T = 120°C$, $\omega = 30$ rad/s and different strain amplitudes. Sparsely spaced markers have been used to distinguish between the curves.

of the different curves.

ω =100 rad/s at 120°C: As at 10 rad/s, the rate of alignment at 100 rad/s increased with strain (Figure 4.14a). However, unlike at 10 rad/s, strain amplitude produced a large effect on the extremum value of $\Delta n_{13}^{(d)}(t)$ obtained during shear at 100 rad/s. Shearing at $\gamma_o \geq 0.3$ produced parallel alignment via distinctive fast and slow processes. In contrast, at $\gamma_o = 0.2$, $\mid \Delta n_{13}^{(d)}(t) \mid$ increased throughout the shearing process analogous to the case of shearing at 10 rad/s using $\gamma_o = 0.3$. However, as the birefringence here was negative, this tended to indicate a biaxial orientation distribution with enhanced projections (in the 1,3-plane) of the parallel and transverse orientations. Biaxial orientation (along the same two directions) was

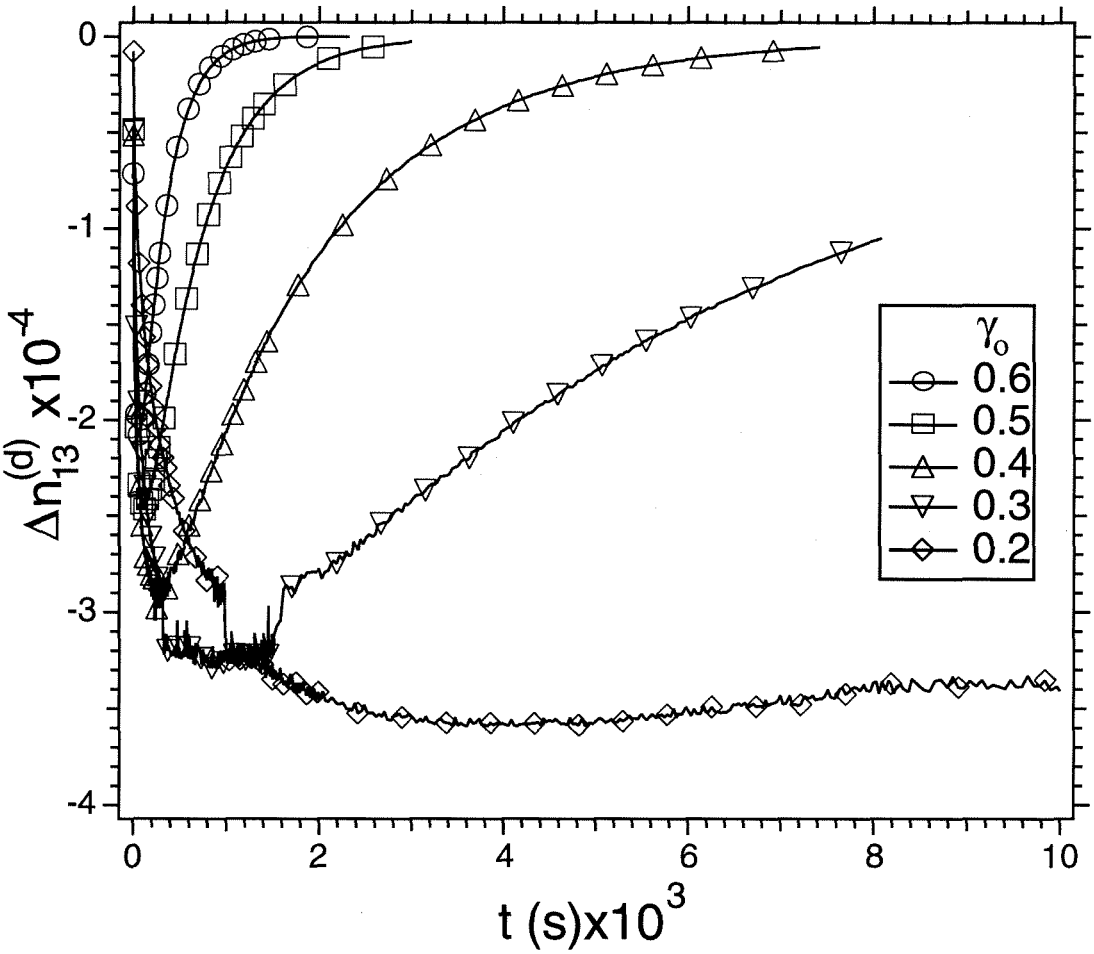

Figure 4.14a: Transient 1,3-birefringence observed during shearing at $T = 120°C$, $\omega = 100$ rad/s and different strain amplitudes.

recently reported by Okamoto *et al.* [85] working with polystyrene-poly(ethylene-alt-propylene) diblock melts, and by Pinheiro *et al.* [94] using blends of PS-PI with polystyrene.

Because the minimum value of $\Delta n_{13}^{(d)}(t)$ was not constant across the different strain amplitudes, rescaling time in terms of strain cannot fully describe the strain dependence. However, to provide a comparison with the results at 10 rad/s, we obtained rough estimates: the fast process showed an approximate time-scaling as the cubic power (γ_o^3) while the slow process exhibited a scaling of approximately γ_o^4.

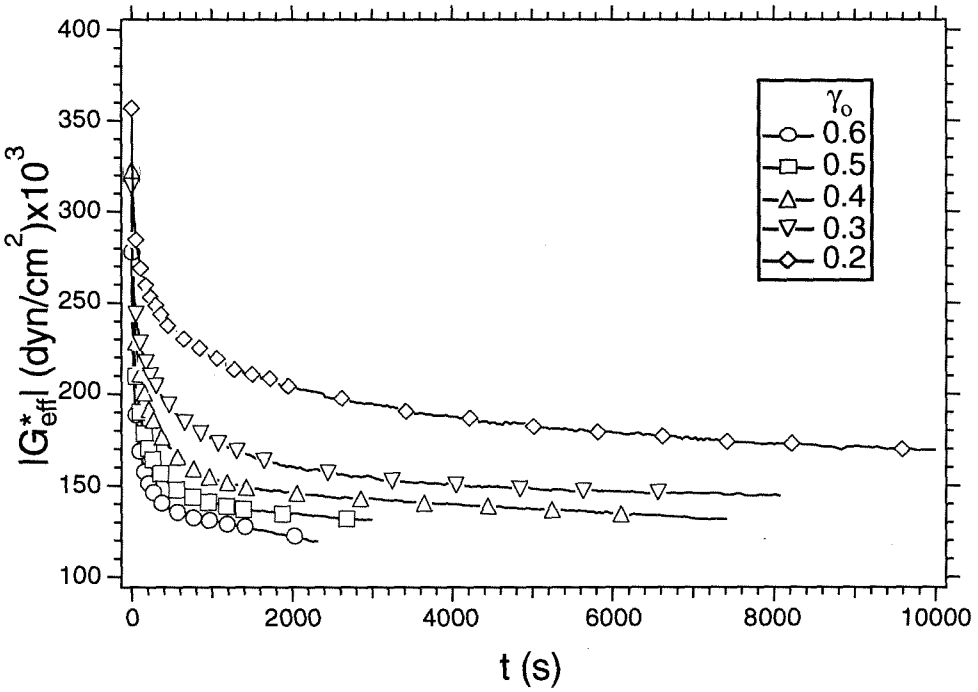

Figure 4.14b: Magnitude of the effective modulus $\mid G^*_{eff} \mid$ plotted against time for shearing at 100 rad/s and $T = 120°C$ with strain amplitude varied from 0.3 to 1. Sparsely spaced markers have been used.

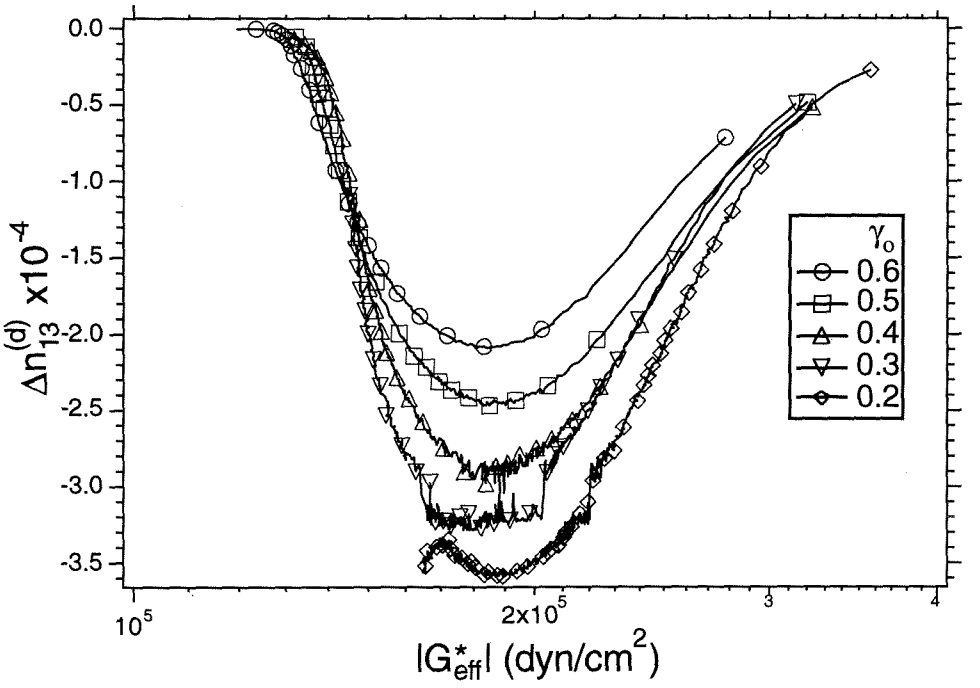

Figure 4.14c: Transient birefringence plotted against the effective modulus ($\mid G^*_{eff}(t) \mid$) measured during alignment at different strain amplitudes. Sparsely spaced markers have been used.

A relationship between $\Delta n_{13}^{(d)}(t)$ and ($\mid G_{eff}^{*}(t) \mid$) is again evident (Figures 4.14b and 4.14c). The family of curves of $\Delta n_{13}^{(d)}(t)$ *vs* ($\mid G_{eff}^{*}(t) \mid$) have similar shapes, and the effective modulus corresponding to the minima in $\Delta n_{13}^{(d)}(t)$ is nearly constant ($\mid G_{eff}^{*} \mid \sim 1.9 \times 10^{5}$) for the different strain amplitudes (Figure 4.14c). The curves differ in the vicinity of the minimum of $\Delta n_{13}^{(d)}(t)$ due to a decrease in the minimum of $\Delta n_{13}^{(d)}(t)$ with increasing strain (Figure 4.14a).

4.3.4 Effect of Temperature (T)

In an ordered block copolymer, dynamic and thermodynamic changes with temperature are expected to affect the dynamics of shear induced alignment, including the dependence of alignment on shear frequency and strain amplitude. We explore these effects by performing shearing experiments at temperatures lying above the T_g of the PS-rich microphase and below the T_{ODT}.

Prolonged shear over several hours at 100°C ($a_T\omega \approx 45.5$ rad/s and 455 rad/s) was possible only using moderate strain amplitudes ($\gamma_o \preceq 0.3$). Higher strain amplitudes were not used due to limitations of our force transducer and flow cell geometry and due to the possibility of melt fracture. At these lower strain amplitudes, the birefringence saturated at intermediate negative values and was neither indicative of parallel alignment (*i.e.* near zero) nor indicative of perpendicular alignment.[11] The negative transient birefringence suggested a state with a mix of orientations such that the projection of the orientation distribution along the transverse direction was higher than

[11] Previous studies of shear alignment in PS-PI [34, 40, 39] have reported parallel alignment at low temperatures (near the T_g of polystyrene-rich microphase) even using strain amplitudes as low as 0.05.

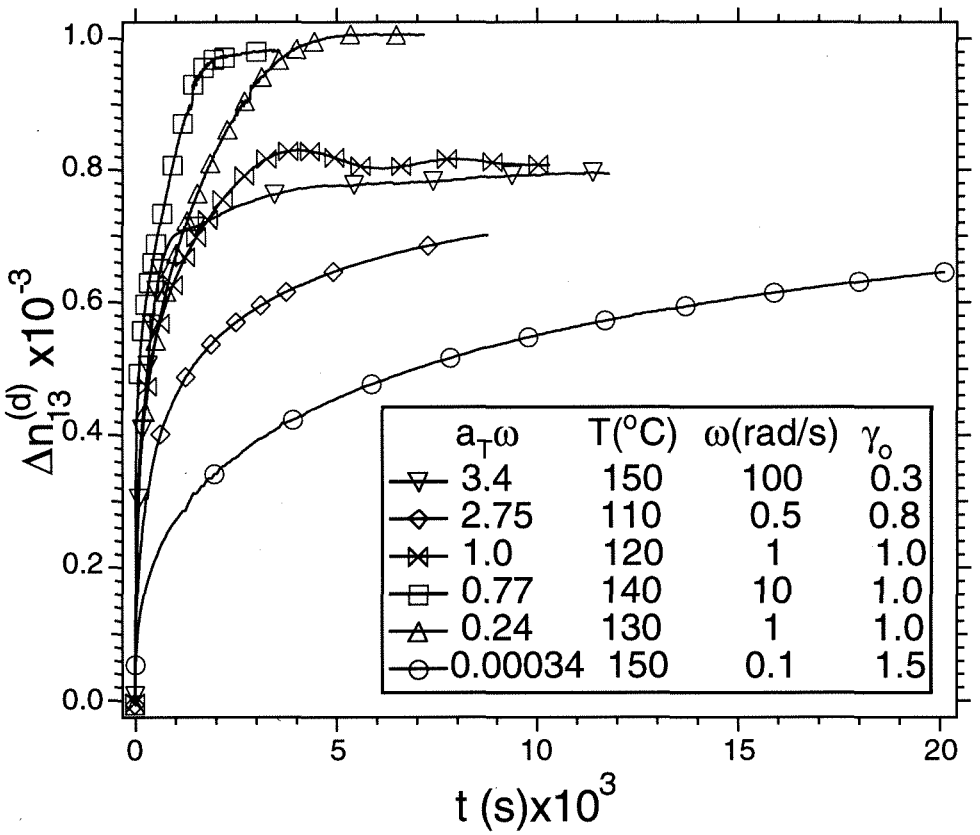

Figure 4.15a: Transient birefringence observed during perpendicular alignment at various reduced frequencies. Sparsely spaced markers have been used.

that along the perpendicular direction. Similar results for the transient birefringence were observed at a higher temperature of 110°C (for $a_T\omega \approx 11$ rad/s and 55 rad/s). Therefore, we could not unambiguously assign an alignment direction for a number of the shearing experiments at 110°C. The only exception was at $a_T\omega \approx 2.75$ rad/s and 110°C, where shearing produced a large and positive birefringence ($\sim 7 \times 10^{-4}$) and indicated imperfect perpendicular alignment (Figure 4.15a).

At temperatures higher than 120°C but below T_{ODT} it was possible to use larger strain amplitudes, which induced alignment within a few hours. However, with increasing temperature, fewer shearing conditions (within the frequency range of our

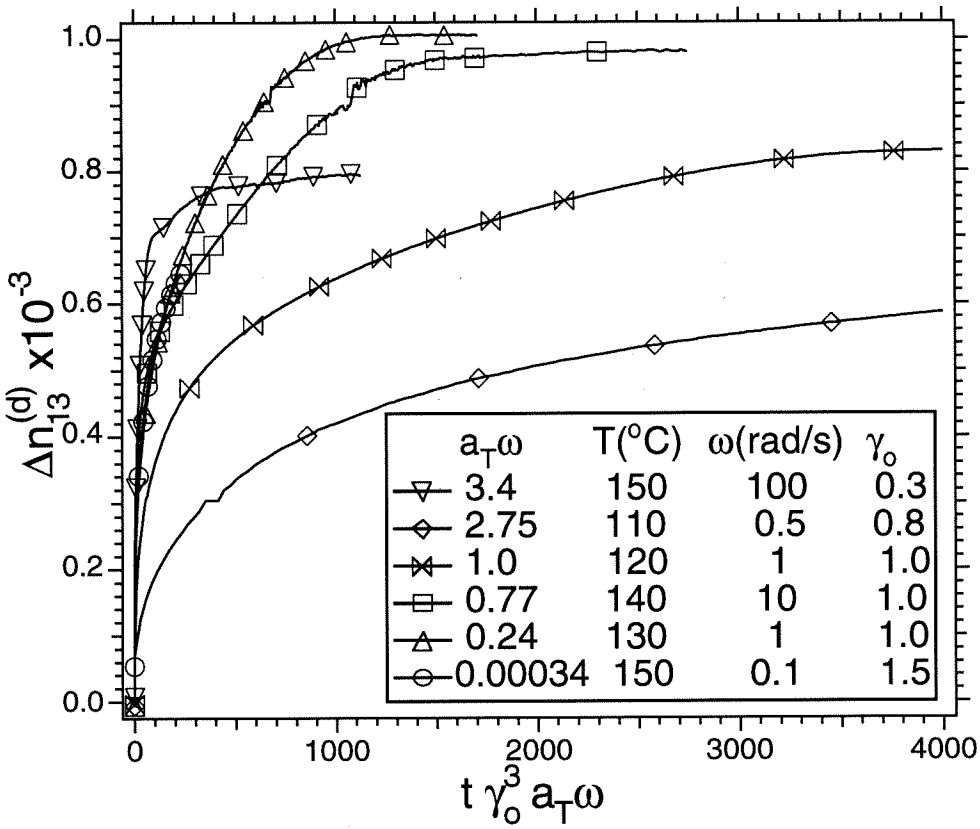

Figure 4.15b: Transient birefringence for conditions shown in Figure 4.15a plotted as a function of scaled time. Sparsely spaced markers have been used.

rheometer) induced parallel alignment. Beyond 130°C we were able to achieve only perpendicular alignment.

As perpendicular alignment was produced at all temperatures ranging from 110°C to 150°C, it is convenient to explore the interplay of temperature with shear frequency and strain amplitude by comparing the evolution of $\Delta n_{13}^{(d)}(t)$ at different temperatures, en route to perpendicular alignment (Figure 4.15a). Relative to the transient birefringence observed at $T = 110$°C ($a_T\omega = 2.75$ rad/s) and 120°C ($a_T\omega = 1$ rad/s), a faster and larger rise in $\Delta n_{13}^{(d)}(t)$ was observed at $T = 130$°C ($a_T\omega = 0.24$ rad/s) and 140°C ($a_T\omega = 0.77$ rad/s) (Figure 4.15a). However, we cannot perform a comparison

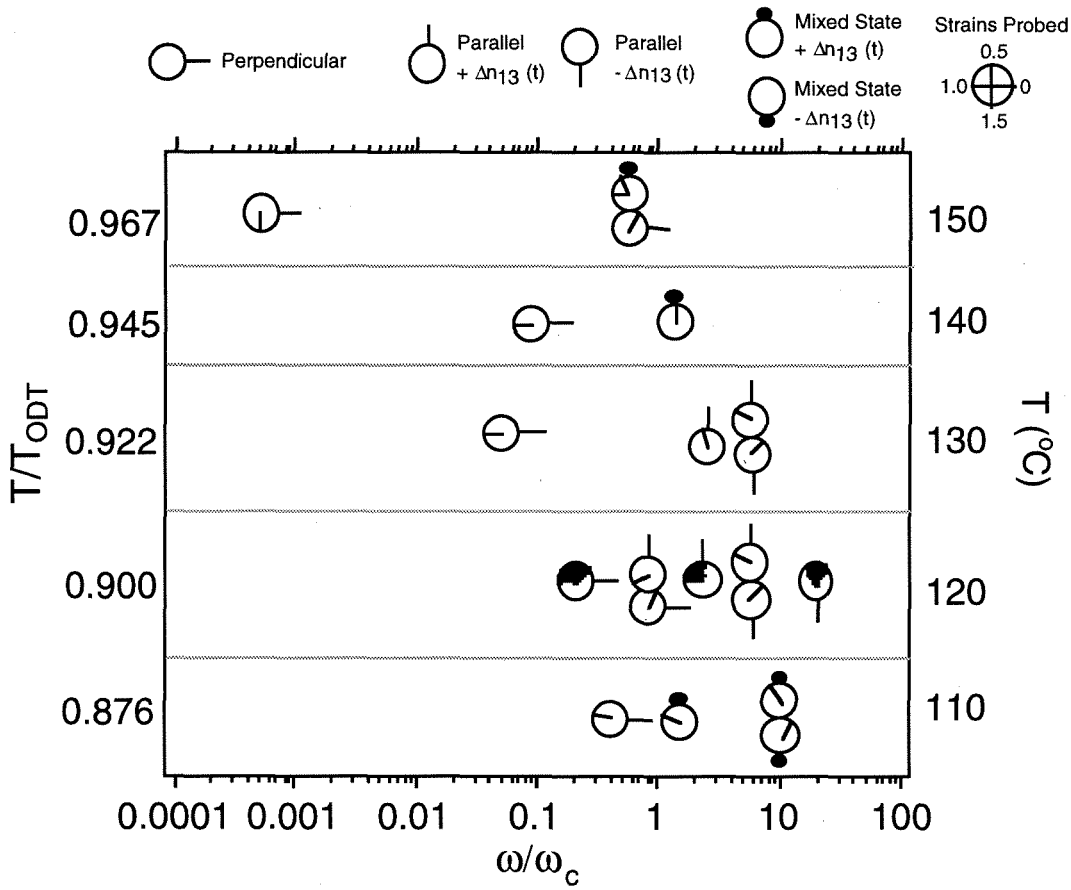

Figure 4.16: Summary of alignment results. The final state of alignment (or non-alignment) is indicated on the outside of each circular marker. For alignment indicated as perpendicular, the transient birefringence trace is similar to that shown in Figure 4.11a. The strain probed is marked within the circular marker. Filled regions indicate more than one strain amplitude were probed. Two circles atop each other indicate different alignment results with different strain amplitudes but at a fixed frequency and fixed temperature. Results at temperature lower than 110°C are not shown as strain amplitudes lower than 0.3 were used and we did not observe definitive alignment.

across shearing conditions with different T, ω and γ_o by considering $\Delta n_{13}^{(d)}(t)$ simply as a function of real-time (t). Therefore, we plot $\Delta n_{13}^{(d)}$ as a function of scaled time $t\gamma_o^3 a_T\omega$, where the variation of frequency (ω) and temperature are combined using a_T, and effect of strain amplitude accounted for by using γ_o^3 (Figure 4.15b, *c.f.* Figure 4.11b). While not completely capturing the dependency of the alignment process on temperature, frequency and strain, such a scaling is effective in partially superposing the transient birefringence, especially at $a_T\omega = 0.77, 0.24$ and 0.00034 rad/s. Furthermore, on this scaled time, as $a_T\omega$ decreases we observe faster evolution of $\Delta n_{13}^{(d)}$ for all frequencies except $a_T\omega = 3.4$ at 150°C (Figure 4.15b).[12]

As in Koppi *et al.* [28], we can represent our collective alignment results at different temperatures on a plot of T/T_{ODT} *vs.* ω/ω_c' (Figure 4.16). However, it is important to note that we have probed only a limited number of shearing conditions at temperatures other than 120°C. In light of our discovery that strain amplitude is extremely relevant in determining the final state of alignment, we believe more extensive testing is required to map out the alignment behavior. As in other studies [28, 34, 40, 95], we find that the change in chain dynamics with temperature is indeed a major factor in determining the ultimate alignment direction. Time-temperature superposition for shifting the frequencies of alignment used at different temperatures demarcates two regimes for PS-PI— low $a_T\omega$ inducing perpendicular orientation, and

[12]The exclusion of $a_T\omega = 3.4$ (*i.e.* 150°C and 100 rad/s) from the trend may be because at this reduced frequency shearing at higher strains ($\gamma_o \sim 1.0$ as opposed to 0.3) results in $\Delta n_{13}^{(d)}(t)$ typical of parallel alignment. Though, $\Delta n_{13}^{(d)}(t)$ did not decrease completely to zero and resulted in a mixed state of alignment. Thus, this condition is reminiscent of 4 rad/s and 120°C, where strain amplitude plays a dominant role with low γ_o (~ 0.4) inducing perpendicular alignment and $\gamma_o \sim 1.1$ leading to parallel alignment (Figure 4.10a).

high $a_T\omega$ leading to parallel orientation (Figure 4.16). For parallel alignment in PS-PI, an additional regime at very low reduced frequencies *i.e.* at temperatures close to T_{ODT}, has been found recently by Zhang *et al.*. [80] However, we are unable to obtain parallel alignment in our PS-PI material at such high temperatures (close to T_{ODT}) and low frequencies; instead we find strong perpendicular alignment even at the lowest reduced frequency we access in our experiments $a_T\omega \sim 3.5 \times 10^{-4}$ rad/s (see Figure 4.16). Patel *et al.* [95] have also found only perpendicular alignment at the lowest reduced frequencies they probe—shearing at $\omega = 0.01s^{-1}$ and $T = 145°C$ for a PS-PI sample with $T_{ODT} = 152°C$.

4.4 Discussion

4.4.1 Monitoring the Alignment Process

To achieve a fundamental understanding of the flow alignment process, it is essential to record material properties that sensitively reflect changes occurring during alignment. In most previous studies, no measurement of stress or microstructure were made during shearing. In a few cases the stress has been recorded during the process [26, 27, 34, 39, 40, 78]. In addition, numerous authors have noted the effects of alignment on the small strain dynamic moduli [26, 28, 29, 34, 39, 40, 78]. These raise the question whether either the effective moduli (or viscosity) during the alignment process or the dynamic moduli at intermediate states of alignment can provide a means to monitor microstructural changes in the sample. In our experiments, neither G^*_{eff} nor

$G^*(\omega)$ at intermediate stages sensitively reflect microstructural changes. In contrast, the transient birefringence dramatically reveals the evolution of the microstructure during flow alignment.

Dynamic Moduli: In all the cases examined for both alignments, G^*_{eff} goes through an initial drop which is only modestly larger en route to parallel alignment than to perpendicular (Figures 4.4b, 4.6b and 4.10b). We believe that this rapid drop in the modulus results from the large and rapid changes in the defect density together with changes in the orientation distribution that occur in the early stages of large amplitude shearing. Following this initial drop, G^*_{eff} shows little change in magnitude compared to the significant changes in the magnitude of $\Delta n^{(d)}_{13}$. These changes in $\Delta n^{(d)}_{13}$ at lower frequencies (*e.g.*, 1 rad/s and 10 rad/s at 120°C) reflect the changing proportions of lamellae along perpendicular and parallel directions. Since, at these frequencies (*i.e.*, 1 rad/s and 10 rad/s) perpendicular and parallel orientations do not show large differences in their dynamic moduli (Figures 4.4c and 4.6c), we expect a correspondingly flat portion in G^*_{eff}. However, a similar reasoning fails to describe the behavior of G^*_{eff} at higher frequencies (*i.e.*, 100 rad/s at 120°C), where large differences in the dynamic moduli exist between different orientations (a mix of transverse and parallel at the end of the "fast" process), but nevertheless G^*_{eff} changes little during the slow process (as transverse is eliminated).

Like G^*_{eff}, the low strain dynamic moduli ($G^*(\omega)$) measured at intermediate states of alignment show only slight sensitivity to the evolution of the microstructure during shear. Furthermore, the changes in $G^*(\omega)$ can be non-monotonic. Variations in both

G' and G'' are gradual for a large part of the alignment process (Figures 4.5, 4.7 and 4.8), in spite of considerable changes in the microstructure as revealed by the birefringence. Microstructures with very different orientation distributions appear to have essentially the same $G^*(\omega)$. Thus, even if the relationship between microstructure and $G^*(\omega)$ were known, it would be impossible to infer the orientation distribution from $G^*(\omega)$.

Birefringence: In the present system (PS-PI) the form effect dominates the birefringence, so the birefringence is directly related to the second moment of the orientation distribution of the lamellae. To a good approximation, the deviatoric parts of the refractive index tensor ($\Delta\mathbf{n}$) and the order parameter tensor $\mathbf{S}$ are proportional:

$$\Delta\mathbf{n} = -n_o(\mathbf{S} - \mathbf{I})$$

where $S_{ij} = \langle u_i u_j \rangle$, with $\mathbf{u}$ being the normal to the lamellae and $\langle ... \rangle$ denoting an average over the orientation distribution, $\mathbf{I}$ is the identity tensor, and n_o is a constant of proportionality that depends on the strength of segregation and the resulting periodic variation of the mean refractive index. Empirically, n_o can be determined from birefringence measurements in samples in which the orientation distribution is known. We estimate the value of n_o for the present sample at 120°C by the largest birefringence we have ever observed for a perpendicular aligned sample, $\Delta n_{max} \simeq 10 \times 10^{-4}$. Using TEM we are currently characterizing the orientation distribution in samples that show such high birefringence values. We believe this value of n_o corresponds to a very highly aligned state since it is more than half the value observed and calculated

for strongly segregated PS-PI, which should consequently have a much larger value of n_o than the present samples. Therefore, we will frequently compare the birefringence of samples to this benchmark value.

Complete characterization of (**S** - **I**) requires the value of n_o and measurement of at least two projections of the refractive index tensor. In the present experiments, we are limited to observing just one projection.[13] Therefore, we can provide bounds on the orientation distribution and make reasonable inferences about the trajectory of orientation. Ongoing TEM and SAXS measurements on samples removed at intermediate states of alignment will provide the basis for more definitive interpretation.

Large 1,3-birefringence values provide relatively unambiguous results. In particular, $n_{11} - n_{33} = n_o$ can only correspond to an order parameter tensor with $S_{33} = 1$ as its only non-zero component. This corresponds to perfect perpendicular alignment. Similarly, $n_{11} - n_{33} = -n_o$ can only mean **S** has $S_{11} = 1$ as its only non-zero component, which would correspond to perfect "transverse" alignment. The interpretation becomes more ambiguous as the birefringence decreases. Observing zero birefringence in the 1,3-plane can correspond to any uniaxial distribution

$$\mathbf{S} = \begin{bmatrix} \epsilon/2 & 0 & 0 \\ 0 & 1-\epsilon & 0 \\ 0 & 0 & \epsilon/2 \end{bmatrix}.$$

Here, we have neglected $S_{12} = S_{21}$ since it averages to zero over a cycle of shear (an odd function of strain); in the present flow geometry, S_{13}, S_{31}, S_{23} and S_{32} are zero by

[13]For reasonable flow geometries, the 1,2-projection results in a retardation over too many orders due to large path length ($\sim$ 15mm in our experiments).

symmetry. The initial, unaligned state with a random grain orientation distribution corresponds to the case $\epsilon = \frac{2}{3}$; and a perfect parallel alignment corresponds to $\epsilon = 0$. Therefore in our experiments, when the birefringence is small, we take into account the dynamic modulus, previous SAXS and TEM studies on similar materials, and context within an overall trajectory [34, 39, 40].

4.4.2 Evolution of Alignment

Upon application of large amplitude shear, distinct changes in the orientation distribution occurring at vastly different time scales are evident in the evolution of birefringence. During both parallel and perpendicular alignments, we observe an initial "fast" and a subsequent relatively "slow" change in the transient birefringence.

The initial condition on each experiment is obtained by annealing at a temperature above the microphase transition temperature (*i.e.* T_{ODT}), and then cooling to 120°C in the ordered state. We expect that the resulting sample morphology consists of randomly oriented lamellar grains [40]. The order parameter tensor in this state can be described as $S_{11} = S_{22} = S_{33} \simeq \frac{1}{3}$, which is consistent with the near zero 1,3-birefringence observed prior to large amplitude shear.[14] Flow induced changes in the lamellar orientation distribution (or the order parameter tensor) can be visualized from the transient birefringence, guided by its sign and magnitude.

Perpendicular Alignment:

Large amplitude shearing at 1 rad/s at $T = 120°C$ produces a rapid positive rise

[14] In the microphase separated state for block copolymers a small apparent birefringence results from depolarization of the polarized light upon transmission through a collection of randomly oriented lamellar grains.

in $\Delta n_{13}^{(d)}$ (Figure 4.4a). This "fast process" can be interpreted as a dominant rapid decrease of S_{11} relative to S_{33}, indicating depletion of the grains biased towards the transverse (axis 1) direction. Furthermore, during this initial fast process the birefringence reaches point 'c' ($\sim \frac{2}{3}\Delta n_{max}$) on Figure 4.4a within $\sim$ 600 s. This large magnitude of $\Delta n_{13}^{(d)}$ strongly suggests a simultaneous rapid increase of S_{33}, *i.e.* the projection of the orientation distribution along the perpendicular direction (axis 3). Thus at point 'c', the order parameter tensor corresponds to grain orientations distributed across parallel and perpendicular directions, with the latter dominating.

Beyond point 'c', a much slower perfection of the alignment occurs, indicated by a gradual increase in $\Delta n_{13}^{(d)}$ towards n_o. This may correspond to gradual depletion of the projection of the orientation distribution in the parallel direction ($S_{22} \rightarrow\sim 0$), and a final alignment along the perpendicular direction ($S_{33} \rightarrow\sim 1$).

Parallel Alignment:

During alignment at frequencies from 100 to 10 rad/s (at $T = 120°C$), unambiguous interpretation of the trajectory of alignment from 1,3-birefringence is difficult. However, here the small-strain moduli measurements at intermediate stages (Figure 4.7) and in the final aligned state complement the birefringence measurements, and allow visualization of the trajectory of alignment.

At 100 rad/s (Figure 4.6a), the initial rapid decrease in $\Delta n_{13}^{(d)}$ to approximately $-\frac{1}{3}n_o$ suggests a rapid depletion of the projection along the perpendicular direction ($S_{33} \sim 0$) while the projection along the transverse, which is believed to be the least preferred direction, remains relatively unchanged from the initial isotropic state

($S_{11} \sim \frac{1}{3}$). Since both $G'(\omega)$ and $G''(\omega)$ at point 'a' on Figure 4.6a are considerably smaller than those of the unaligned material (Figure 4.7)—quite unlike the case of perpendicular alignment— we infer that the projection along the parallel direction is enhanced. In contrast, the rapid rise of $\Delta n_{13}^{(d)}$ at 10 rad/s (Figure 4.6a) to approximately $\frac{1}{3}n_o$ indicates that here $S_{11} \rightarrow\sim 0$, while S_{33} remains unchanged and S_{22} increases.

At frequencies from 60 to 20 rad/s ($T = 120°C$), the initial fast change is much less apparent and $\Delta n_{13}(d)$ remains close to zero. In the context of a final parallel alignment, this would indicate that the projections along both perpendicular and transverse directions decrease at comparable rates (Figure 4.9). In all cases, *i.e.* 10-100 rad/s, at the end of the initial "fast" process the order parameter tensor corresponds to an orientation distribution depleted in its projection along either perpendicular (at 100 rad/s) or transverse directions (at 10 rad/s), or both (60-20 rad/s), and increased projection along the parallel direction.

As in the case of perpendicular alignment, during the slower process the direction of alignment is perfected, with the final value of $\Delta n_{13}^{(d)} \approx 0$ indicating an almost complete disappearance of the projection of the orientation distribution in the 1,3-plane.

Frequency Regime In-Between Parallel and Perpendicular Alignment:

Shear frequency appears to play a decisive role in selecting the route to either parallel or perpendicular alignment (Figure 4.17). In particular, for the the initial "fast" change during shearing at 120°C:

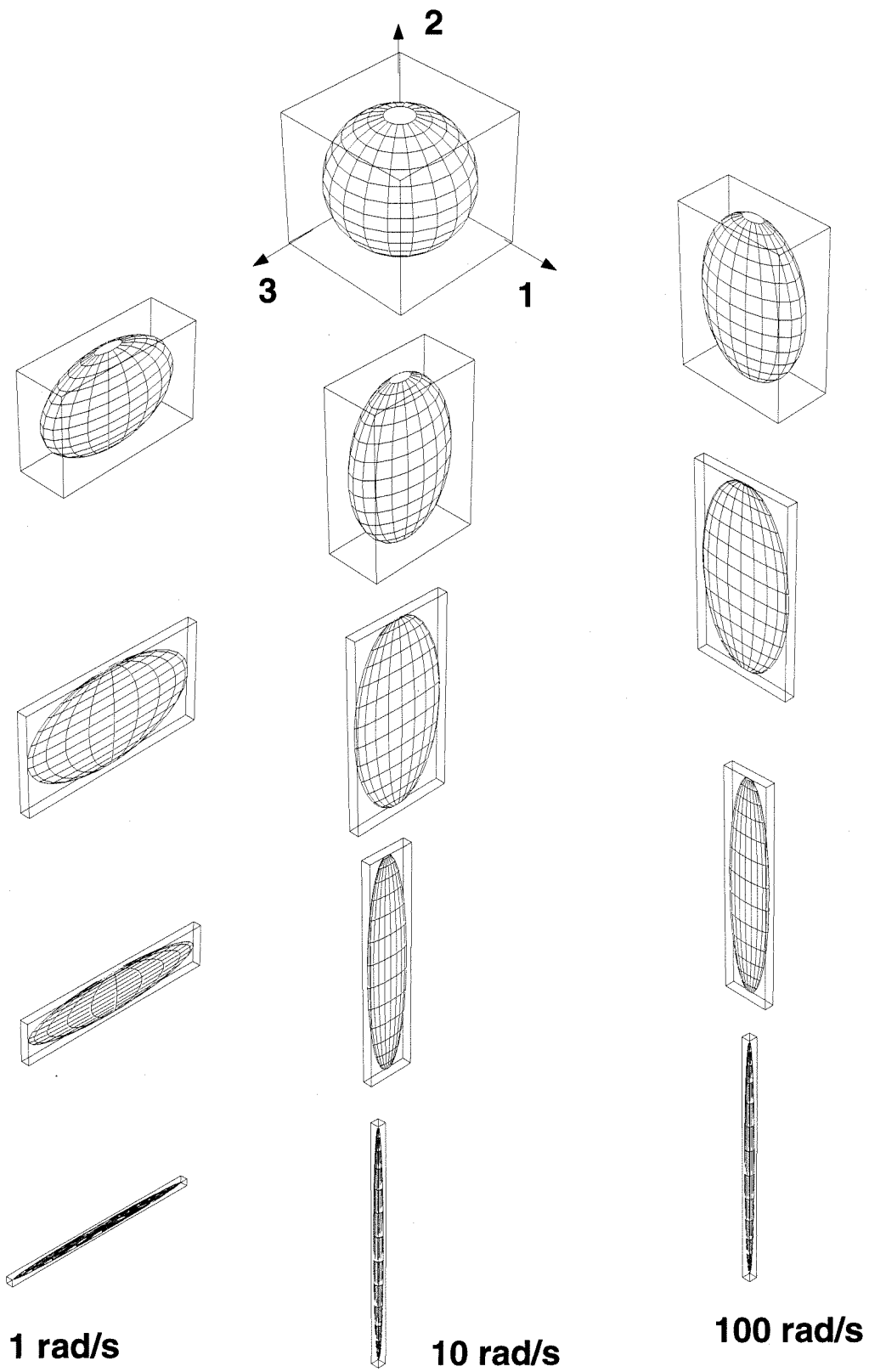

Figure 4.17: Schematic representation of the changes in lamellar orientation distribution during perpendicular and parallel alignment.

1. for $\omega \geq 30$ rad/s, S_{33} decreases relative to S_{11}, while S_{22} increases;

2. for 10 rad/s $\leq \omega \leq 30$ rad/s, S_{11} decreases relative to S_{33}, while S_{22} increases, and

3. for $\omega = 1$ rad/s, S_{11} decreases relative to S_{33}, with S_{33} increasing.

As shearing frequency is reduced from 10 to 1 rad/s (at 120°C), the character of the "fast" alignment process shifts from enriching the parallel projection to enriching the perpendicular projection at the expense of the transverse projection of the orientation distribution. Such a shift is also reflected in results during shearing at 4 rad/s. Enrichment of the perpendicular projection during the fast process, both for $\gamma_o = 1.1$ and $\gamma_o = 0.4$, is indicated by transient birefringence that exceeds $(1/3)n_o$ (Figure 4.10a).

During the subsequent slower process at 4 rad/s, strain plays a critical role—selecting the ultimate direction of alignment: for $\gamma_o = 1.1$, the perpendicular projection disappears during the slow process, while for $\gamma_o = 0.4$ the parallel projection decreases. At other frequencies, the effect of strain on the slow process is also profound: below a critical strain, the slow process does not appear to occur, and the alignment is never perfected.

4.4.3 Implications of our Results

On Mechanisms of Alignment

The interplay of strain amplitude and shear frequency in determining the route of alignment has significant implications on the different pictures put forward by

previous researchers to explain selection of the route and direction of alignment in block copolymers. It has been argued that flow energy ($\sim \sigma\gamma_o$) could overcome the microphase-separation energy and disrupt the lamellar microdomains, which followed by a reformation along a preferred direction would lead to alignment [24, 26, 34]. The choice of a preferred direction (parallel or perpendicular alignment) is believed to depend critically on the shear rate [28, 34, 39]. However, the whole suite of results outlined in section 4.3 indicate that alignment is not simply controlled by either the shear rate, the cumulative strain or the flow-energy. For instance at 120°C:

1. shearing conditions of [ω = 10 rad/s, $\gamma_o = 1$] and [ω = 30 rad/s, $\gamma_o = 0.5$] are not widely separated in terms shear rate ($\sim \omega\gamma_o$), but show drastically different transient birefringence (Figures 4.12a and 4.13), and correspondingly distinct microstructural changes;

2. $\Delta n_{13}^{(d)}(t)$ observed during shearing at a particular frequency (*e.g.*, 1 rad/s, 10 rad/s or 100 rad/s) but different strain amplitudes (γ_o) cannot be superposed using cumulative strain ($\sim \gamma_o t$)

3. flow energy ($\sim \mid G^*_{eff} \mid \gamma_o^2\omega$) during shearing at [30 rad/s, $\gamma_o = 0.7$] is similar to that during shearing at [100 rad/s, $\gamma_o = 0.3$], but the trajectory during alignment at these two conditions is dramatically different (birefringence in Figures 4.13 and 4.14a).

It has also been suggested that in PS-PI, the ultimate alignment direction at a particular shear rate and temperature is chosen to correspond with the minimum modulus (G^*) [95]. Indeed shearing is accompanied with a reduction in the modulus

[both G^*_{eff} and $G^*(\omega)$]. However, this reduction in modulus does not appear to underlie the selection between parallel and perpendicular alignment. In this PS-PI, consideration of the small-strain moduli would only yield parallel alignment, which is the lower modulus throughout the frequency range in our experiments. It could be argued that during large amplitude shear, the effective dynamic modulus would play a controlling role in determining the final direction of alignment. However, it is seen clearly that the greatest reduction in the effective modulus occurs within the first few hundred seconds of shear, while the microstructure is still far from macroscopic alignment in a particular direction. Furthermore, here again parallel alignment is associated with a larger decrease in G^*_{eff}—yet it is not the preferred direction of alignment at all shear frequencies. Even at the same shear frequency (4 rad/s and 120°C), different strain amplitudes lead to different final states of alignment even though a lower effective modulus during shearing is associated with the trajectory to parallel alignment (Figure 4.10b).

This result at 4 rad/s has profound implications regarding the concept of selective grain melting suggested to explain the disappearance of the domains biased in "unfavorable" transverse orientations. It has been speculated that the perpendicular orientation is the least susceptible to grain melting [28]. However, at 4 rad/s and 120°C oscillatory shear at the larger strain amplitude ($\gamma_o = 1.1$) induces parallel alignment, and at the lower strain amplitude ($\gamma_o = 0.4$) induces perpendicular alignment. One would expect that at the higher strain amplitude, which corresponds to a higher distortion of equilibrium layer spacing and greater disturbance of fluc-

tuations, selective grain melting would lead to even better perpendicular alignment, which is not the case. Thus, while grain melting may occur here, it cannot be the only mechanism determining the final state of alignment.

In almost all of the earlier experimental and theoretical studies [28, 32, 37, 79, 96] it has been proposed that the grains oriented along the transverse direction are the most unfavorable. It is argued that since these layers undergo compression, they are unstable and disappear rapidly either by rotation or melting or some combination of the two mechanisms. However, we observe that the rate of disappearance of grains with layer normals along the vorticity direction (*i.e.,* perpendicular direction) can surpass that for the transverse grains (*e.g.,* at 100 rad/s and 120°C). We are able to observe this phenomena only from an *in-situ* and *real time* study. From solely post-alignment characterization as done in most earlier studies, the samples shear aligned at 100 and 10 rad/s (120°C) exhibit identical final states. Only the *in-situ* transient birefringence measurements allow us to distinguish between the two very different trajectories.

On Multiple Mechanisms

As mentioned already, toward the goal of predicting the direction, degree and dynamics of flow-induced alignment, various authors have suggested mechanisms that might explain distinct orientations (*e.g.,* selective melting leading to perpendicular alignment) [28, 80]. Some investigators have suggested the possibility that two or more mechanisms may act in combination to produce alignment [26, 34]. Indeed, our results indicate that on the way to a given alignment, distinct processes may be occur-

ring. As alignment proceeds, there appears to be a transition in the character of the process, as though one process overtakes another in importance. This is manifested in the distinct strain dependence of the early ("fast") and the late ("slow") changes evident in the transient birefringence for each alignment trajectory (for example in Figures 4.12c-4.12d : at 10 rad/s and 120°C, the time scale varies with γ_0^5 for the fast process *vs* γ_0^3 for the slow process).

A competition between distinct processes is also suggested by the interplay of frequency and strain amplitude observed at certain "intermediate" frequencies. One example of such an intermediate frequency is between conditions leading to parallel alignment but via either a large, positive $\Delta n_{13}^{(d)}(t)$ or a large, negative $\Delta n_{13}^{(d)}(t)$. At $\omega = 30$ rad/s and $T = 120°C$, changes in strain amplitude qualitatively change the shape of the transient birefringence (Figure 4.13). The nature of this change is such that with increasing strain amplitude the transient $\Delta n_{13}^{(d)}(t)$ shows an increasing positive character, suggesting that the projection along the transverse direction is depleted more rapidly (relative to that along perpendicular) as γ_o increases from 0.5 to 0.7. A qualitatively similar trend is observed at $\omega = 100$ rad/s and $T = 120°C$ as γ_o increases from 0.2 to 0.6 (Figure 4.14a). In contrast, at 10 rad/s the peak height in $\Delta n_{13}^{(d)}(t)$ does not change from $\sim 3 \times 10^{-4}$ as strain amplitude increases form 0.4 to 1.0, perhaps indicating that here the initial projection of transverse is eliminated by the fast process regardless of strain amplitude.

Another example of an intermediate frequency where strain amplitude plays a controlling role is between the shearing conditions inducing parallel and perpendic-

ular alignment. At 4 rad/s and $T = 120°C$, strain has a more dramatic effect and selects the direction of flow-induced alignment (Figure 4.10a). This control of the final state of alignment by strain provides another valuable means to manipulate structure to induce coherent macroscopic order. However, it forces us to reexamine the role of different dynamical processes during alignment, and of the parameters controlling them.

4.4.4 Parameters Controlling Flow-Induced Alignment

It is widely accepted that the molecular and microstructural dynamics that cause alignment upon shearing are a function of the combined effects of temperature (T), molecular composition and shear frequency (ω) [24, 26, 28–33, 37, 77, 78, 96].

Among the several influences of temperature is the speeding-up (or slowing down) of the time scale for conformational relaxation of the polymeric constituents of the block copolymer. Typically this is accounted for by lumping the temperature effect into a single shift factor a_T; a procedure that does not capture the different extent of shifts for the different microphases. Temperature also couples with the molecular composition (via, χN) to alter the degree of segregation–in most cases, weaker segregation is achieved as $T \rightarrow T_{ODT}$. Consequently, higher temperatures reduce the viscoelastic contrast among the polymer blocks and also increase the rate of fluctuations. While the role of the former *i.e.* viscoelastic contrast has been acknowledged as a factor [78, 80, 95], it remains univestigated. Influence of the latter *i.e.* strength of fluctuations has been characterized by Koppi *et al.* [28] using T/T_{ODT} as a measuring

parameter.

Shear frequency is the other key factor during shear, and it is believed that shearing in different dynamical regions leads to either perpendicular or parallel alignment [28, 78, 80, 95]. Koppi *et al.* [28] have suggested three regimes: "domain or defect-controlled" regime at very low frequencies where the response on the scale of whole grains or domains (or defect dynamics) dominates; "microstructural" regime at frequencies where the distortion of the microphase separated structure dominates; and "polymeric" regime at sufficiently high frequency that distortion of macromolecular chains dominates viscoelasticity (demarcated from the "microstructural" regime by ω_c'). Thus, mapping alignment conditions [28] with respect to T/T_{ODT} and ω/ω_c' offers some insight into the role of both frequency and temperature and provides common grounds for comparison between different studies.

While shear frequency and temperature play important roles, they by no means are the only parameters during macroscopic alignment. At fixed ω and T, strain amplitude influences the stress response, the shear rate and the magnitude of distortion and can be expected to have significant consequences as well. Surprisingly, it has received little attention previously and only few results exist [26, 34, 83]. Winey *et al.* [34] have reported that for PS-PI melts, strain amplitudes lower than 0.01 do not induce alignment while $\gamma_o \simeq$ 0.01-0.05 is effective in alignment; at the chosen T and ω, strain amplitudes higher than 2.0 result in expelling the melt from their shear cell. Morrison *et al.* [26] have investigated SBS triblocks under steady shear and observed improved alignment as amount of strain imposed is increased. However, no system-

atic study of strain amplitude has been undertaken and scant attention has been paid in theoretical modeling to the effects of strain amplitude [30–33, 37, 77, 96].

The available theoretical literature on alignment also lacks treatment of the complex dynamics resulting from an orientation distribution within a polydomain material. Current theories focus almost exclusively on the properties of microstructures that are uniformly aligned, with an emphasis on elucidating the relative stability of monodomains in different orientations, when subjected to an applied field [30–33, 37, 77, 96]. However, as the orientation distribution has to evolve dynamically from that of a polydomain material to a well-aligned material, consideration of the stability of the ultimate microstructure cannot alone suffice.

Our results provide ample evidence of such an evolution. We find that the relative rates of transformation among the different projections of the orientation distribution are markedly influenced by both shear frequency and strain amplitude, and that by varying γ_o, ω and T, the trajectory of alignment can involve

- a rapid disappearance of the projection along the flow axis ($\hat{\mathbf{u}} \parallel 1$) with either an increase along the velocity gradient ($\hat{\mathbf{u}} \parallel 2$) axis enroute to parallel alignment, or an increase along vorticity axis ($\hat{\mathbf{u}} \parallel 3$) enroute to perpendicular alignment (manifested by $\Delta n > \frac{1}{3}\Delta n_{max}$).

- for parallel alignment, the projection of the orientation distribution along the vorticity axis ($\hat{\mathbf{u}} \parallel 3$) sometimes diminishes faster than that along flow axis ($\hat{\mathbf{u}} \parallel 1$).

Therefore, understanding the kinematics of grains during shear and understanding

the torques acting on "grains" is essential for insights into the mechanisms of alignment. A fundamental grasp of such issues would elucidate the physics underlying the reorientation of the grains and the process of ultimate alignment of the lamellae along a preferred direction. We believe that considerable opportunity exists in modeling and simulation of these effects, which in turn could yield valuable insights.

Our results serve usefully in discriminating between the existing ideas about alignment mechanisms, highlighting points of departure of current theories or hypotheses from the experimental observations. The results presented here also identify critical aspects of the alignment process, and establish the effects that future theories and computations need to capture to be successful in explaining flow alignment.

Appendix A

This appendix provides detailed information on the design for the mechanical and electronic components used in implementing polarization-modulation laser scanning microscopy (PMLSM). It also outlines the steps necessary for the operation of the technique.

A.1 Mechanical and Electrical Design

The incorporation of the polarimetric optical train on the microscope involves setting up appropriate polarization generation elements (PSG) that prepare the linear state of polarization of laser light and modulate its phase. As described earlier in Chapter 2, this requires insertion of a linear polarizer, a photoelastic modulator and a quarter-wave plate in the beam path.

To facilitate such a modification of the microscope, a module was custom designed to hold the optical elements. Important considerations for the design were that it match an existing reflector slider in the Zeiss LSM, which was necessary to insert it into the LSM. Space constraints also required minimization of the size of the module and the photoelastic modulator. The custom-made module (Hinds International, Oregon) has three parts each of which houses one optical element. These parts when assembled together can be exchanged with relative ease with the reflector slider (Figure A.1). Current module contains a dichroic sheet polarizer (Melles Griot Optics, Catalogue # 03FPG003, California) and a mica quarter-waveplate (Melles Griot Optics, Catalogue # 02WRM005, California). The photoelastic modulator is made of fused silica material and operates at a fundamental frequency of $\approx$ 63kHz

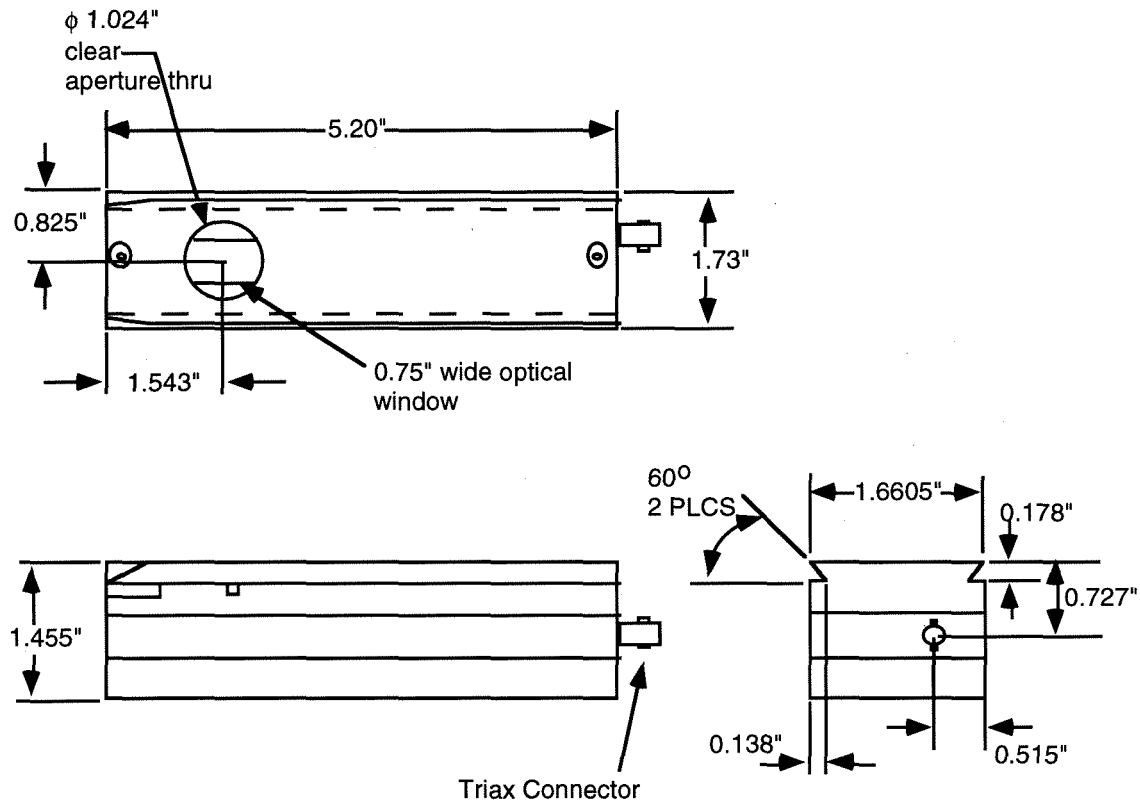

Fractions		± 1/32
Decimals	.XX	± .015
	.XXX	± .005
Hole Dia's	.XX	± .005
	.XXX	+ .003
		- .001
Angles		± 0°30'
Bends		± 2°
Perpendicularity		.003/inch
Concentricity		.003 TIR

Straightness &/or
Flatness .005/inch

Threads
External - Class 2A
Internal - Class 2B

Unmarked angles,
bends & intersections 90°

Machined Surfaces
63_J or better

Figure A.1: Mechanical drawings for the module designed to hold a linear polarizer, a photoelastic modulator and a quarter wave plate.

(Hinds International, Catalogue # 421003 with split head option #42000, Oregon). The modulator is provided with a broad band (450-650nm) anti-reflection coating.

Further modification for PMLSM requires the use of an external photodetector to transform the light intensity into an analog signal for demodulation. For transmission mode of operation, the photodetector assembly has to be placed on the luminous field diaphragm at the base of the microscope stand. Once again design specifications were set keeping in mind the dimensions of the diaphragm and the small-size constraint. Using a simple scheme, the detector element and the amplifying electronics were mounted in a plastic housing which was then attached to a metal ring designed to slip over the field diaphragm (Figure A.2). The Si photodiode (6pinDP Universal Detector) is operated in the photovoltaic mode using a amplifier circuit (Comlinear CLC401AP op-amp, Surtech, CA) (Figure A.3).

Normalization of the first and second harmonics of the modulated light intensity is performed using the steady (or dc) component of the detector signal. Digital techniques to achieve this division are incompatible with the rastering speeds employed for the laser. Therefore, analog ratio circuits have been built using a ratiometer (Evans Electronics, Catalogue # 4122, California) (Figure A.4). Analog circuits have also been built to provide baseline offset to the ratio of voltages (Figure A.5). This is important for negative ratios (lock-in signal (I_f or I_{2f}) normalized using I_{dc} from the low pass filter), since the negative voltages are replaced by zero values within the LSM image processor.

A relay switch provides an interface between the signal demodulation and the LSM

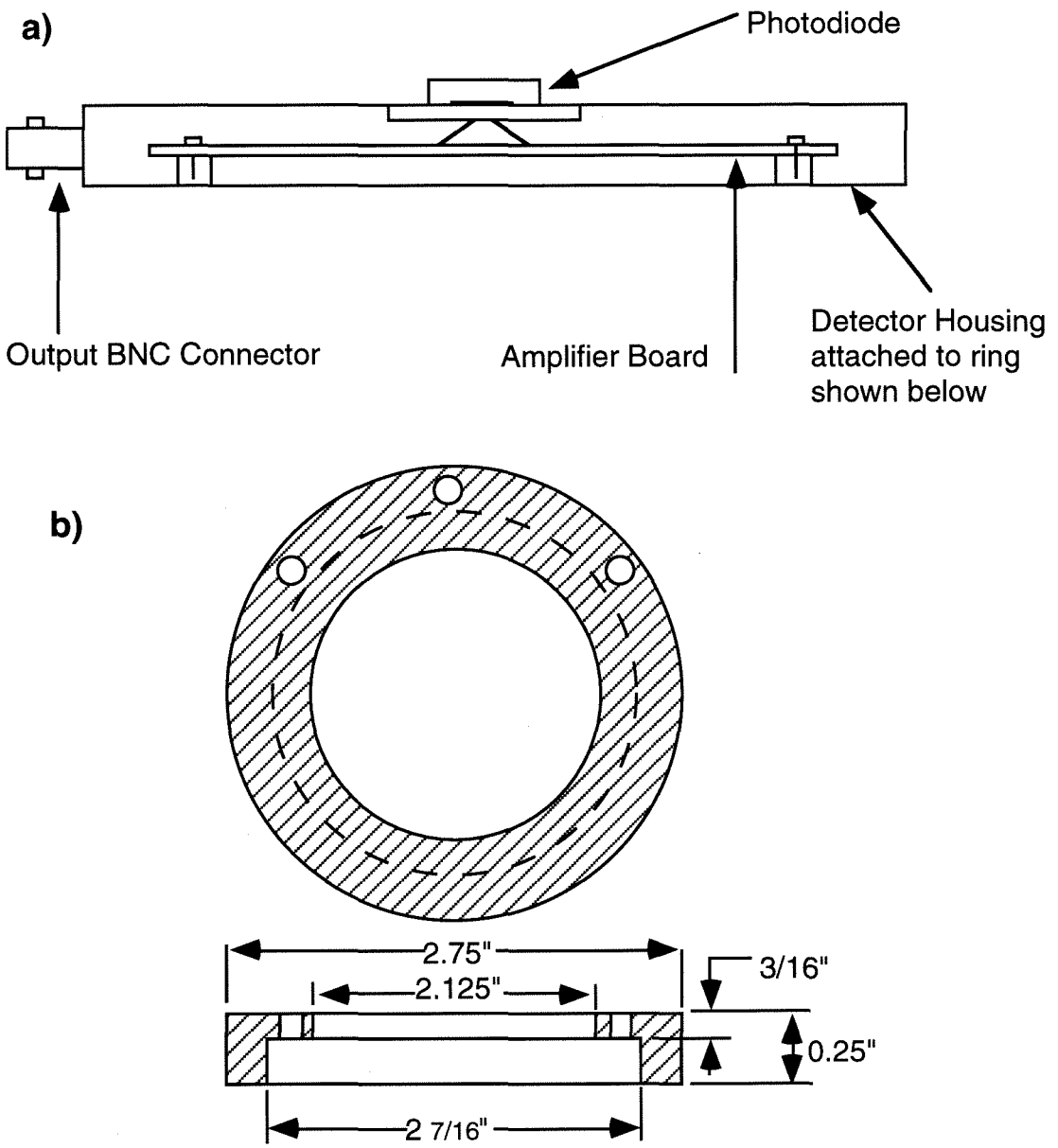

Figure A.2: (a) Schematic of the detector assembly as housed in a plastic box. (b) Design of the metal ring which attaches to detector housing and covers the field diaphragm of the Zeiss LSM.

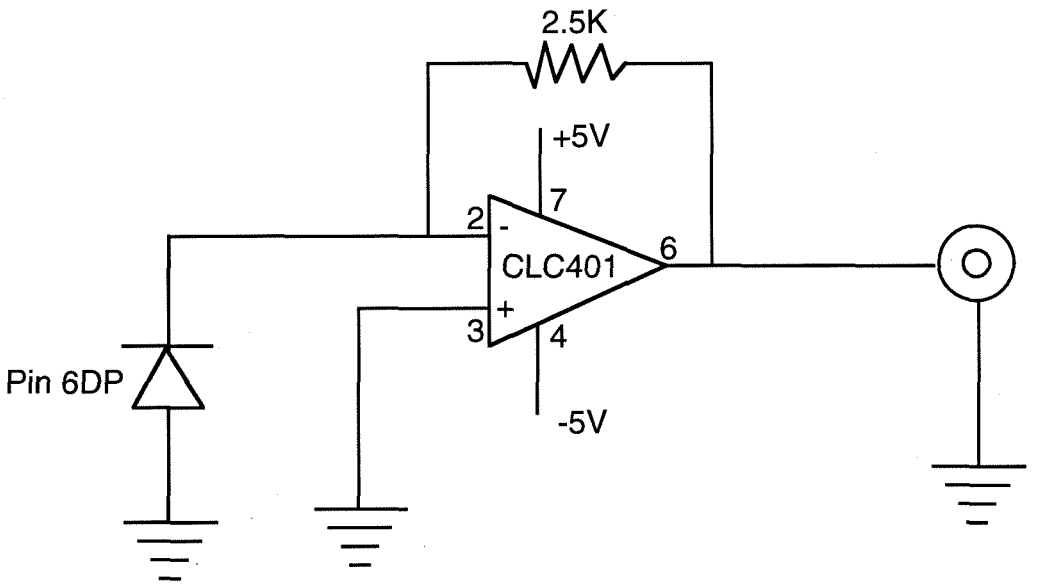

Figure A.3: Amplifier circuit for the photodetector.

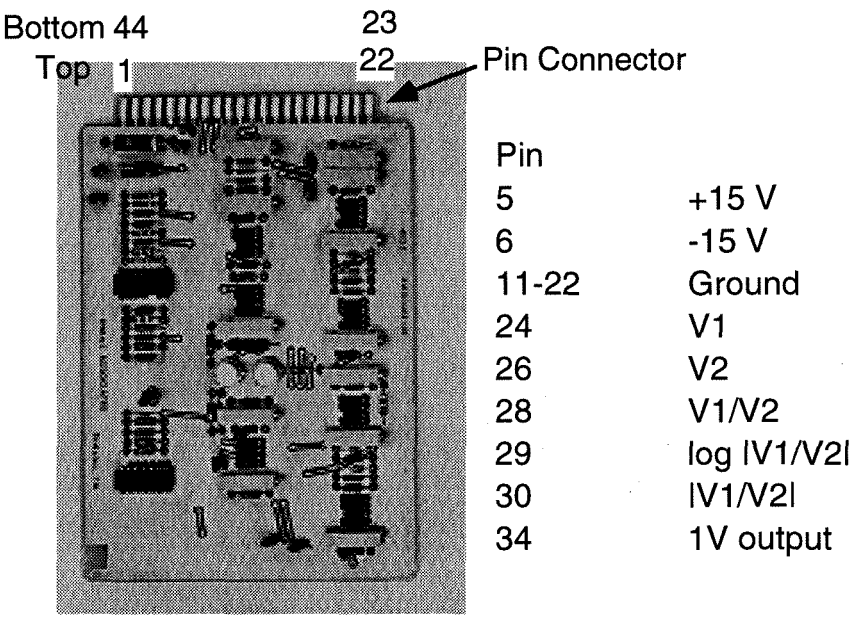

Figure A.4: Ratiometer and its pin connections.

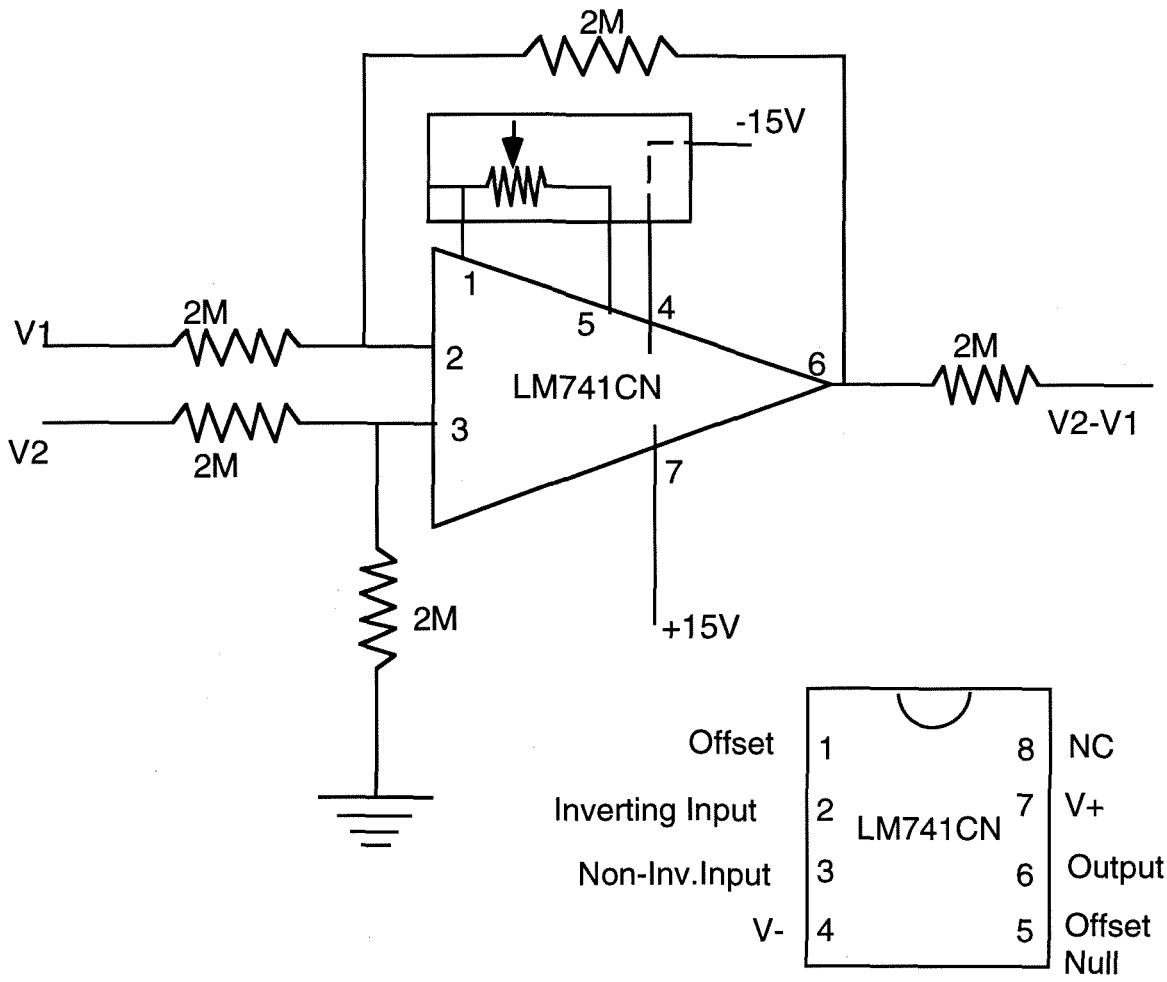

Figure A.5: Circuit diagram for the offset circuit (subtracts two voltages).

image processor (Figure A.6). In the present set-up, the transmitted signal from the LSM photodiode (situated in the LSM base) is routed through the relay switch (*i.e.* connected to either 1A or 2A). When the switch is inactive, this transmitted signal is relayed to the image processor (output 1C or 2C). However, when the relay is energized (12V power supply) the signals input to the ports 1B or 2B are active. The magnitude of the analog signals input through these two ports (1B or 2B) should be below 3V to prevent damage to the video amplifiers in the image processor. The five diodes in series and a resistor (Figure A.6) provide the necessary protection against

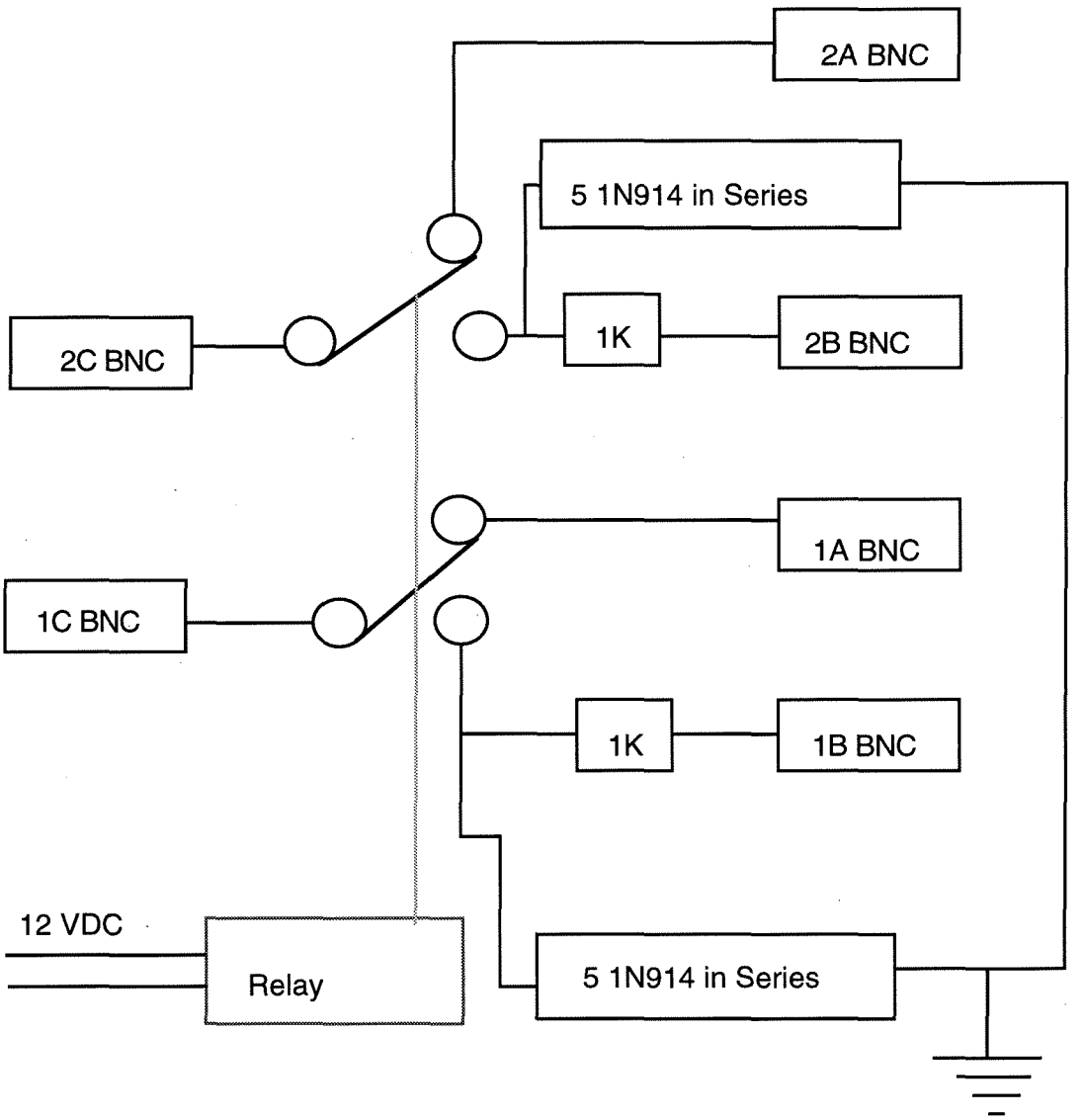

Figure A.6: Design of the relay interface circuit used to toggle between polarization-modulation laser scanning microscopy inputs and conventional laser scanning microscopy.

higher stray voltages.

A.2 Operation of the Microscope

This section briefly outlines some of the important steps and precautions that need to be followed to implement PMLSM. Two critical procedures that have to be emphasized are the insertion of the PEM module, and relaying of the voltage ratios to the microscope unit using the relay interface.

- In LSM10, an internal motor was built-in the microscope to adjust the reflector slider position while switching between conventional transmitted or fluorescence, and laser transmission or fluorescence mode. For that model (*i.e.* LSM10) the PEM module is swapped with the slider only under laser scanning mode and not conventional mode. After the PEM module is inserted conventional mode cannot be used as switching the mode will cause the motor to jam. In LSM320, the motor is no longer present. Care has to be taken to insert the PEM module only to a distance similar to the reflector slider (which is shorter than the PEM module), and it should not be inserted to its complete length. However, conventional mode may be used with LSM320.

- For both LSM10 and LSM320, video amplifiers in the image processing unit of the LSM cannot withstand voltages in excess of 3V. Therefore, prior to input of voltages through the relay-interface, their magnitude **has** to be checked. Extreme caution needs to be exercised as the voltages relayed to the LSM during polarimetric measurements are ratios of two voltages and can therefore

exhibit electrical spikes. For experiments recording transients, it is necessary to know beforehand that voltages will not exceed 3V.

Initial setup requires that the lock-in amplifiers, the low pass filter, the ratiometer and the offset circuit be placed adjacent to the microscope and the appropriate input/output connections be made (Figure A.7). At this stage, points **A** and **B** in Figure A.7 are not connected. Furthermore, the detector is not placed on the field diaphragm. However, the power supply for the detector is switched on so that at the completion of the setup all transient signals have decayed. Switching on the LSM is performed with an initial power-up and firing of the Ar-Ion laser (needs couple of minutes for the laser start-up), followed by turning on the computer. Following steps offer guidelines for further operation:

1. Place a sample of known optical anisotropy (used for polarimetric calibration) on the stage and focus on it in the conventional (or laser transmission mode), and note down the approximate vertical position of the stage.

2. Gently pull the reflector slider out. Carefully insert the PEM module, taking care to push it in a distance similar to the reflector slider. A spring loaded silver-pin (on the front of the microscope stand) needs to be pulled to push the module in. Cover the reflector slider with some lens paper and set it aside safely.

3. Place the detector on the field diaphragm. Switch to laser transmission mode and check if the detector voltage output is below 3V. The polarity (for negative signal) and the amplification of this signal (for low magnitude) can be adjusted

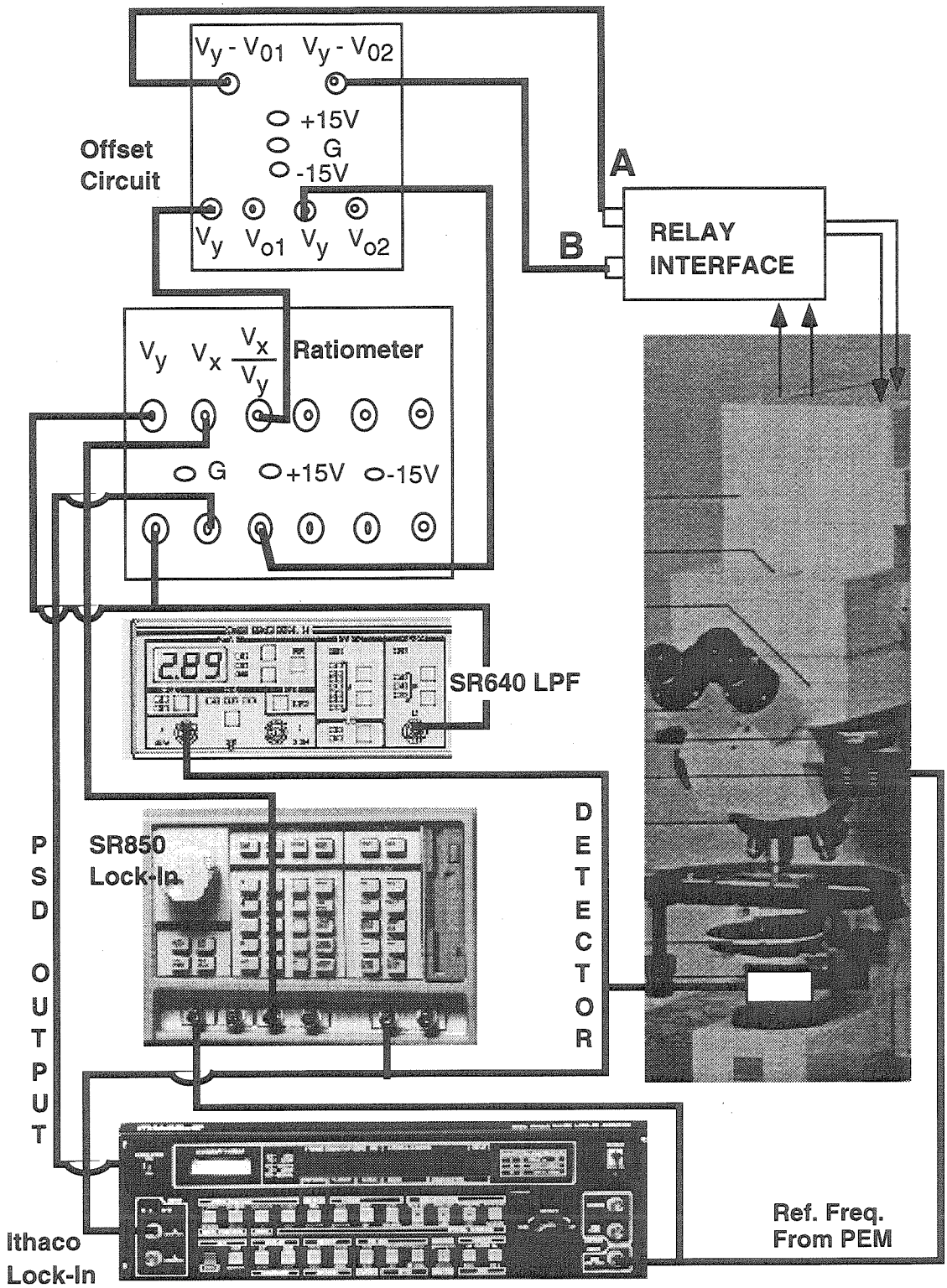

Figure A.7: Set-up of the polarization-modulation scanning microscope and wiring for the ancillary equipment.

by routing through the low pass filter, without switching the filter in (front panel of SR640 low pass filter).

4. Input this detector signal to the relay interface. Upon energizing the relay interface, the image can be observed on the display terminal.

5. Disconnect the detector signal from the relay interface.

6. To image in the birefringence or dichroic mode, switch on the PEM and set its amplitude to the value at which $J_o = 0$ (obtained from calibration). For birefringence imaging, a circular polarizer has to be inserted beneath the sample stage.

7. Switch on the lock-in amplifiers (Stanford Lock-In for first harmonic and Ithaco lock in for second harmonic). Using the spot scan mode of the LSM, adjust the phase on the lock-ins.

8. Place the sample for imaging on the stage and switch to frame scanning mode. For focusing, remove the analyzing optics below the stage and use the unfiltered detector signal to form an image (the PEM amplitude may have to be reduced to about 5).

9. Reinsert the analyzing optics (*i.e.* circular polarizer for birefringence). Switch the low pass filter in, and check the voltage ratios. If they are within the 3V range, an image can be formed using the relay interface. Signal amplification (*i.e.* image contrast) can be achieved by adjusting the sensitivities on the lock-ins and the amplification (dB gain) on the low pass filter. Signal baseline (*i.e.*

image brightness) can be adjusted by using the offset circuits, where offset voltages can be provided by the auxiliary output feature on the SR850 Stanford lock-in amplifier.

Quantitative imaging requires initial calibration for determining the transfer-function that maps voltages to the grey levels used for image display.

$$G = F(C, B)\ V$$

The mapping depends on the brightness and contrast settings on the LSM during imaging, which vary from $[B_1, B_2, B_3, \ldots B_M]$ and $[C_1, C_2, C_3, \ldots C_N]$, respectively. It has to be performed independently for both channels that are to be used for image acquisition. The procedure involves input of voltages from 0V to 3V in small increments ($\sim 0.1V$) following a scheme shown in Figure A.8.

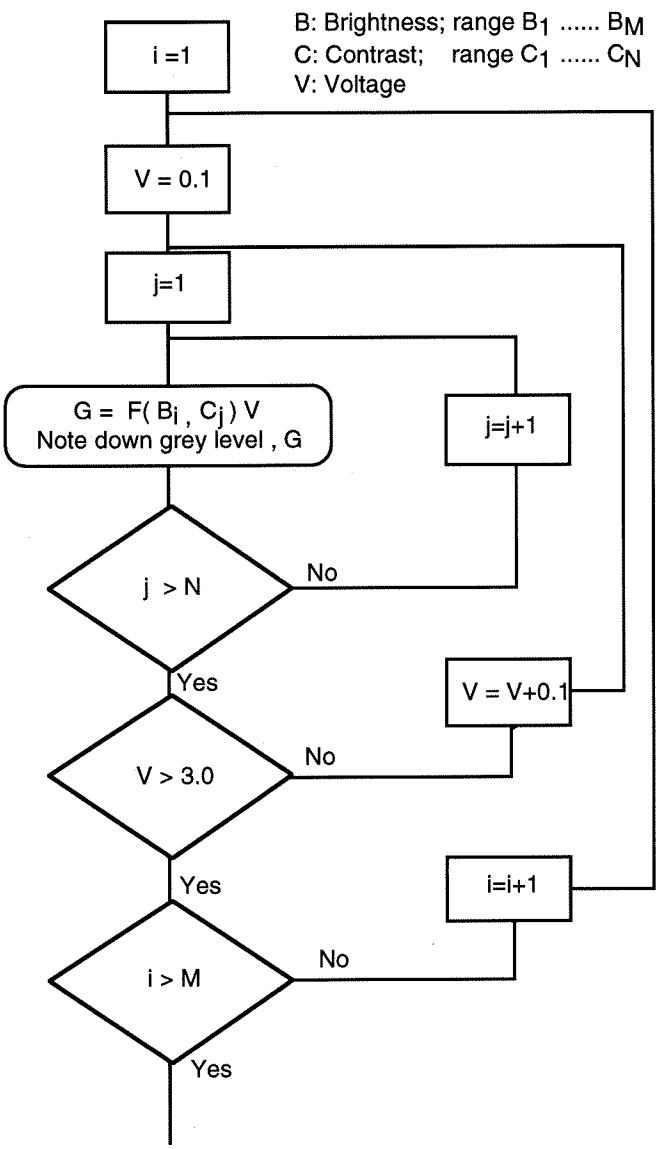

Figure A.8: Calibration scheme to determine transfer function for mapping between grey levels and input voltage.

Bibliography

[1] V. A. Marikhin and L. P. Myasnikova. *Prog. Coll. Sci.*, 92:39, 1993.

[2] L.M. Blinov. *Sov. Phys. Usp.*, 31:623, 1988.

[3] Jr. G.L. Gaines. *Insoluble Monolayers at Liquid-gas Interface.* Interscience Publishers, NY, 1966.

[4] G. G. Roberts. *Langmuir-Blodgett Films.* Plenum Press, NY, 1990.

[5] J. D. Swalen, D.L. Allara, J. D. Andrade, E. A. Chandross, S. Garoff, J. Israelachvili, T. J. McCarthy, R. Murray, R. F. Pease, J. F. Rabolt, K. J. Wynne, and H. Yu. *Langmuir*, 3:932, 1987.

[6] P. Chollet. *Thin Solid Films*, 68:13–19, 1980.

[7] P. Chollet and J. Messier. *Thin Solid Films*, 99:197–204, 1983.

[8] H. G. Braun, H. Fuchs, and W. Schrepp. *Thin Solid Films*, 159:301, 1988.

[9] J. R. Fryer, R. A. Hann, and B. L. Eyres. *Nature*, 313:382, 1985.

[10] N. Uyeda, T. Takenaka, K. Aoyama, M. Matsumoto, and Y. Fujiyoshi. *Nature*, 327:319, 1987.

[11] R. D. Neuman and S. Fereshtehkhou. *J. Colloid and Interface Science*, 125:34, 1988.

[12] Kiyoshi Yase, Stefan Schwiegk, G. Lieser, and G. Wegner. *Thin Solid Films*, 210-211:22, 1992.

[13] F. W. Embs, E. L. Thomas, A. Gittinger, and L. Dulog. *Thin Solid Films*, 237:217, 1994.

[14] T. R. Albrecht, M. M. Dovek, C. A. Lang, P. Grutter, C. F. Quate, S. W. J. Kuan, C. W. Frank, and R. W. F. Pease. *J. Appl. Phys.*, 64:1178, 1988.

[15] J. P. Rabe, M. Sano, D. Batchelder, and A. A. Kalatchev. *J. Microscopy*, 152:573, 1988.

[16] J. H. Coombs, J. B. Pethica, and M. E. Welland. *Thin Solid Films*, 159:293–299, 1988.

[17] E. Meyer, L. Howald, R. M. Overney, H. Heinzelmann, J. Frommer, H.-J. Guntherodt, T. Wagner, H. Schier, and S. Roth. *Nature*, 349:398, 1991.

[18] J. A. N. Zasadzinski, C. A. Helm, M. L. Longo, S. A. C. Gould, and P. K. Hansma. *Biopys. J.*, 59:755, 1991.

[19] L. F. Chi, M. Anders, H. Fuchs, R. R. Johnston, and H. Ringsdorf. *Science*, 259:213, 1993.

[20] J. Y. Josefowicz, N. C. Maliszewski, S. H. J. Idziak, P. A. Heiney, Jr. J. P. McCauley, and A. B. Smith III. *Science*, 260:323, 1993.

[21] J. A. N. Zasadzinski, R. Vishwanathan, L. Madsen, L. Garnaes, and D. K. Scwartz. *Science*, 263:1726, 1994.

[22] A. Keller, E. Pedemonte, and F. M. Willmouth. *Colloid Polym. Sci.*, 238:25, 1970.

[23] M. J. Folkes, A. Keller, and F. P. Scalisi. *Colloid Polym. Sci.*, 251:1, 1973.

[24] G. Hadziioannou, A. Mathis, and A. Skoulious. *Colloid Polym. Sci.*, 257:136, 1979.

[25] G. Hadziioannou, A. Mathis, and A. Skoulious. *Macromolecules*, 15:258, 1982.

[26] F. A. Morrison and H. H. Winter. *Macromolecules*, 22:3533, 1989.

[27] F. A. Morrison, H. H. Winter, W. Gronski, and J. D. Barnes. *Macromolecules*, 23:4200, 1990.

[28] K. Koppi, M. Tirrell, F. S. Bates, K. Almadal, and R. H. Colby. *J. Phys. II*, 2:1941, 1992.

[29] K. Koppi, M. Tirrell, and F. S. Bates. *Phys. Rev. Lett.*, 70:1449, 1993.

[30] K. Amundson, E. Helfand, D. D. Davis, X. Quan, S. S. Patel, and S. D. Smith. *Macromolecules*, 24:6546, 1991.

[31] K. Amundson, E. Helfand, X. Quan, and S. D. Smith. *Macromolecules*, 26:2698, 1993.

[32] K. Amundson and E. Helfand. *Macromolecules*, 26:1324, 1993.

[33] K. Amundson, E. Helfand, X. Quan, S. D. Hudson, and S. D. Smith. *Macromolecules*, 27:6559, 1994.

[34] K. I. Winey, S. S. Patel, R. G. Larson, and H. Watanabe. *Macromolecules*, 26:2542, 1993.

[35] C. R. Safinya, E. B. Sirota, R. F. Bruinsma, C. Jeppesen, R. Plano, and L. J. Wenzel. *Science*, 261:588, 1993.

[36] S. H. J. Idziak, C. R. Safinya, R. S. Hill, K. E. Kraiser, M. Ruths, H. E. Warriner, S. Steinberg, K. S. Liang, and J. N. Israelachvili. *Science*, 264:1915, 1994.

[37] R. Bruinsma and Y. Rabin. *Phys. Rev. A*, 45:994, 1992.

[38] F. S. Bates and G. H. Fredrickson. *Annu. Rev. Phys. Chem.*, 41:525, 1990.

[39] R. G. Larson, K. I. Winey, S. S. Patel, and H. Watanabe. *Rheol. Acta*, 32:245, 1993.

[40] K. I. Winey, S. S. Patel, R. G. Larson, and H. Watanabe. *Macromolecules*, 26:4373, 1993.

[41] T. Provder, M. W. Urban, and H. G. Barth, editors. *Hyphenated Techniques in Polymer Characterization.* ACS Symposium Series, Washington, DC, 1994.

[42] R. A. Azzam and N. M. Bashara. *Ellipsometry and Polarized Light.* North-Holland, Amsterdam, 1987.

[43] J. A. Schellman. In B. Samori and W. Thulstrup, editors, *Polarized Spectroscopy of Ordered Systems.* Kluwer Academic Publishers, Dordrecht, 1987.

[44] G. G. Fuller. *Ann. Rev. Fluid Mech.*, 22:387, 1990.

[45] S. J. Johnson, P. L. Frattini, and G. G. Fuller. *J Coll. Int. Sci.*, 104:440, 1985.

[46] T. Buffeteau, B. Desbat, and J. M. Turlet. *App. Spectros.*, 45:1991, 1991.

[47] D. Blaudez, T. Buffeteau, J. C. Cornut, B. Desbat, N. Escafre, M. Pezolet, and J. M. Turlet. *App. Spectros.*, 47:869, 1993.

[48] C. J. Sheppard and T. Wilson. *Theory and Practice of Optical Scanning Microscopy.* Academic Press, New York, 1985.

[49] Ching-Bo Juang, Laura Finzi, and Carlos J. Bustamante. *Rev. Sci. Instrum.*, 59:2399, 1988.

[50] W. Mickols and M. F. Maestre. *Rev. Sci. Instrum.*, 59:867, 1988.

[51] V. Wilke. volume 396, page 164. Proc. SPIE, 1984.

[52] V. Wilke. *Scanning*, 7:88, 1985.

[53] V. K. Gupta and J. A. Kornfield. *Rev. Sci. Instrum.*, 65:2823, 1994.

[54] J. E. Mark, A. Eisenberg, W. W. Graessley, L. Mandelkern, E. T. Samulski, J. L. Koenig, and G. D. Wignall. *Physical Properties of Polymers.* ACS Professional Reference Book, Washington, DC, 1993.

[55] R. M. Kannan and J. A. Kornfield. *Rheol. Acta*, 31:535, 1992.

[56] R. M. Kannan, J. A. Kornfield, N. Schwenk, and C. Boeffel. *Macromolecules*, 26:2050, 1993.

[57] M. Losche and H. Mohwald. *Rev. Sci. Instrum.*, 55:1968, 1984.

[58] A. Barraud, J. Leloup, P. Maire, and A. Ruaudel-Teixier. *Thin Solid Films*, 133:133, 1985.

[59] Jr. G.L. Gaines and W.J. Ward III. *J. Colloid Interface Sci.*, 60:210, 1977.

[60] E. Orthmann and G. Wegner. *Angew. Chem. Int. Ed. Engl.*, 25:1105, 1986.

[61] G. Duda, A. J. Schouten, T. Arndt, G. Lieser, G. F. Schmidt, C. Bubeck, and G. Wegner. *Thin Solid Films*, 159:221, 1988.

[62] G. Duda and G. Wegner. *Macromol. Chem., Rapid Comm.*, 9:495, 1988.

[63] T. Sauer, T. Arndt, D. N. Batchelder, A. A. Kalachev, and G. Wegner. *Thin Solid Films*, 187:357, 1990.

[64] R. G. M. Crockett, A. J. Campbell, and F. R. Ahmed. *Polymer*, 31:602, 1990.

[65] S. Schwiegk, T. Vahlenkamp, Y. Z. Xu, and G. Wegner. *Macromolecules*, 25:2513, 1992.

[66] M. Suzuki, A. Ferencz, S. Lida, V. Enkelmann, and G. Wegner. *Adv. Mater.*, 5:359, 1993.

[67] B. R. Malcolm. *Thin Solid Films*, 134:201, 1985.

[68] M. R. Buhaenko, J. W. Goodwin, R. M. Richardson, and M. F. Daniel. *Thin Solid Films*, 134:217, 1985.

[69] M. R. Buhaenko, J. W. Goodwin, and R. M. Richardson. *Thin Solid Films*, 159:171, 1988.

[70] J. G. Byatt-Smith and B. R. Malcolm. *J. Chem. Soc. Faraday Trans.*, 90:493, 1994.

[71] B. R. Malcolm. *Langmuir*, 11:204, 1995.

[72] B. R. Malcolm. *Thin Solid Films*, 178:17, 1989.

[73] B. R. Malcolm. *Thin Solid Films*, 178:191, 1989.

[74] M. F. Daniel and J. T. T. Hart. *J Mol. Electron.*, 1:97, 1985.

[75] N. Minari, K. Ikegami, S. Kuroda, K. Saito, M. Saito, and M. Sugi. *J Phys. Soc. Jpn.*, 58:222, 1989.

[76] M. J. Grundy, R. J. Musgrove, R. M. Richardson, and S. J. Roser. *Langmuir*, 6:519, 1990.

[77] G. H. Fredrickson. *J. Rheol.*, 38:1045, 1994.

[78] R. M. Kannan and J. A. Kornfield. *Macromolecules*, 27:1177, 1994.

[79] J. A. Kornfield, R. M. Kannan, and S. D. Smith. volume 71, page 250. Proc. Amer. Chem. Soc., Div. Polym. Mater., 1994.

[80] Y. Zhang, U. Wiesner, and H. W. Spiess. *Macromolecules*, 28:778, 1994.

[81] F. S. Bates, J. H. Rosedale, H. E. Bair, and T. P. Russell. *Macromolecules*, 21:2557, 1989.

[82] J. H. Rosedale and F. S. Bates. *Macromolecules*, 23:2329, 1990.

[83] N. Balsara, B. Hammouda, P. K. Kesani, S. V. Jonnalagadda, and G. C. Straty. *Macromolecules*, 27:2566, 1994.

[84] N. Balsara and B. Hammouda. *Phys. Rev. Lett.*, 72:360, 1994.

[85] S. Okamoto, K. Saijo, and T. Hashimoto. *Macromolecules*, 27:5547, 1994.

[86] T. P. Lodge and G. H. Fredrickson. *Macromolecules*, 25:5643, 1992.

[87] P. Allan, R. G. C. Arridge, F. Ehtaiatkar, and M. J. Folkes. *J. Phys. D: App. Phys.*, 24:1381, 1991.

[88] O. Diat, D. Roux, and F. Nallet. *J. Phys. II, France*, 3:1427, 1993.

[89] K. Almadal, F. S. Bates, and K. Mortensen. *J. Chem. Phys.*, 96:9122, 1992.

[90] F. S. Bates, J. H. Rosedale, and G. H. Fredrickson. *J. Chem. Phys.*, 92:6255, 1992.

[91] K. Kawasaki and A. Onuki. *Phys. Rev. A*, 42:3664, 1990.

[92] M. Rubinstein and S. P. Obukhov. *Macromolecules*, 26:1740, 1993.

[93] F. D. Bloss. *An Introduction to the Methods of Optical Crystallography.* Holt,Rhinehart and Winston, Inc., NY, 1961.

[94] B. S. Pinheiro and K. I. Winey. volume 36, page 174. Polym. Prepr. Amer. Chem. Soc., Div. Poly. Chem., 1995.

[95] S. S. Patel, R. G. Larson, K. I. Winey, and H. Watanabe. Submitted to Macromolecules.

[96] M. E. Cates and S. T. Milner. *Phys. Rev. Lett.*, 62:1856, 1989.